Dissertation

submitted to the

combined faculties of the Natural Sciences and for Mathematics

of the Ruperto-Carola University of Heidelberg, Germany

for the degree of

Doctor of Natural Sciences

Put forward by

Evan C. Border, MSc.

Born in Albuquerque, USA

Oral examination: 29.07.2020

Variability of δ^{234}U

in the

Mediterranean Sea, Amazon Estuary,

and

Atlantic Ocean

Referees

Prof. Dr. Norbert Frank

Prof. Dr. Werner Aeschbach

Variability of δ^{234}U in the Mediterranean Sea, Amazon Estuary, and Atlantic Ocean:

It has long been assumed that the world's oceans are homogeneous in δ^{234}U, even on a sub-‰ scale, however this has not been comprehensively investigated outside of the North Pacific using modern high-precision MC-ICP-MS. In this study, the δ^{234}U of water samples from across the Mediterranean Sea, Amazon Estuary, and North Atlantic is presented to show that the oceanic uranium system is much more variable and dynamic than previously believed and variable on a ‰-scale. Mediterranean water masses are elevated in δ^{234}U compared to the Atlantic by ∼1-2‰, allowing for the estimation of the δ^{234}U of riverine and groundwater inputs to the basin. Analysis within the Amazon Estuary shows that there are significant geographical differences in the non-conservative behavior of U, and that the Amazon has little to no effect on the δ^{234}U of the nearby Atlantic. The upper Atlantic is on average 1‰ lower in δ^{234}U than the deep Atlantic, indicating that oceanic δ^{234}U is not in steady-state but rather decreasing. Results point towards the offset seen in the upper Atlantic possibly being the result of inputs from the Indian Ocean (which has yet to be investigated at such high-precision), indicating that such oceanic δ^{234}U variability may be a widespread phenomena.

Variabilität von δ^{234}U im Mittelmeer, der Amazonasmündung und dem Atlantischen Ozean:

Seit langem wird angenommen, dass die d234U-Isotopie im Ozean überall gleich ist, selbst unterhalb der ‰-Skala. Bisher wurde dies außerhalb des Nordpazifiks kaum mit moderner, hoch-präziser MC-ICP-MS untersucht. In dieser Dissertation wird das δ^{234}U von Wasserproben aus dem gesamten Mittelmeer, der Amazonasmündung und dem Nordatlantik präsentiert, um zu zeigen, dass das ozeanische Uran-System δ^{234}U Änderungen von mehr als 1‰ aufweist und damit viel variabler und dynamischer ist als bisher angenommen. Die Wassermassen des Mittelmeers haben δ^{234}U Werte die ∼1-2‰ höher sind als im Atlantik, was die Schätzung des durchschnittlichen δ^{234}U von Flüssen und Grundwasserquellen die ins Mittelmeerbecken fließen ermöglicht. Analysen innerhalb des Amazonasmündungsgebietes zeigen, dass es bedeutende geographische Unterschiede im nichtkonservativen Verhalten von U gibt und dass der Amazonas wenig bis gar keinen Einfluss auf das δ^{234}U des Atlantiks hat. Das δ^{234}U des oberen Atlantiks ist im Durchschnitt 1‰ niedriger als im tiefen Atlantik, was darauf hindeutet, dass δ^{234}U im Ozean nicht im Gleichgewichtszustand ist, sondern eher abnimmt. Die erhaltenen Ergebnisse legen nahe, dass der Unterschied zwischen oberem und tiefem Atlantik möglicherweise auf eine Übertragung von Wasser mit niedrigem δ^{234}U aus dem Indischen Ozean zurückgeführt werden kann. Dies deutet darauf hin, dass δ^{234}U auch dort viel variabler ist als bisher vermutet.

Contents

1 Introduction **5**

2 Background and Basics **7**
2.1 Ocean circulation 7
2.2 Geochemical properties of uranium 9
2.3 Uranium in the ocean 11
2.4 Uranium isotopes and δ^{234}U 12

3 Materials and methods **19**
3.1 Sample collection 19
3.2 Sample preparation 19
3.3 MC-ICP-MS and the measurement of δ^{234}U 21
3.3.1 High-precision MC-ICP-MS 21
3.3.2 Measurements of δ^{234}U 26

4 Mediterranean Sea δ^{234}U offset **28**
4.1 Introduction 28
4.2 Sample overview 30
4.3 Results 32
4.4 Discussion 36
4.4.1 Mediterranean δ^{234}U offset and water mass fingerprinting . . . 36
4.4.2 Investigating Mediterranean coastal groundwater U-input . . . 40
4.4.3 Modeling overall U-inputs to the Mediterranean Sea 46
4.5 Summary 51

5 U systematics in the the Amazon River Estuary **53**
5.1 Introduction 53
5.2 Sample overview 56
5.3 Results 58
5.4 Discussion 58
5.4.1 Establishing the Amazon River and Atlantic Ocean U mixing end-members 58
5.4.2 Geographical differences in U behavior within the Amazon Estuary 60
5.4.3 High salinity U-behavior and evidence of mangrove influence . 71
5.4.4 Overall influence of the Amazon River on Atlantic δ^{234}U . . . 75
5.5 Summary 76

6 Atlantic δ^{234}U disequilibrium **77**
6.1 Introduction . . . 77
6.2 Sample overview . . . 79
6.3 Results . . . 79
6.4 Discussion . . . 82
6.4.1 δ^{234}U offset between thermocline and deep Atlantic . . . 82
6.4.2 Indian Ocean as source of low-δ^{234}U water . . . 84
6.4.3 Implications for δ^{234}U in the global ocean . . . 86
6.5 Summary . . . 89

7 Conclusions and Outlook **90**

A Data **95**
A.1 Mediterranean Sea . . . 95
A.2 Gulf of Lions: coastal samples . . . 97
A.3 Gulf of Lions: spring samples and groundwater end-members . . . 98
A.4 Atlantic Ocean . . . 99
A.5 Gulf of Cadiz . . . 100
A.6 Amazon . . . 101

B Additional figures **102**

C Lists **103**
C.1 List of Abbreviations . . . 103
C.2 List of Figures . . . 105
C.3 List of Tables . . . 111

D Bibliography **112**

The absence of evidence is not the evidence of absence.

Carl Sagan (*Cosmos*)

1 Introduction

In the mid-1950s a team of Russian scientists discovered something puzzling. Two long-lived uranium isotopes, ^{234}U and ^{238}U, which should be in radioactive equilibrium with one another, showed isotopic ratios in soil and groundwater which varied wildly from expected values (Cherdyntsev, 1955). Shortly thereafter it was revealed that this was far from a mere local occurrence, and that even the mighty oceans are about 15% enriched in ^{234}U (Thurber, 1962). Measurements from the Atlantic, Pacific, and Mediterranean showed that this effect seemed to be uniform among ocean basins (Koide and Goldberg, 1965). Eventually, the development of new measurement techniques allowed for ever-more precise determinations of the magnitude of this offset (typically discussed in terms of δ^{234}U, the magnitude of the offset in ‰ (permil)), first constraining it on a ‰ (Chen et al., 1986; Delanghe et al., 2002) and later sub-‰ (Andersen et al., 2010) scale. At this point, with the isotopic ratio measured as precisely as was currently feasible, the system appeared to be 'solved', at least until the possible future development of an even more precise measurement technique. Even as studies began to reveal past climate-driven changes to oceanic δ^{234}U (Henderson, 2002; Robinson et al., 2004b; Chen et al., 2016), there remained little impetus to further investigate modern seawater, as it was expected that all measurements would return similar values.

Such assumed homogeneity can often mask the true nature of the associated geochemical system and ultimately provide an opportunity for unexpected discoveries. While testing whether the high-precision MC-ICP-MS measurement procedures used at the Institute of Environmental Physics in Heidelberg for the uranium-series dating of carbonates (Arps, 2017) could be adapted to accurately measure the δ^{234}U of seawater, it was found that what initially appeared to simply be spread in the data was actually an unforeseen ‰-scale systematic difference between δ^{234}U in the Atlantic and Mediterranean. As more samples were collected and measured, it became clear that such fine, yet significant, inhomogeneity appears to be an integral feature of the oceanic U system rather than a mere anomaly. Individual water-masses were able to be fingerprinted, inputs from groundwater and rivers were able to be traced and analyzed, and even basin-scale differences between the deep- and upper-ocean (possibly originating from half the world away) were discovered.

Precise knowledge of oceanic δ^{234}U both in the present and past is important beyond mere curiosity. Changes in δ^{234}U over time are used as a paleo-proxy for global weathering and ocean mixing (Robinson et al., 2004b; Chen et al., 2016). The dating of marine carbonates use δ^{234}U as a method of quality-control, to test whether or not a carbonate skeleton was subject to open-system effects (Cheng et al., 2000). Comparisons between δ^{234}U in the upper and deep ocean have been used to constrain

the overall mixing time of the global ocean (Chen et al., 1986; Andersen et al., 2010). As will be demonstrated later, observed systematic differences in δ^{234}U provide a powerful opportunity to investigate uranium inputs and removals from the ocean system, even via processes such as groundwater discharge which are often unable to be measured directly. The finding that δ^{234}U is much more variable than previously believed brings into question many aspects of what is known about oceanic U as well as raising numerous questions (and future research opportunities).

This thesis will begin with an overview of basic background information in Chapter 2, covering ocean circulation, the geochemical properties of uranium, its behavior in the ocean, and finally the δ^{234}U isotopic system. Afterwards in Chapter 3, the methods utilized in this thesis will be discussed, covering sample collection, preparation, and eventual MC-ICP-MS measurement. Chapter 4 will focus on the elevated δ^{234}U found in the Mediterranean Sea, as well as the fingerprinting of water masses, an investigation of coastal groundwater discharge, and the estimation of U-input to the Mediterranean through rivers and submarine groundwater. Afterwards, Chapter 5 will turn the spotlight on the Amazon Estuary, where analysis of U concentration and δ^{234}U showcases large geographical differences in uranium behavior across the estuarine salinity gradient. Finally, Chapter 6 will bring together seawater δ^{234}U measurements from across the North Atlantic to show that the upper-Atlantic has significantly lower δ^{234}U than the deep-Atlantic, indicative of the system not being in steady state and in direct contradiction to conventional theoretical models of oceanic uranium. Afterwards, in Chapter 7, will follow a summary of the main conclusions as well as a discussion of possible paths going forward.

2 Background and Basics

2.1 Ocean circulation

Covering approximately 71% of the Earth's surface, the oceans play an integral role in global processes such as the pole-ward redistribution of energy from the tropics, the regulation and formation of weather, or enabling any number of biogeochemical systems to function. Earth's climate, today a topic of ever increasing relevance, is hugely influenced by the oceans. Currents in the Atlantic transport vast amounts of heat northward and serve to keep much of Europe significantly warmer than similarly north-lying areas of other continents (Palter, 2015), while disruptions to this same system have been attributed with causing the rapid oscillation between ice-ages and warm periods between 25 and 60 thousand years ago (Henry et al., 2016). In the Pacific, oscillations between El Niño and La Niña conditions can dictate weather conditions or trigger to extreme weather events worldwide (McPhaden et al., 2006), with this effect likely to grow stronger due to anthropogenic climate chagne (Cai et al., 2015). In short: The oceans exert an immense influence on the behavior of the Earth system, and it is impossible to understand the world without first looking to the oceans.

From a human perspective the ocean often appears to be largely unchanging. The tides rise and fall, waves crash on the shoreline, but as a whole the system looks relatively static, particularly away from the surface. In reality, it is a complex turbulent system made up of currents and circulations, inflows and outflows, upwelling and downwelling; all happening across many scales and time-scales. In fact even the deep-sea, kilometers below the surface, is slowly circulating over hundreds or even thousands of years. The ocean represents a system which is constantly in motion, and how this system evolves effects the entire planet.

Like any system, to stay in motion requires energy. As is the case with most Earth systems, this ultimately originates from the sun. The ocean is excellent at absorbing sunlight, particularly at high incidence angles, however sunlight is not evenly distributed across the Earth's surface. The Earth exists as a sphere, which receives an essentially uniform beam of radiation from the sun, resulting in much higher radiation flux density in the tropics than in the polar regions. This energy imbalance leads the water in the tropics to warm and expand relative to lower-energy regions, which causes sea levels in the tropics to be $\sim 1\ m$ (relative to the geoid) higher than they are near the poles, creating a global meridional pressure gradient (Marshall and Plumb, 2007). The effects of this gradient are most pronounced near the surface of the ocean (where solar energy is collected) leading to a general flow of upper ocean waters towards the colder polar regions. As surface water flows pole-

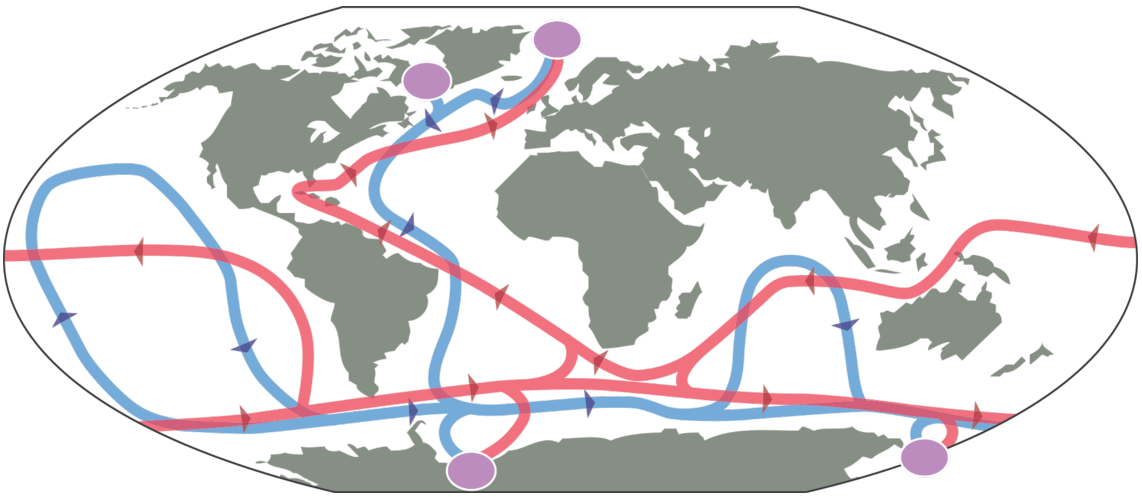

Figure 2.1: The overturning circulation of the oceans. Red arrows indicate surface currents. Blue arrows are deep-sea currents. The purple circles are areas of deep-water production. Figure from Hansen et al. (2004).

ward, it cools and gradually loses buoyancy until it eventually sinks and becomes cold, dense deep-ocean water. Due to mass conservation, this constant pole-ward flow of surface water must be balanced by an equal return flow, which takes the form of deep-sea currents, slowly making their way back equator-ward to complete the cycle.

This system is known as the thermohaline circulation (THC) and is fundamental to understanding the oceans. The entire system is constantly, slowly, circulating; driven by imbalances in solar radiation. This is of course a simplified view, which is ultimately complicated by a number of factors such as the presence of continents and their unequal distribution, the coriolis effect, surface wind-shear and of course turbulence. Together these effects combine to produce the overarching currents of the THC, the major features of which are shown in Figure 2.1. Circulation is split between two largely independent regimes corresponding to the upper (red) and deep (blue) ocean. These systems are connected by areas of so-called 'deep-water production', where surface water is cooled by heat loss to the atmosphere, loses buoyancy, and sinks (Marshall and Plumb, 2007). Deep water production is highly localized, with the majority taking place at four locations: the Labrador and Greenland Seas in the north, and the Weddell and Ross Seas to the south (Rahmstorf, 2006). The reverse process where deep-water returns to the surface is much more diffuse and thus harder to observe, yet is believed to happen primarily in the Southern Ocean (Marshall and Speer, 2012). Much of the circulation in the THC, particularly in the deep-sea, takes place on very long time-scales, with the full mixing time on the order of 1000 years (Broecker and Peng, 1982; England, 1995; Khatiwala et al., 2012).

The ocean system contains much more than mere water. Broecker and Peng (1982) describe the ocean as a "chemical plant" containing a vast array of additional

constituents, each being biogeochemically cycled according to their inputs, removal mechanisms, reactivity, or importance in biological functions. In oceanography dissolved ions and their isotopic systems are often of particular interest, as changes to a particular isotopic ratio can often be attributed to fractionation brought about by certain biogeochemical processes. Therefore, these isotopic systems can be studied as proxies so as to shed light on the process in question, which may not itself be otherwise directly observable. Such proxy techniques allow for the study of past ocean dynamics (so-called *paleoceanography*), as changes in isotopic systems are often stored in archives such as the skeletons of cold-water corals. These skeletons can last hundreds of thousands of years and are able to be absolutely dated to high precision using uranium-series analysis (Cheng et al., 2000), allowing for reconstructions of the isotopic makeup of ambient water as it was during the lifetime of the coral.

2.2 Geochemical properties of uranium

Uranium (U) is a metal with an atomic number of 92, placing it within the actinides. It is found naturally nearly everywhere on Earth, with the crust containing between 3-4μg g^{-1} (Choppin et al., 2013) and the oceans having a typical concentration of 3.3μg l^{-1} (Chen et al., 1986). There exist three natural isotopes, ^{238}U, ^{235}, and ^{234}U, with ^{238}U being by far the most abundant, making up over 99% of all uranium on Earth. The isotopic makeup will be discussed more in depth in Section 2.4. With an average atomic mass of 238.02891 Da (Meija et al., 2016), uranium is the heaviest naturally occurring element on Earth.

In a geochemical context, uranium has two relevant oxidation states, U(IV) and U(VI), though additional states such as U(III) and U(V) are found very rarely. These differ strongly in their solubility. U(VI) is typically found as the highly soluble uranyl ion (UO_2^{2+}) while U(IV) forms the highly reactive and only weakly soluble U^{+4} ion (Markich and Brown, 2018) which is readily absorbed by colloids or particulates (Zänker and Hennig, 2014). U(VI) uranyl can form a number of soluble complexes with inorganic and organic ligands, whose frequency is dependent upon pH (Markich and Brown, 2018). In seawater, dissolved uranium is almost entirely in the form of uranyl-carbonate complexes such as $UO_2[CO_3]_2^{2-}$ or $UO_2[CO_3]_3^{4-}$ (Krishnaswami and Kirk Cochran, 2008). The determining factor of uranium solubility is the presence of dissolved oxygen. In oxic solutions U is typically in the U(VI) state, while in anoxic or highly suboxic conditions, in which U(VI) cannot form its typical uranyl complexes, U(VI) is generally reduced to U(IV) and loses solubility (Krishnaswami and Kirk Cochran, 2008). Therefore, in most biogeochemical applications uranium can be considered highly soluble.

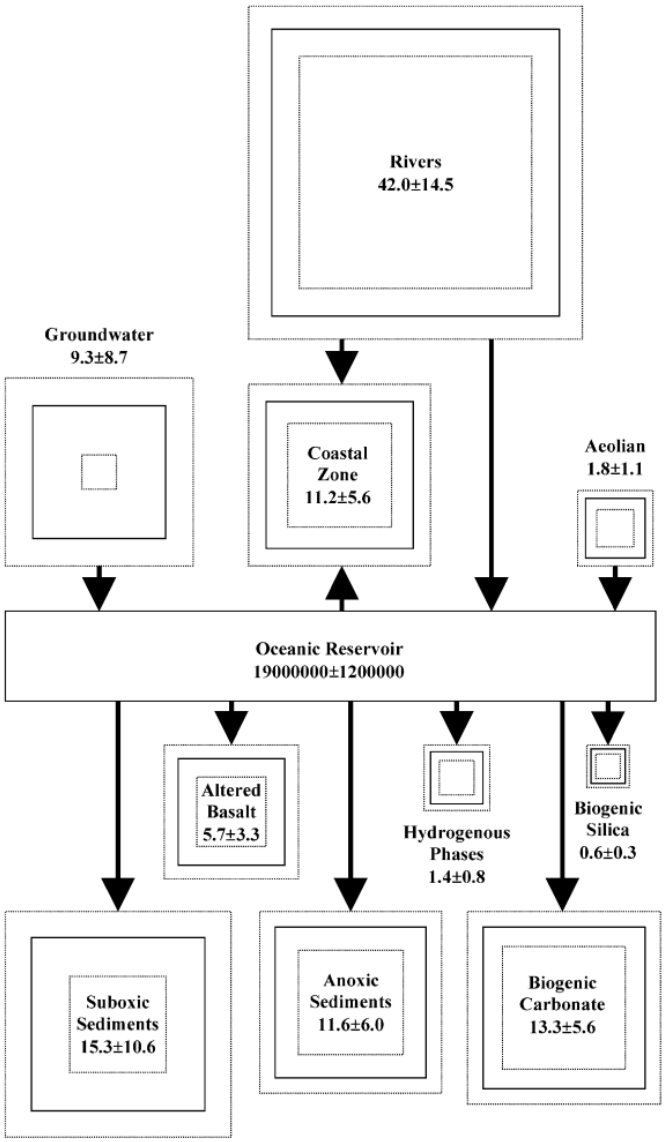

Figure 2.2: A schematic of the ocean U budget for the Holocene from Dunk et al. (2002). Inputs and removals are shown in terms of Mmol/yr, while the ocean inventory is in Mmol.

2.3 Uranium in the ocean

In the ocean, uranium is a conservative (i.e. 'salt-like') tracer with a long residence time on the order of 300-600 thousand years (Dunk et al., 2002; Henderson, 2002). As such, U concentrations are closely related to salinity through the relationship U (μg l^{-1})=(0.0919 $\pm$ 0.0005)$\times$salinity (Chen et al., 1986), which works out to $\sim$3.2 μg l^{-1} at a salinity of 35 PSU. This concentration is assumed to be in steady state due to both its relative homogeneity within the worlds oceans as well as the record of U/Ca ratios in well-preserved coral skeletons being virtually constant going back until the last glacial maximum (Bender, 1973; Broecker, 1971; Swart and Hubbard, 1982).

Figure 2.2 shows the oceanic U budget for the Holocene according to Dunk et al. (2002). Rivers dominate oceanic U-input, accounting for roughly four times the input of the next largest source, groundwater. Global water discharge from rivers is estimated to be 0.95-1.11 Sv (Milliman, 2001; Dai and Trenberth, 2002) (Sverdrup, 1 Sv = 10^6 m^3/s = 3.15$\times 10^4$ km^3/yr) carrying an average U concentration of 0.3μg l^{-1} (Palmer and Edmond, 1993). Concentrations are highly variable from river to river, ranging from from 0.01 to 100 μg l^{-1} (Osmond and Ivanovich, 1992). This large spread in U concentrations means that the magnitude of a river's water discharge does not always correlate with its importance as a uranium source. As an example, the Huang He (Yellow River, U concentration = 7.5 μg l^{-1}) has a larger absolute flux of U than the Amazon River (U conc. = 0.04 μg l^{-1}), despite freshwater discharge from the Amazon being a factor of 100 higher (Chabaux et al., 2003). The study of riverine U is complicated by their estuaries which sometimes act non-conservatively, particularly in the low-salinity regime where a reduction in U concentration is often observed (Sarin et al., 1990; Sarin and Church, 1994; Swarzenski et al., 2004; Moore and Shaw, 2008). As such, the effect of any given river on oceanic U cannot be determined without first analyzing across the salinity gradient of any associated estuary, as these have the potential to significantly alter the river's effective U contribution.

The second largest source of oceanic U is groundwater, specifically submarine groundwater discharge (SGD). SGD is a broad category, encompassing any and all flows of water on continental margins from the seabed to the coastal ocean, regardless of fluid composition or driving force (Burnett et al., 2003). This therefore includes everything from hydraulic-head driven inflow through a surficial aquifer to wave- or hydrothermally-driven seawater-porewater exchange (Moore, 2010). The overall discharge of water via SGD is still poorly constrained as it is nearly impossible to observe directly. Recent studies have pointed towards the overall magnitude of SGD being much higher than previously thought, with estimates ranging from roughly $\sim$1 Sv (i.e. equal to riverine discharge) (Moore et al., 2008) to 3-4 times this amount (Kwon et al., 2014). Among all varieties of SGD, it is likely that surficial aquifers are the most important with regards to oceanic U. These typically have concentrations on the scale of 1μg l^{-1}, while deeper aquifers and sediment porewaters are more likely to be anoxic and thus usually contain lower concentrations, on the order of only a few ng l^{-1}(Andrews and Kay, 1982; Osmond and Cowart, 2000). Though rare,

much higher concentrations on the scale of hundreds of μg l^{-1} have been measured in groundwater in Finland (Suksi et al., 2006).

The removal of U takes place primarily in the reducing environments found within anoxic or suboxic sediments, although coastal zones such as estuaries, salt marshes, or mangrove swamps as well as uptake during the formation of biogenic carbonate also play an important role (Dunk et al., 2002). The removal process is therefore of a more wide-spread nature than the more localized inputs and occurs primarily in the deep-sea. Oceanic U cycling can therefore be approximated by a two-box model (Figure 2.5, with one box representing the upper ocean and the second the deep ocean and the only connections between the two being the creation of deep water and gradual upwelling (Chen et al., 1986). This will be discussed later in Section 2.4, in conjunction with the isotopic makeup of oceanic U.

2.4 Uranium isotopes and δ^{234}U

Uranium has three naturally occurring isotopes with highly variable abundances: ^{238}U (99.2745%), ^{235}U (0.720%), and ^{234}U (0.005%) (Choppin et al., 2013). There exists two additional long-lived synthetic isotopes, ^{233}U and ^{236}U, which are released as a result of human nuclear activity and may occasionally be found in trace amounts. All U isotopes are radioactive, with the half-lives of natural isotopes ranging from hundreds of thousands to billions of years. The two longest-lived isotopes, ^{238}U and ^{235}U with half-lives of 4.4683×10^9 yrs and 7.0381×10^8 yrs respectively (Jaffey et al., 1971), are primordial. Each of these forms the basis of a decay-chain which begins with the isotope in question and ends, by way of numerous intermediate daughter nuclides, with a stable isotope of lead. The ^{238}U chain is shown in Figure 2.3 and is known as the *uranium series*, while the ^{235}U chain is known as the *actinium series*. This thesis focuses exclusively on the two isotopes (^{238}U and ^{234}U) which are part of the uranium series.

In a closed system, the long half-life of of the primordial nuclide ^{238}U when compared to its daughter nuclides leads to an interesting long-term effect, known as *secular equilibrium*. The decay of each nuclide i can be described as

$$N_i(t) = N_i(0)e^{-\lambda_i t} \tag{2.1}$$

where N_i represents the quantity of radionuclide i and $\lambda_i t$ its decay constant (related to the half-life through $\lambda = ln(2)/t_{1/2}$). On time scales t significantly smaller than the half-life of the primordial isotope (in this case ^{238}U, but for clarity referred to as $i = 0$, with each successive daughter nuclide referred to as $i = 1, 2, 3...$)

$$\lambda_0 t \ll 1 \tag{2.2}$$

leading to

$$e^{-\lambda_0 t} \approx 1 \tag{2.3}$$

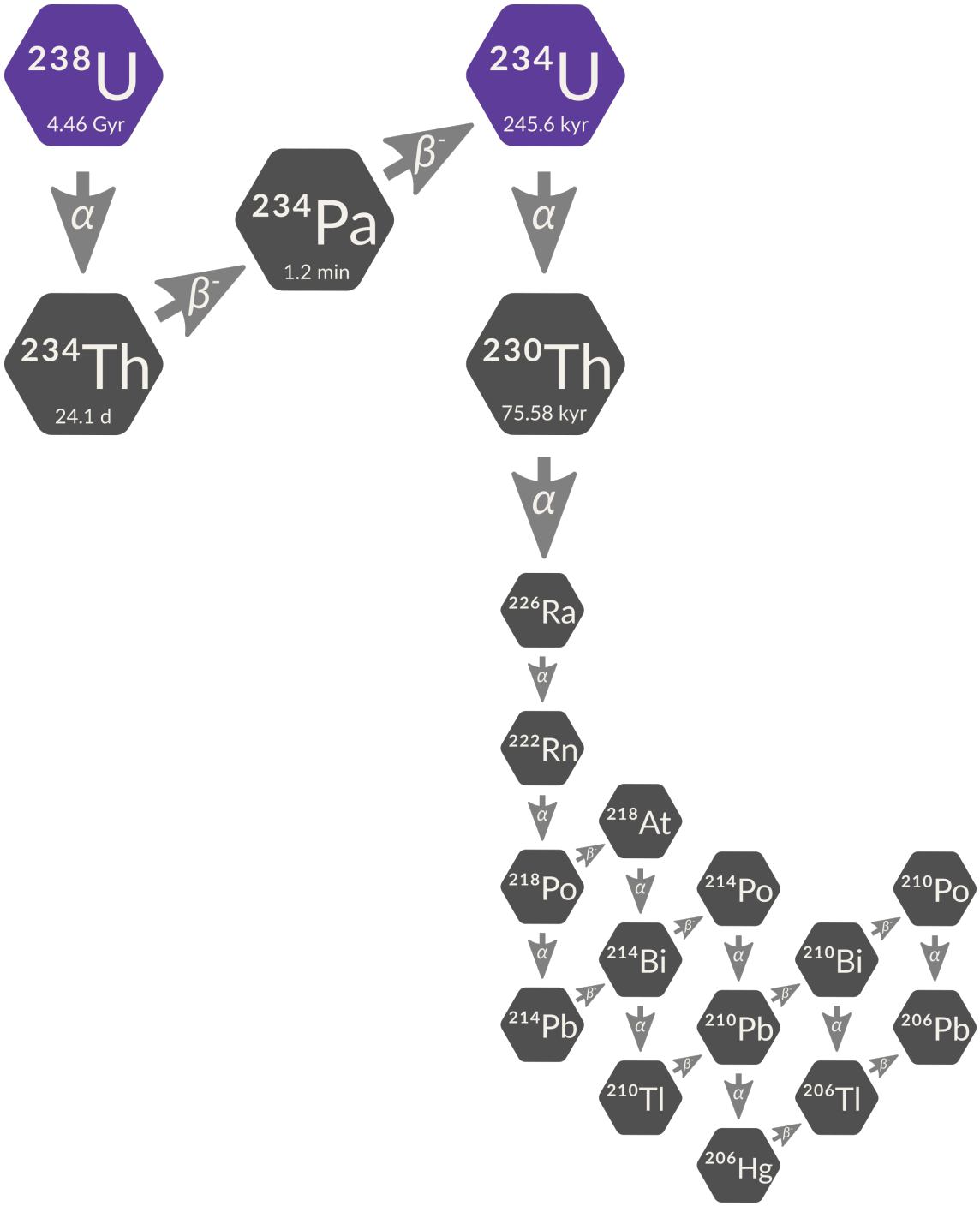

Figure 2.3: The ^{238}U decay chain, also known as the *uranium series*. The two uranium isotopes are highlighted in purple. The chain begins with primordial ^{238}U and ends with stable ^{206}Pb.

Therefore, on such time scales, N_0 can be assumed to be constant with respect to time. The change in abundance of the first daughter isotope (in the case of the uranium series ^{234}Th, or $i = 1$) with respect to time can be given as

$$\frac{dN_1}{dt} = \lambda_0 N_0 - \lambda_1 N_1 \tag{2.4}$$

representing the in-growth from decay of the parent nuclide 0 and removal due to its own decay. This will reach equilibrium when $dN_1/dt = 0$ (on the time scale of several half-lives of daughter isotope 1) resulting in

$$N_1 = \frac{\lambda_0}{\lambda_1} N_0 \tag{2.5}$$

which implies that, since N_0 is constant, N_1 is constant as well as λ_i is time-independent. On time scales much longer than the half-lives of all daughter nuclides yet much shorter than the half-life of the primordial isotope, this may be generalized for the entire decay chain as

$$N_{i+1} = \frac{\lambda_i}{\lambda_{i+1}} N_i \tag{2.6}$$

excluding the final stable member, which accumulates over time. Introducing the concept of *activity*, defined as

$$A_i = \lambda_i N_i \tag{2.7}$$

or 'the number of decays of nuclide i per unit time', Equation 2.6 can be reformulated as

$$\frac{\lambda_{i+1} N_{i+1}}{\lambda_i N_i} = \frac{A_{i+1}}{A_i} = 1 \tag{2.8}$$

This shows that under ideal conditions, the decay chain reaches an equilibrium where the number of decays per unit time is equal among all members, often referred to as *unity*.

This is, of course, how things develop as part of an ideal, closed system and does not always match reality. Particularly in aqueous systems such as rivers (e.g. Moore, 1967; Mangini and Dominik, 1979; Chabaux et al., 2003), groundwater (e.g. Cherdyntsev, 1955; Rosholt et al., 1964; Dooley et al., 1966; Osmond and Cowart, 2000), and even the ocean (e.g. Thurber, 1962; Ku et al., 1977; Chen et al., 1986; Delanghe et al., 2002; Andersen et al., 2010), ^{238}U and ^{234}U are often found to be in radioactive disequilibrium with one another. The fractionation process responsible for this is known as the *α-recoil effect* and is a direct consequence of both uranium's high solubility as well as its radioactivity. This effect takes place primarily at the boundary between water (groundwater or porewater) and fractured rock matrix (such as bedrock or sediment) and leads to the water becoming enriched in ^{234}U,

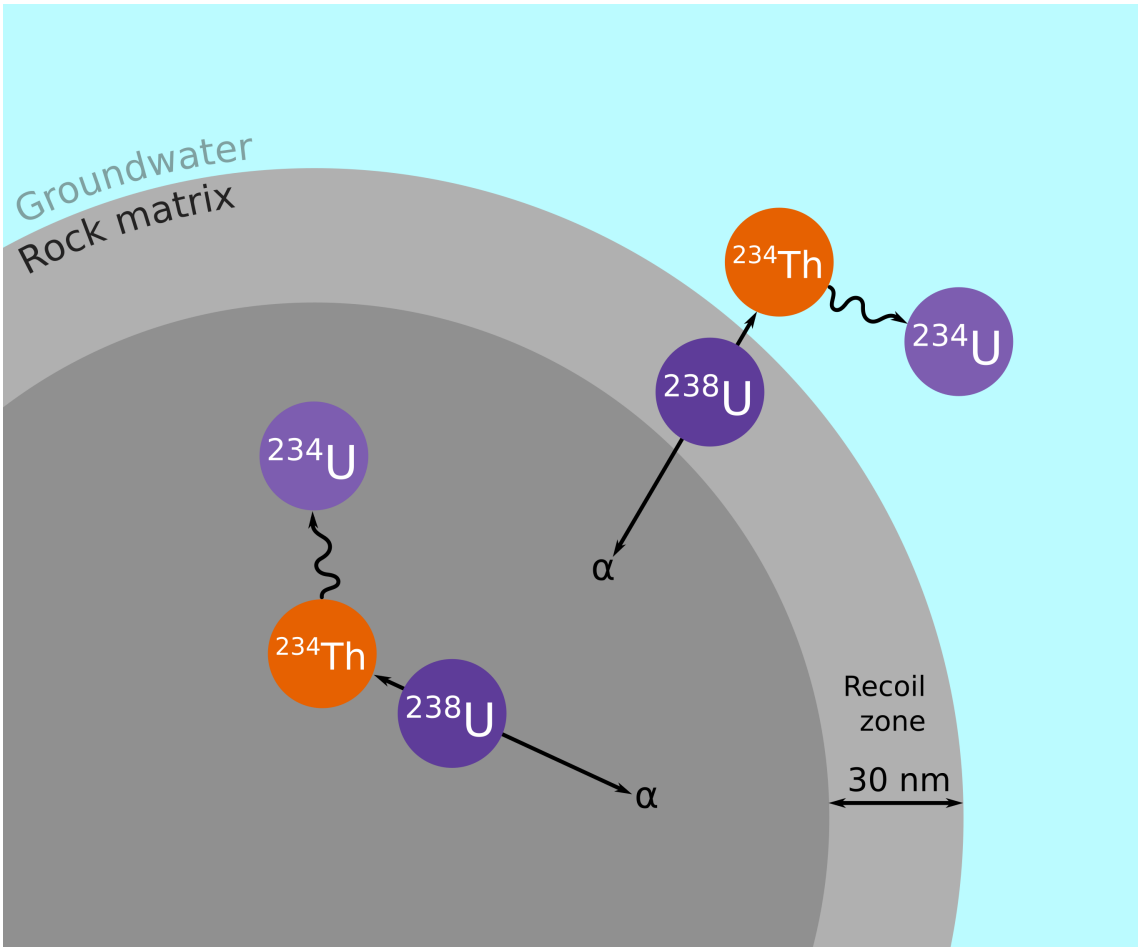

Figure 2.4: A conceptual view of the α-recoil effect, which is responsible for the elevated (i.e. above unity) ^{234}U content of groundwater, rivers and the ocean.

while nearby fractured or porous rock matrix becomes depleted (Dooley et al., 1966; DePaolo et al., 2006), indicating a transfer of ^{234}U between the solid and liquid phases.

When ^{238}U decays into ^{234}Th it emits an *alpha*-particle and, following Newton's third law, itself experiences an opposing recoil. Supposing that this decay takes place near the surface of fractured bedrock surrounded by groundwater, this recoil effect may cause the ^{234}Th to be ejected into the surrounding groundwater, where it quickly decays into ^{234}Pa and then ^{234}U (Figure 2.4). Since uranium is highly soluble, this ejected ^{234}U is quickly dissolved and remains in the liquid phase. This only affects decaying ^{238}U which is located closer to the solid-liquid interface than the recoil distance, which is typically on the order of 30 nm (DePaolo et al., 2006) (labeled as 'recoil zone' in Figure 2.4). ^{238}U decays well within the rock matrix do not cause an ejection of the nuclide and therefore do not directly contribute to the fractionation. In all, this has the effect of preferentially transferring ^{234}U from the rock matrix to ambient water leading to an enrichment of ^{234}U in the water and a depletion in the bedrock. As such α-recoil induced ejection can only take place directly near the surface of the host rock, the strength of the overall fractionation effect is dependent on the surface-area to volume ratio (and therefore the particle size) of the rock matrix. Physical weathering is therefore thought to increase this overall effect, both through exposing fresh surfaces for ^{234}U to eject from as well as releasing ^{234}U from damaged crystallographic sites as the result of internal α-recoil (Henderson, 2002). A recent study has proposed that even under dry conditions (such as the lowering of the water table), α-recoil causes excess ^{234}U to accumulate on the outer surface of the bedrock, which may then be 'collected' when groundwater returns (Wendt et al., 2019).

With the advent of high-precision measurement techniques such as MC-ICP-MS (discussed later in Section 3.3.1) the activity ratio between ^{234}U and ^{238}U is typically discussed in delta notation (δ^{234}U), which is defined as the deviation from secular equilibrium (i.e. unity) in permil

$$\delta^{234}U(‰) = \left(\frac{A_{^{234}U}}{A_{^{238}U}} - 1\right) \times 1000 \tag{2.9}$$

A positive δ^{234}U value therefore indicates an enrichment in ^{234}U, while a negative value represents a depletion.

The isotopic makeup of oceanic U is notable for having an apparently uniform ~15% enrichment in ^{234}U (Thurber, 1962; Ku et al., 1977; Chen et al., 1986; Delanghe et al., 2002). This offset was first analyzed using high-precision MC-ICP-MS (see Section 3.3.1) by Andersen et al. (2010), who found an average value of δ^{234}U $= 146.8 \pm 0.1$‰ in samples primarily from the North Pacific. This study was the first to show significant basin-scale regional variations in oceanic δ^{234}U, as it found well-mixed samples from the Arctic Ocean were to be on average 0.5‰ higher than samples from other ocean basins. This enrichment is largely the result of the elevated δ^{234}U in riverine input, without which the system would slowly return to

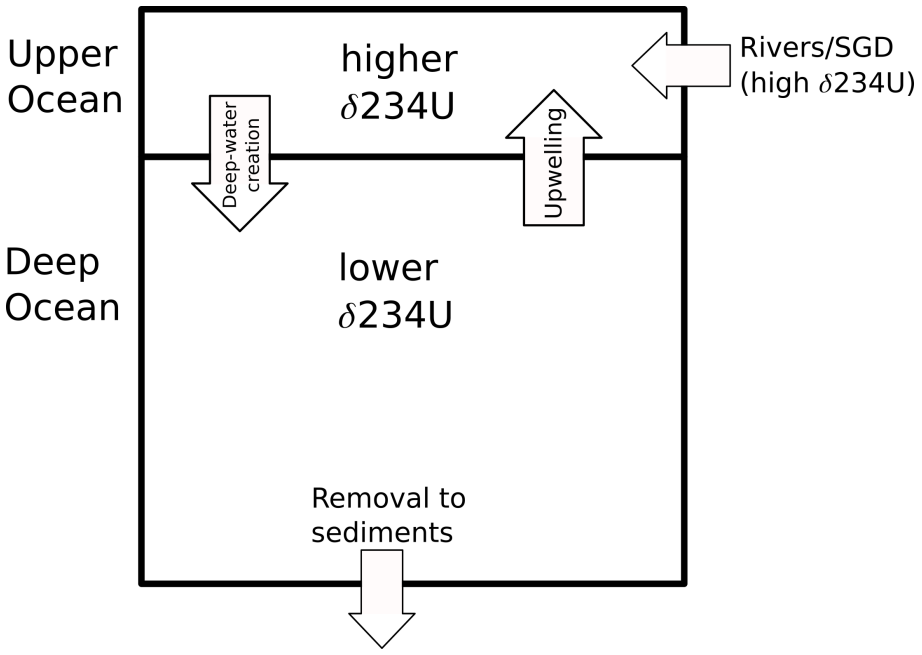

Figure 2.5: A model of the oceanic U system according to Chen et al. (1986). Inputs are primarily to the upper ocean, while removal occurs primarily in the deep-sea.

secular equilibrium. Following this, Henderson (2002) has estimated the average riverine δ^{234}U value to be 223‰.

It has been theorized that the upper ocean should display a slightly higher δ^{234}U than the deep ocean, as most inputs (with high δ^{234}U) take place at the surface, while removal occurs primarily in the deep ocean (Chen et al., 1986). These two regimes (i.e. the upper and deep ocean) are, following the behavior of the THC, only connected by deep-water production in one direction and upwelling in the other (Figure 2.5). If it is assumed that oceanic U is in steady state, the magnitude of such an offset could be used to constrain the overall mixing time of the ocean (Chen et al., 1986). This theoretical offset has as of yet never been observed and thus assumed to be smaller than the external reproducibility of the average oceanic δ^{234}U value (Chen et al., 1986; Andersen et al., 2010). Most recently, this approach has been used by Andersen et al. (2010) to constrain the vertical mixing time of the ocean to less than 1000 years, according to an apparent 2σ external reproducibility of ±0.4‰ across seawater samples.

Though allegedly quite uniform in the present, studies of sediments (Henderson, 2002), cold-water corals (Chen et al., 2016; Krengel, 2020) and tropical corals (Esat and Yokoyama, 2006; Chutcharavan et al., 2018) indicate that δ^{234}U has varied significantly over at least the past 800 kyr. As an example, values were on the order of 2-5‰ lower during the last glacial maximum (LGM) before rapidly increasing approximately 15 kyr ago to values slightly higher than those found today (Chen et al., 2016; Krengel, 2020). There is evidence that the ocean has experienced

periods of heterogeneity with respect to δ^{234}U. During the transition from LGM to the Holocene there existed a significant (3-4‰) offset between the low-latitude Atlantic and low-latitude Pacific over the course of ∼3 kyr (Chen et al., 2016), while corals from the Alboran Sea indicate a potential ∼1-2‰ offset between the Mediterranean and Atlantic over the course of the Holocene (Krengel, 2020).

3 Materials and methods

3.1 Sample collection

The majority of samples were collected as part of various scientific cruises (2014 MoccoMebo (RV *Maria S. Merian*, Hebbeln et al. (2015)), 2016 Mingulay-Rockall (RV *L'Atalante*, (Elliot, 2016)), 2017 UFO (RV *Meteor*, Frank (2017)), 2018 M147 Amazon-GEOTRACES (RV *Meteor*, (Koschinsky et al., 2018))) using Niskin bottles mounted on shipboard CTD ('conductivity, temperature, and depth') devices. These are lowered by cable from the research vessel, with onboard sensors sending back real-time information about the ambient water properties. At any point, upon reaching a desired depth or water-mass, an individual Niskin bottle may be closed, collecting water from the current depth. A typical setup (Figure 3.1, showing the Seabird "SBE 9 plus" from the RV *Meteor*) includes 24 attached Niskin bottles (allowing for the sampling of up to 24 depths with one cast), as well as sensors for measuring temperature, salinity, and pressure. Additional sensors are often added to the CTD to meet the specific needs of each expedition or simply to provide additional data. Examples of these include those for measuring oxygen content, irradiance, flourescence, turbidity, or distance to the sea floor. Other samples, such as those from along the Mediterranean Coast, were collected using small hand-held water pumps, while water properties were recorded using a separate small CTD unit.

Samples were filtered upon collection through Pall 0.45 μm *AcroPak* filters before being acidified using 6 M HCl to a pH of 2, so as to prevent the dissolved U from falling out of solution. Samples were stored either in 10 l 'cubitainers' or 125-250 ml Polypropylene bottles. These were closed with parafilm and sealed within garbage bags to reduce the risk of contamination or spillage during transport. All samples were stored at IUP Heidelberg.

A more in-depth description of the relevant samples, as well as their collection, is provided at the beginning of each chapter.

3.2 Sample preparation

In order to measure the isotopic ratio of seawater uranium using high-precision MC-ICP-MS (described in Section 3.3), it is necessary to extract the dissolved U from the seawater matrix. This avoids clogging or damaging the mass-spectrometer due to the high salt content of seawater, while also reducing matrix effects and enabling a larger signal through greatly concentrating the sample U. The extraction process follows a modified version of the column chromatography used at IUP Heidelberg for extracting U and Th from carbonate archives (e.g. cold-water corals, speleothems)

Figure 3.1: The CTD setup aboard the RV *Meteor*, as used to collect samples from the Amazon region. The 24 Niskin bottles are open, ready for deployment. The CTD unit and sensors can be seen at the bottom. In this particular instance the CTD unit is a Seabird "SBE 9 plus".

for the purposes of U-series dating (see Douville et al. (2010) for the original process). The primary reasons for alterations are the much lower U concentrations in seawater compared to carbonates, necessitating larger sample sizes, as well as the high salinity content of the samples, which each typically contain about 1.5 g of salt. Additionally Th was not of concern, as seawater generally contains very little.

A typical sample consisted of 40 ml of seawater, with the majority being weighed and spiked with a mixed ^{233}U and ^{236}U solution to allow later calculation of the original uranium concentration. Samples were then evaporated and subsequently dissolved in 15 ml of 7 N HNO_3. Uranium extraction was achieved using a column packed with 500 ml of UTEVA chromatographic resin Horwitz et al. (1992). Samples were loaded onto preconditioned columns in a stepwise fashion, as the dissolved samples (∼15 ml) were much larger volume than the remaining free space in the columns (∼2 ml). Each column was then rinsed with 3 ml of 7 N HNO_3, followed by 3x 1 ml of 7 N HNO_3, with the resulting solution discarded. Finally, the sample beakers were placed under the columns and the uranium was eluted once with 1 ml 3 N HCl followed by five elution steps using 1 ml 1 N HCl. The resulting eluate was collected and the samples were evaporated. All columns were subsequently filled with water and stored for use a second time. Once the samples were completely dry, they were redissolved in 1 ml 1 N HNO_3. The columns were re-opened and the water allowed to drain out. After the columns were reconditioned, the samples again loaded onto the same columns, after which the same rinsing and elution steps described earlier were carried out a second time. The samples were again subsequently evaporated. Once completely dry, the samples were dissolved in 1.2 ml 1% HNO_3+0.05% HF. Once dissolved, the samples were transferred to 1.5 ml centrifuge tubes, centrifuged for 15 minutes, and decanted into measurement tubes. This seeks to remove any particulates left over in the solution which may harm the mass-spectrometer. As a final step, 1% HNO_3+0.05% HF was added to the samples to ensure they each contain at least 1.2 ml of solution and therefore enough for the measurement.

3.3 MC-ICP-MS and the measurement of δ^{234}U

This section will be split into two parts. The first will give some background and information about both high-precision mass spectrometry in general as well as the specific measurement device utilized, while the second will deal with the specifics of the δ^{234}U measurements performed for this thesis.

3.3.1 High-precision MC-ICP-MS

Multi-collector inductively coupled mass spectrometry (MC-ICP-MS) represents one of the most powerful tools in analytical chemistry today. Similar to other mass spectrometric systems, its core functionality is to separate the constituents of a sample based on their mass-to-charge ratio and through this provide a measurement of the relative abundance of chosen chemical compounds, elements, or isotopes.

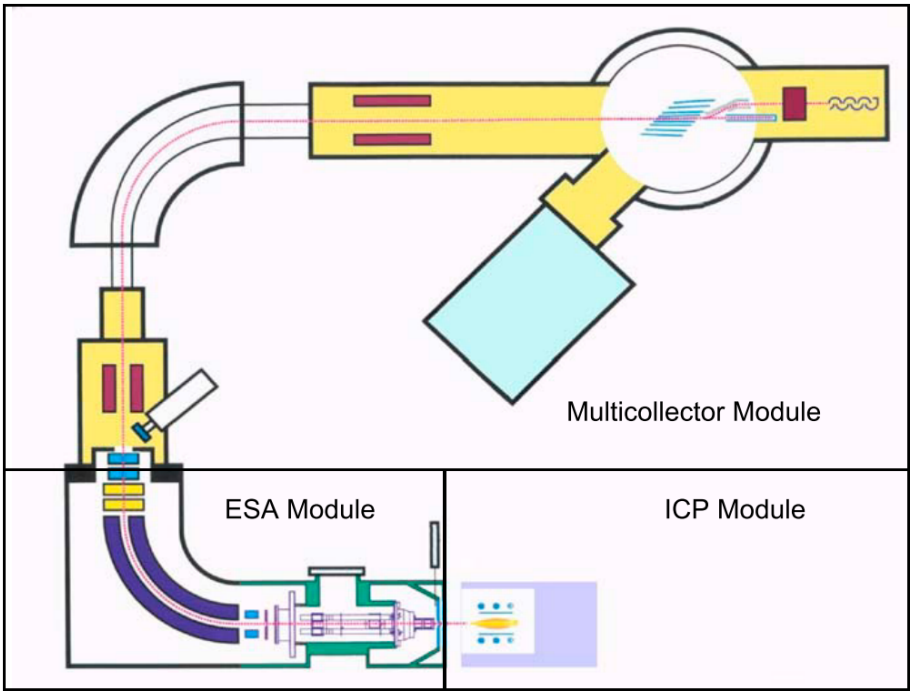

Figure 3.2: The basic layout of the Thermo Fisher Neptune *plus* used for measuring δ^{234}U in this thesis. Samples were introduced to the ICP module using a Cetac Aridus II rather than the built-in nebulizer. Figure adapted from ThermoFisher (2009).

There exist a wide variety of mass spectrometers, each of which may have different methods of sample ionization, mass separation, or ion detection. Accordingly, each system may provide specific advantages or drawbacks based on the intended scientific use-case. MC-ICP-MS has a very high mass resolution and specializes in resolving isotopic systems. Therefore, for the field of isotope geochemistry, which depends upon the ability to precisely measure differences or changes in isotopic makeup of environmental systems, MC-ICP-MS has become an invaluable tool.

The MC-ICP-MS device used for the measurements in this thesis was the Thermo Fisher Neptune *Plus* at the Institute for Environmental Phyics (IUP) in Heidelberg, Germany. As shown in Figure 3.2, the device is split into three main parts: an ICP (inductively couple plasma) Module, which ionizes the sample and introduces it to the machine; an ESA (electrostatic analyzer) Module, which filters the ions based on kinetic energy; and a Multicollector Module, which both separates the filtered ions based on mass over charge as well as measuring the resulting abundances.

The main component of the ICP module is the argon plasma torch, a cross-section of which is shown in Figure 3.3. To generate the plasma, the load coil couples a 27.12 Mhz RF field into the flowing argon gas, producing sustained temperatures exceeding 8000 °C (ThermoFisher, 2009). The sample is introduced to this plasma in the form of a fine aerosol, where it is instantaneously and efficiently ionized. Samples are initially in liquid form and as such must first be converted to aerosol

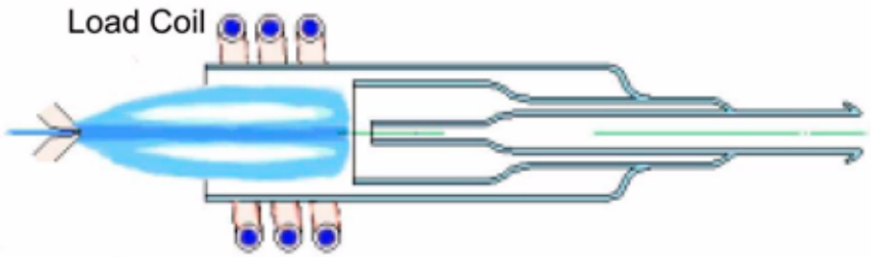

Figure 3.3: A cross section of the plasma torch. Figure adapted from ThermoFisher (2009).

before being introduced to the plasma torch. This necessity to convert from liquid to aerosol is one of the inherent weaknesses of MC-ICP-MS, as only very little of the sample is successfully nebulized and makes its way to the torch. This is typically on the order of 3-5% (Thomas, 2013). Though the Thermo Fisher Neptune *Plus* comes equipped with its own nebulizer and spray chamber, this has been replaced at IUP Heidelberg with a CETAC Aridus II nebulizer fed by an Elemental Scientific SC-2 DX autosampler.

Once particles are ionized in the ICP Module, they are introduced to the ESA Module through a series of two cones (the 'sample' and 'skimmer' cones) which allow only the center of the beam to pass through. These serve as both the interface between the external atmospheric pressures and internal vacuum as well as filtering excess electrons, photons, and gas molecules from the ion beam (ThermoFisher, 2009). After these come a series of lenses and quadrupoles, known collectively as the 'transfer lens system', where the beam is shaped and focused. At this stage the vacuum is also increased, with pressures reaching on the order of 10^{-7} mbar, which further accelerates the beam.

At this point, the ion beam enters the primary portion of the ESA Module: the ESA itself. This is (along with the magnetic sector) one of the two primary focusing mechanisms, which ultimately enable the production of a mass spectrum. Though as a whole an MC-ICP-MS device such as the Neptune is highly sophisticated, the principles guiding how it filters and separates ions are ultimately grounded in relatively basic physical concepts. In the case of the ESA, this is the movement of charged particles within a uniform electric field. The ESA is made up of two 90° curved plates with opposite applied DC voltage. The inner plate is negatively charged, while the outer plate is positively charged, resulting in an electric field of intensity E between the plates. As ions with charge q travel through the ESA, the centrifugal force balances the electric force, resulting in:

$$qE = \frac{mv^2}{r} \tag{3.1}$$

where m is the mass of the particle, v is the velocity, and r is the radius of the ESA.

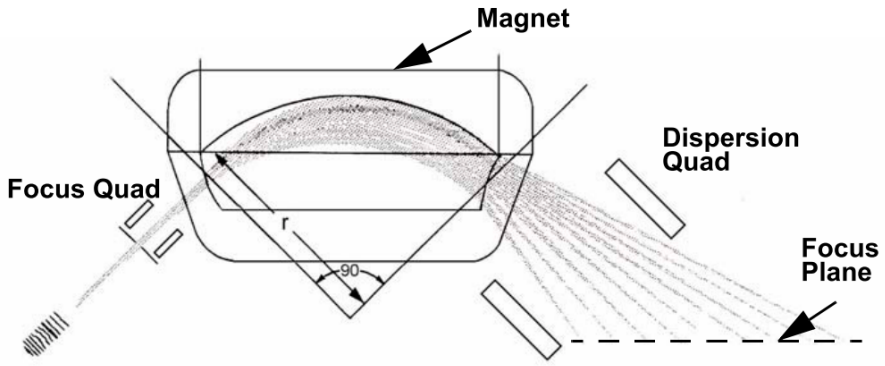

Figure 3.4: Mass dispersion in the magnetic sector of the Neptune. Figure adapted from ThermoFisher (2009).

Substituting in the entrance kinetic energy (E_k) of the ion and solving for r gives:

$$r = \frac{2E_k}{qE} \tag{3.2}$$

or the trajectory of the ion within the ESA. This trajectory is independent of the mass and depends only upon the charge and kinetic energy of the ion. Because of the dependence on charge, negative ions (which are also produced in the plasma (Thomas, 2013)) are eliminated. At the end of the ESA, there is a a slit which limits the possible trajectories which may pass through. This effectively acts as an energy filter, allowing only ions with a narrow range of kinetic energies to pass into the magnetic sector (ThermoFisher, 2009).

After leaving the ESA the ion beam enters the Multicollector module. This is split into two primary components: the magnetic sector (MS) and the detectors. The MS generates a large magnetic field which can be adjusted to a maximum of 1.2 T (ThermoFisher, 2009). This is the primary method by which ions are separated by mass and therefore allows for the measurement of a mass-spectrum (Figure 3.4). As the magnetic field (B) is oriented perpendicular to the velocity of the ion beam, the magnetic force is given by:

$$F_m = qvB \tag{3.3}$$

Similarly to the ESA, ions follow a path with radius r, which leads to the centrifugal force balancing the magnetic force

$$qvB = \frac{mv^2}{r} \tag{3.4}$$

which then simplifies to

$$r = \frac{mv}{qB} \tag{3.5}$$

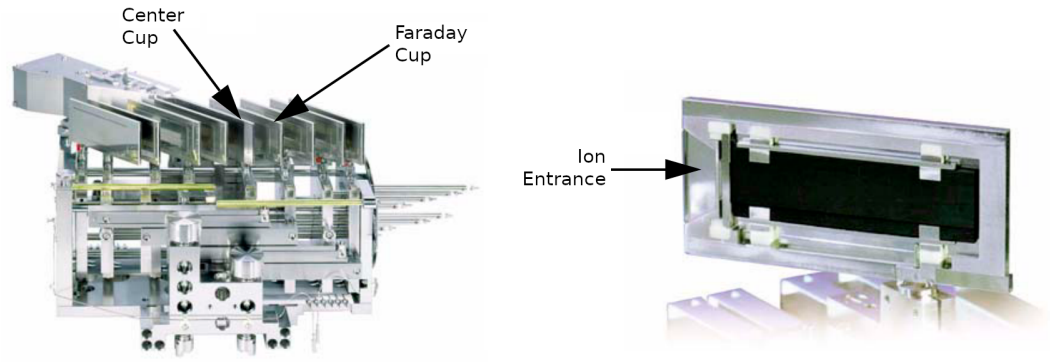

Figure 3.5: (left) The multicollector array, with eight mobile Faraday cups and one fixed 'center' cup. (right) A zoomed in view of a Faraday cup with the cover removed. Figures adapted from ThermoFisher (2009).

which shows that the trajectory is dependent on the momentum (mv) of the ion, and that the MS is fundamentally a momentum analyzer (Hoffmann and Stroobant, 2007). Taking the kinetic energy of the ions to be

$$E_k = \frac{mv_2}{2} \tag{3.6}$$

combining with Equation 3.4 and solving for r gives

$$r = \frac{\sqrt{2mE_k}}{qB} \tag{3.7}$$

The trajectory is therefore dispersive with respect to both kinetic energy, mass, and charge. In general, the E_k of each ion will be relatively similar due to the filtering within the ESA, although this is not perfect and there remains a certain degree of spread in the kinetic energies of the ions when they enter the MS. This is compensated for by the setup of the ion optics within the Neptune, where the energy dispersion within the ESA and MS are exactly the same magnitude, but opposite sign (ThermoFisher, 2009). The E_k dependence of the ion trajectory within the MS therefore cancels out the E_k dispersion in the ESA, leaving only a dependence on mass and charge. This is known as *double focusing* and allows for ions of the same mass to charge ratio but differing kinetic energies to ultimately arrive at the same location on the detectors (Hoffmann and Stroobant, 2007).

The second major piece of the Multicollector Module is the multicollector itself. This is an array of eight movable detector platforms and one fixed center channel, enabling the measurement of up to nine masses simultaneously. Each of the movable detectors platforms is equipped with a Faraday cup, while the fixed channel can be switched between directing the ion beam to either a Faraday cup or an ion counter (secondary electrom multiplier). For this study only Faraday cups were used. These are small cups made from solid carbon which the ion beam strikes, causing the ions to accept electrons from the Faraday cup walls and neutralize. The multicollector

Cup	L1	C	H1	H2	H3
Resistor (Ω)	10^{12}	10^{13}	10^{11}	10^{11}	10^{10}
Mass (Da)	233	234	235	236	238
Typical Intensity ($10^{11}\Omega$ equiv.)	6 mV	14 mV	1.6 V	0.8 V	220 V

Table 3.1: The typical setup for δ^{234}U measurement with the Thermo Fisher Neptune *Plus*. Typical intensities are in terms of what the current would be when measuring with the standard $10^{11}\Omega$ resistor.

array as well as an individual Faraday cup can be see in Figure 3.5. Each Faraday cup is attached to ground through a resistor which causes a current proportional to the number of ions hitting the detector walls (Hoffmann and Stroobant, 2007). Each Faraday cup is connected to an current amplification system with adjustable resistors ranging from $10^{10}\Omega$ to $10^{13}\Omega$ allowing for the measurement of a high range of signal intensities. This is particularly useful when analyzing systems similar to δ^{234}U where ^{238}U is approximately 10^5 times more abundant than ^{234}U. The highly abundant isotope can be measured using the low ohmic resistor (e.g. $10^{10}\Omega$) while the low abundance isotope can be simultaneously measured using one of the high ohmic resistors.

3.3.2 Measurements of δ^{234}U

Analysis of all samples took place on the Thermo Fisher Neptune *Plus* at IUP Heidelberg. All masses analyzed (233, 234, 235, 236, 238) were measured on Faraday cups. A typical setup is shown in Table 3.1 along with utilized resistors and typical signal intensities (in $10^{11}\Omega$ equivalent) for a standard seawater sample with $\sim 3\mu g\, l^{-1}$ concentration. Intensities decreased considerably for lower concentration samples, however all remained within their associated dynamic ranges (i.e. signal-to-noise ratios of less than 2‰) as laid out by Dornick (2016).

Before each measurement sequence, a h-as solution was measured to correct for both Hydride ions (H^+) as well as tailing and abundance sensitivity. Samples were then measured using standard-sample bracketing (i.e. alternating standard and sample measurement) to best allow for correction of instrument drift. The standard utilized is a Harwell Uraninite (Hu-1) solution diluted to intensities similar to that of the water samples. Hu-1 is in secular equilibrium (i.e. $\delta^{234}U = 0$) and previous measurements ($n = 1009$) over a three year period from January 2017 to February 2020 at IUP Heidelberg have shown a reproducibility of $(^{234}U/^{238}U) = 1.00004 \pm 0.00014$ (1σ standard deviation). Before each standard or sample measurement the machine was rinsed and a chemical blank was measured. Integration times for each measurement were 2.099 s, with 200 scans for samples and 100 scans for standards. Using this approach, it is possible to analyze approximately three samples per hour. Samples were measured primarily during the day as opposed to overnight so that standard drift could be regularly checked and, if found to be too high (indicative of instability in the MC-ICP-MS device), the measurement could be terminated.

Typical δ^{234}U errors are on the order of 0.2-0.4‰ for samples with a seawater-like concentration.

After measurement, data was corrected for influence from Hydride ions and tailing through use of the automatic MATLAB script from Arps (2017). As the measured Hu-1 standard is in secular equilibrium, correction for measurement drift was accomplished through dividing the raw activity ratio by the average of the two bracketing standards. This has the effect of raising or lowering the measured δ^{234}U in accordance with the 'offset' of the standards. When measuring δ^{234}U to sub-‰ precision, instrument stability is of the utmost importance as high instability may cause permil-scale swings in measured δ^{234}U. To this end the bracketing standards are an invaluable tool, as sudden large changes in standard δ^{234}U are indicative of measurement instability. As the differences in oceanic δ^{234}U are very small (on the ‰- to sub-‰-scale) a strict limit on standard drift of 0.8‰ was implemented. All samples whose bracketing standards differed by more than this amount were rejected. Overall 1σ standard reproducibility across all measurements lies at 0.6‰.

4 Mediterranean Sea δ^{234}U offset

4.1 Introduction

The Mediterranean Sea is a large mostly-enclosed sea covering $2.5{\times}10^6$ km^2 which lies between the European and African continents. It has an average depth of approximately 1500 m, although depths can reach up to 5267 m. Within the sea there are two primary basins, the Western and Eastern Basins, which are connected by the relatively shallow Strait of Sicily with a maximum depth of ∼300 m. The Mediterranean is only connected to the Atlantic (and by extension the world's ocean system) at its very western edge, through the narrow Strait of Gibraltar (SoG). This strait is a mere 14 km wide and a maximum of 900 m deep (although mean depths are only about 365 m). At its northeastern extent, the Mediterranean is connected to the Black Sea through the Bosporus-Marmara-Dardanelles system which at its narrowest point (in the Bosporus section) is only around 700 m wide and 65 m deep. Since 1869 there is an additional artificial connection between the Mediterranean and Red Sea in the form of the Suez Canal, however this represents only a negligible amount of water exchange (Shaltout and Omstedt, 2015).

Although often considered part of the ocean system, being connected to the Atlantic only through the SoG greatly limits Ocean-Mediterranean water exchange. The upper layers at the SoG constitute an inflow from the Atlantic with a volumetric flow of 0.86 ± 0.10 Sv, which overlays an outflow of 0.80 ± 0.08 Sv (Jordà et al., 2017). This input and outflow do not balance one another, with evaporation instead playing a key role. Because of this, the Mediterranean Sea is known as a 'concentration basin', where salinities rise above those found in the outer ocean. If the SoG were to be closed, evaporation would no longer be balanced by excess input and sea levels in the Mediterranean would decrease by 0.5-1.0 m yr^{-1} (Millot and Taupier-Letage, 2006). The residence time for water within the Mediterranean is highly variable, ranging from days to centuries, though the average is ∼ 50-100 yrs (Millot and Taupier-Letage, 2006). Deep waters have the highest residence times, with those for deep waters in the Eastern Basin being significantly longer than their western counterparts (Tanhua et al., 2013).

Other inputs to the Mediterranean are, in comparison to flow through the SoG, very small. As such, for sake of clarity it makes more sense to discuss these volumetric flows in terms of km^3 yr^{-3} rather than Sv (1 Sv = 31536 km^3 yr^{-3}). According to Jordà et al. (2017) water input to the Mediterranean from the Black Sea is 275 km^3 yr^{-3}, while total river input is slightly higher at 375 km^3 yr^{-3}. Submarine groundwater discharge (SGD) contributes an additional 1400 km^3 yr^{-3}, with only 70 km^3 yr^{-3} of this freshwater and the remainder consisting of recirculated saline

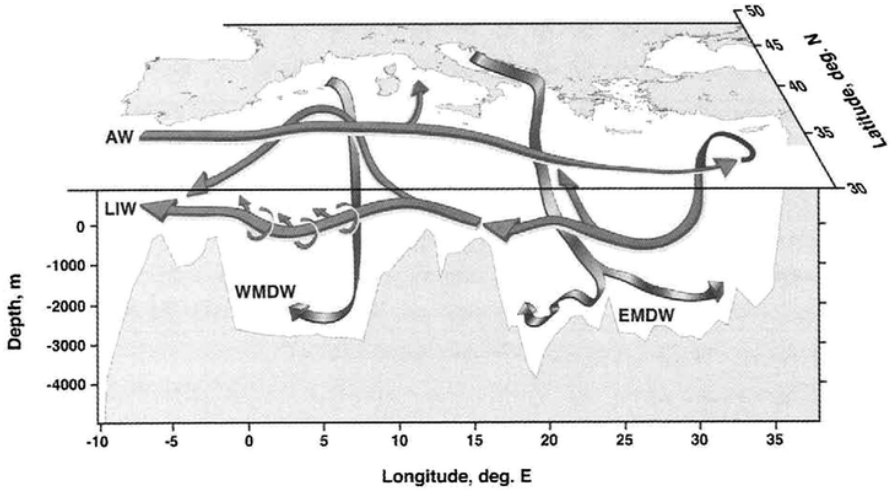

Figure 4.1: The major features of the Mediterranean Overturning Circulation. Atlantic Water (AW, also known as Modified Atlantic Water (MAW)) flows in through the SoG and across the basin where (due to evaporation) loses buoyancy and becomes Levantine Intermeditate Water (LIW). Western Mediterranean Deep Water (WMDW) and Eastern Mediterranean Deep Water (EMDW) are formed in the GoL and Adriatic Sea respectively. Figure adapted from Tsimplis et al. (2006).

water from the Mediterranean Sea itself (Rodellas et al., 2015). When combined, these inputs are less than 8% as large as the inflow through the SoG, which highlights how, despite being semi-enclosed, exchange with the Atlantic remains the dominant influence on the makeup and composition of Mediterranean water.

Figure 4.1 shows a simplified schematic of Mediterranean circulation. There are generally three distinct layers within the water column. Atlantic Water (AW) flows into the Mediterranean where it remains at the surface as it gradually is altered through evaporation and mixing as it transits eastward across the sea. Because of these changes, this water mass is generally referred to as Modified Atlantic Water (MAW) once it is within the Mediterranean to distinguish from the unaltered AW which enters through the SoG. Some of this MAW becomes dense enough due to evaporation-inflicted buoyancy loss that it sinks in the Eastern Mediterranean and becomes Levantine Intermediate Water (LIW), which returns westward. The deepest water masses (and the largest by volume, collectively referred to as Mediterranean Deep Water (MDW)) are Western Mediterranean Deep Water (WMDW) and Eastern Mediterranean Deep Water (EMDW), formed sporadically in winter due to deep convection in the Gulf of Lions (GoL) and Adriatic Sea respectively (Robinson et al., 2001b). These three levels of water mass converge in the Alboran Sea, where WMDW can be found at much shallower depths than otherwise and, particularly in the south along the Moroccan coast, lies directly below MAW (Fabres et al., 2002). Mediterranean Outflow Water (MOW), the Atlantic water mass created by the outflowing of water from the Mediterranean through the SoG consists of a dynamic mix

of LIW and WMDW which forms in the Alboran Sea (Kinder and Parilla, 1987).

Previous analyses of δ^{234}U in Mediterranean seawater have been carried out using α-spectroscopy (Koide and Goldberg, 1965) and TIMS (Delanghe et al., 2002). Each of these found the Mediterranean to be indistinguishable from the ocean at-large in terms of δ^{234}U, indicating that any systematic variation in δ^{234}U which is present is likely to be on a scale (i.e. ‰ to sub-‰) that is only resolvable through MC-ICP-MS. Riverine inputs to the Mediterranean, which should represent an important source of new uranium to the system, are largely unstudied. Of the ten largest rivers by discharge (Rhône, Po, Drin-Bojana, Nile, Neretva, Ebro, Tiber, Adige, Seyhan, and Ceyhan), only the Rhône, the largest, has been investigated for both U concentration (^{238}U = 1.1 μg l^{-1}, (Ollivier et al., 2011)) and δ^{234}U (δ^{234}U = 120‰, (Zebracki et al., 2017)). The Rhône is rather atypical for world rivers, having a δ^{234}U value which, while being above secular equilibrium, is lower than that of the ocean (δ^{234}U = 146.8) (Chabaux et al., 2003). The Black Sea has a strongly depth-dependent δ^{234}U signature which ranges from 179.2‰ (1.21 μg l^{-1}) in Black Sea Deep Water (BDW) to 196.3‰ (1.88 μg l^{-1}) in Black Sea Surface Water (BSW) (see additional Figures B.1 and B.2 in the appendix). Input from the Black Sea to the Mediterranean consists nearly exclusively of BSW (Zodiatis, 1994) and therefore constitutes a very significant source of high-δ^{234}U.

This chapter will present the first high-precision MC-ICP-MS δ^{234}U study of seawater from the Mediterranean, nearby Atlantic, and suspected SGD sites in the GoL. The aim is to investigate how the δ^{234}U of the Mediterranean Sea compares with that of the Atlantic on a sub-permil scale and to explore the causes of any differentiation. Particular emphasis will be placed upon SGD inputs as a possible source of high-δ^{234}U, with samples taken from SGD outflows in the GoL as well as from nearby seawater being analyzed. Finally, a simple box model of the Mediterranean U-budget will be used to determine the average δ^{234}U and U concentration of SGD and riverine input. The SGD inputs analyzed in this study, as well as previously existing riverine data, will be compared with the results of this model to determine whether input from either can realistically explain the δ^{234}U systematic seen in the Mediterranean.

4.2 Sample overview

Locations of samples in the Mediterranean and nearby Atlantic stations can be seen in Figure 4.5, representing a total of 200 samples. This includes 139 samples collected by ship-based CTD systems in the Mediterranean Sea (95) or Atlantic (44), as well as 56 samples collected by hand-operated pumps from along the Mediterranean coast at Calanques de Marseille, near Marseille, France. An additional 5 samples were collected near Perpignan, France from two karstic springs draining into Lagoons connected to the Mediterranean Sea (Font Estramar and La Palme, (Bejannin et al., 2017)) as well as two locations near the outflow of two lagoons into the Mediterranean Sea, one with input from the Font Estramar spring and one

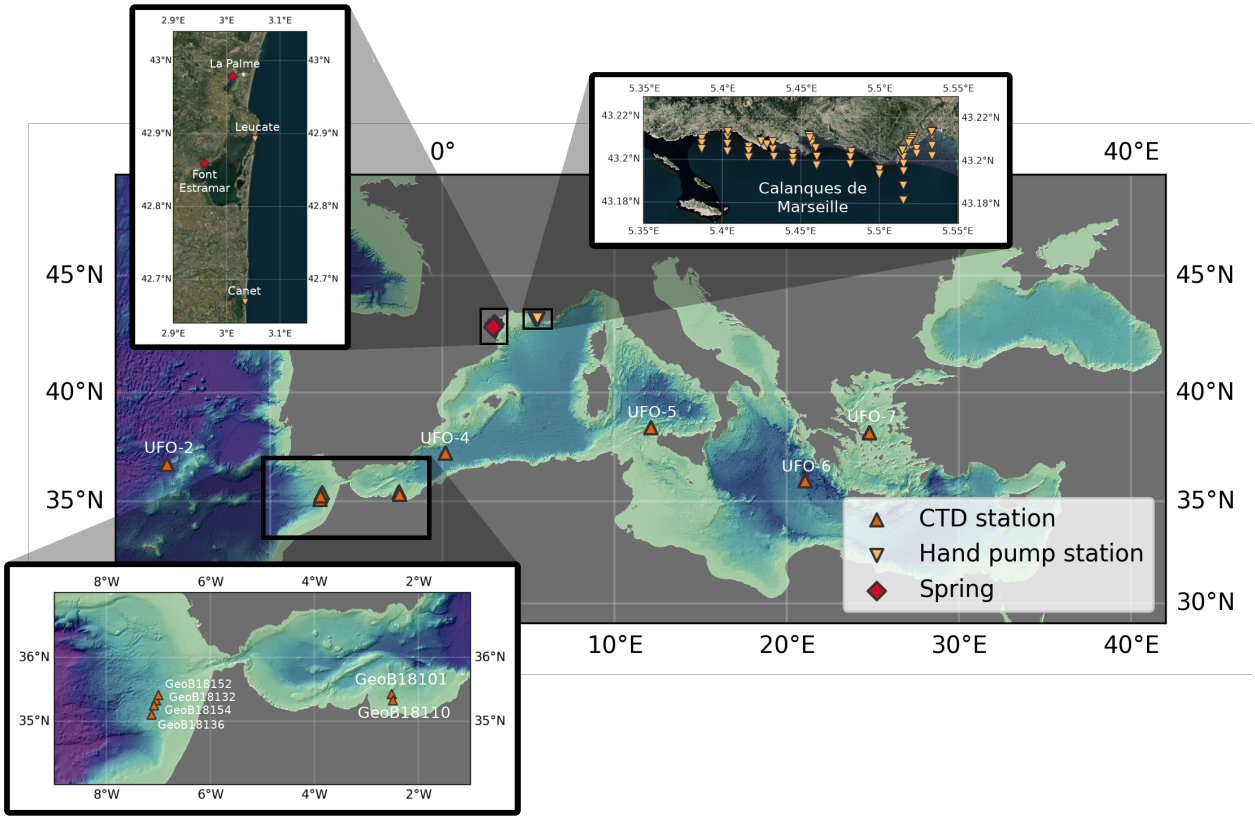

Figure 4.2: Sampling locations in the Mediterranean and nearby Atlantic. The top map inserts show a closer view of coastal sampling along the Western French Mediterranean Coast (left) and along the Calanques de Marseille (right). The bottom enlargement shows the closely spaced stations in the Gulf of Cadiz and Alboran Sea. 'Spring' here refers only to terrestrial springs, rather than SGD. Calanques samples were largely taken according to known SGD locations (Figure 4.3).

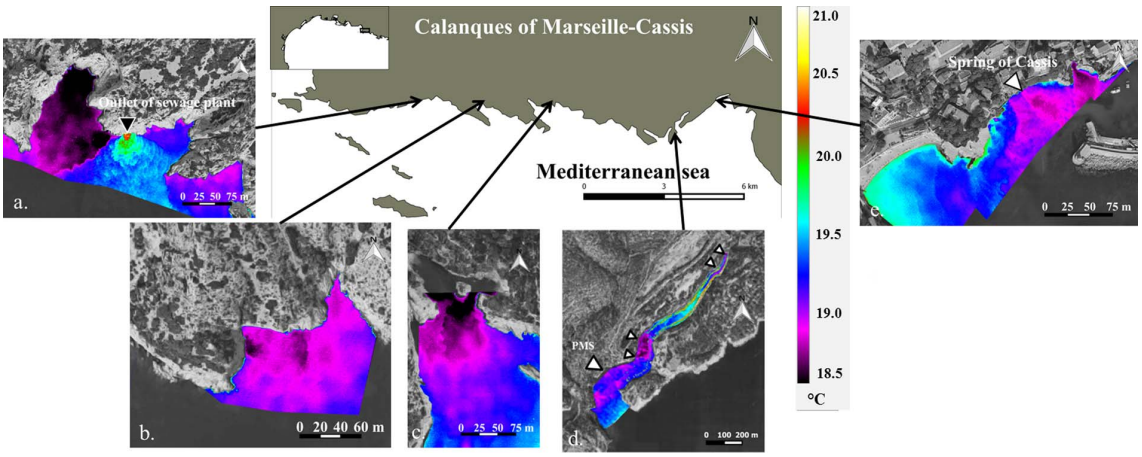

Figure 4.3: The five locations of strong SGD influence found by Bejannin et al. (2017). Aerial thermal imaging was used to find influence from cold SGD (a. Calanque of Cortiou, b. Calanque of Sormiou, c. Calanque of Sugiton, d. Calanque of Port Miou and e. Cassis). White arrows indicate known submarine springs according to Gilli (2001). Note that, in addition to SGD, Calanque of Cortiou (a) is influenced by ouflow from the main sewage plant in Marseille (warm signal). Figure taken from Bejannin et al. (2017).

without major spring-water influence. Calanques samples were taken in accordance with the previous investigation by Bejannin et al. (2017). In that study, aerial infrared imaging was used to find five major sources of SGD, through exploiting the typically cold temperature of groundwater (Figure 4.3).

These samples were collected across a number of cruises and projects. Samples from the Alboran Sea and Gulf of Cadiz (stations GeoB18101 to GeoB18154) were taken aboard the RV *Meteor* in 2014 during the MoccoMeBo cruise (Hebbeln et al., 2015). The remaining open-sea CTD samples (stations UFO-2 to UFO-7) are from the 2017 UFO cruise also aboard the RV *Meteor* (Frank, 2017). All coastal and springwater samples were collected in 2018. Overall sampled depths at CTD stations range from 13 m to 2971 m. Coastal samples (hand-held pump and springwater samples) were collected in 2018. These were generally taken at the water's surface, with the exception of samples taken near sources of SGD in the Calanques de Marseille, where the pump intake was placed as close to source of the discharge as possible, which may be up to two meters below the surface. All samples were stored, processed, and measured at IUP Heidelberg.

4.3 Results

Overall δ^{234}U show large variability, ranging from 145.9‰ to 1173.2‰. Samples from groundwater, or which are influenced by groundwater, (Figure 4.4) showed

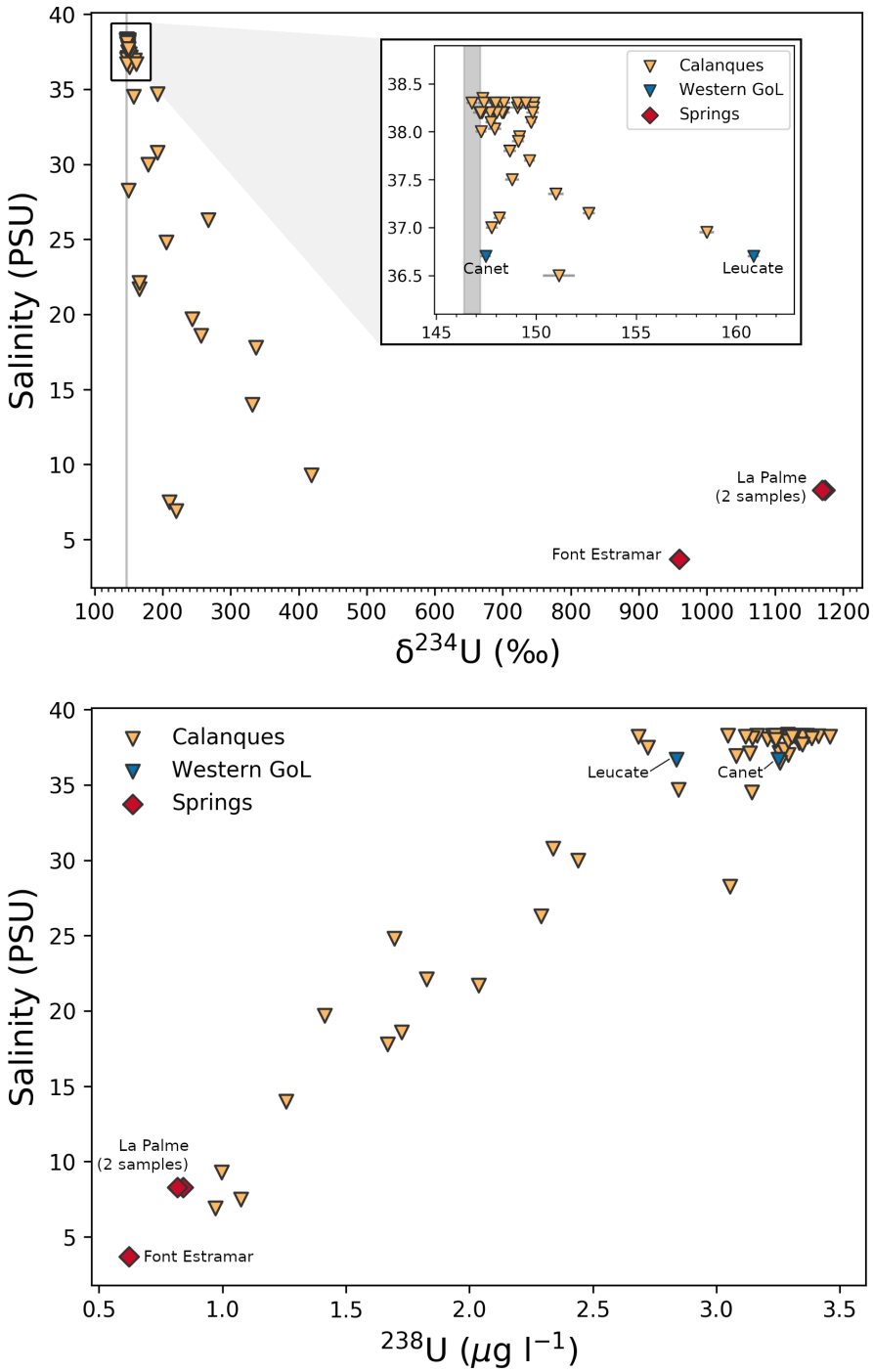

Figure 4.4: (Top) δ^{234}U results from all coastal samples (springs, hand pump stations). The hand pump stations from the Western GoL (Leucate and Canet) are colored blue to differentiate them from the Calanques de Marseille stations (yellow). The inset figure shows a zoomed in view of the upper right region of the main plot. The shaded vertical section represents the oceanic δ^{234}U from Andersen et al. (2010) of 146.8 ± 0.1‰. All errors are 2σ, although most are smaller than the plot symbols. (Bottom) Salinity vs. U concentration (^{238}U) for coastal samples.

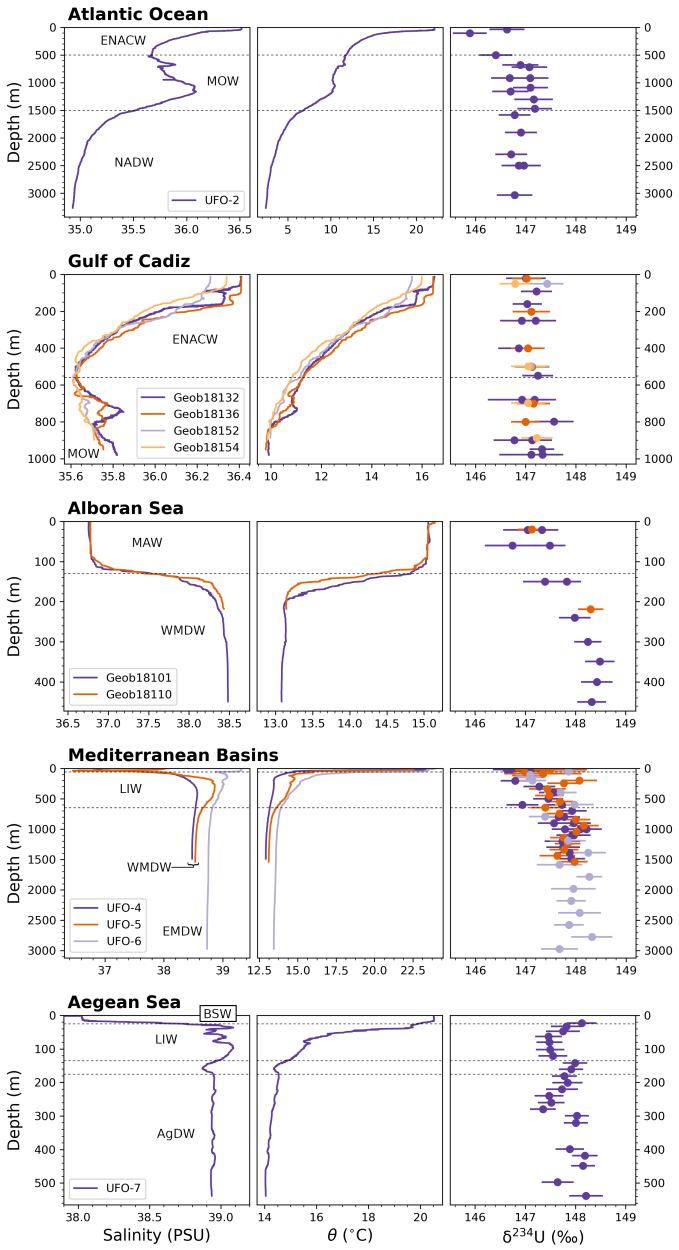

Figure 4.5: δ^{234}U results from CTD stations in the Mediterranean Sea and nearby Atlantic, arranged by region. The left two sections show salinity (in practical salinity units (PSU)) and potential temperature (θ) from CTD casts during sample collection. Major water masses are labeled as follows: Eastern North Atlantic central water (ENACW), Mediterranean overflow water (MOW), North Atlantic deep water (NADW), modified Atlantic water (MAW), Western Mediterranean deep water (WMDW), Levantine intermediate water (LIW), Eastern Mediterranean deep water (EMDW), Aegean Deep Water (AgDW), and Black Sea surface water (BSW). All δ^{234}U errors are 2σ.

much larger variability than those from open-sea CTD stations (Figure 4.5). The terrestrial springs had the highest δ^{234}U values, ranging from 959.5‰ to 1173.2‰. Hand-pump stations showed values which ranged from ocean-like (146.8‰) to highly enriched in ^{234}U (418.5‰). Samples from open-sea stations were overall much more similar to oceanic values than the coastal samples, however showed a much larger variation than would be expected in the open ocean, with values ranging between 145.9‰ and 148.3‰. Errors in δ^{234}U were typically ∼0.3‰, rising to 0.6‰ for samples with low (<10 PSU) salinity (such as groundwater and ground-water influenced samples) due to lower U content. Among CTD samples, U concentrations varied between 3.21 μg l^{-1} and 3.78 μg l^{-1} with negligible error. Concentrations increased in accordance with the salinity of the sample and showed no significant differentiation from the salinity-U relationship of ^{238}U (μg l^{-1})=(0.0919 ± 0.0005)∗salinity (99% confidence level) established by Chen et al. (1986), indicating that the Mediterranean did not show a depletion or enrichment of overall U with respect to the oceans. Coastal samples showed U concentrations which decreased with salinity, indicating that the groundwater end-members had both enhanced δ^{234}U and decreased U concentration. The lowest measured concentration was 0.62 μg l^{-1} for the Font Estramar spring.

Oceanic values from NADW (average δ^{234}U value = 146.8 ± 0.1‰ ($2\sigma_m$, n = 6) 2σ reproducibility = 0.2) show precise agreement with the reported global ocean δ^{234}U value of 146.8 ± 0.1‰ (2σ reproducibility = 0.4‰) from Andersen et al. (2010), speaking to the accuracy of measurements. Upper Atlantic values are strongly depleted compared to NADW, however the oceanic δ^{234}U provided by Andersen et al. (2010) relies almost entirely on samples from the Northern Pacific, including only two samples from the Atlantic, both of which are from depths of over 3000 m. As will be discussed later in Chapter 6, this is likely an Atlantic-wide trend, where the upper Atlantic is depleted in δ^{234}U while deep-waters more closely follow the Pacific.

The CTD-station δ^{234}U results shown in Figure 4.5 reveal an apparent systematic δ^{234}U enrichment on the scale of ∼1-2‰ in Mediterranean waters with respect to the ocean. This offset lies well outside of the 0.4‰ reproducibility of oceanic δ^{234}U from Andersen et al. (2010) and therefore represents a very significant and unexpected deviation from oceanic values. This differentiation can be most clearly observed in the Alboran Sea, where modified Atlantic water (MAW) overlays Western Mediterranean deep water (WMDW) and a just over 1‰ gradient is seen between shallow and deep samples. Realizing such fine differences (on the scale of 1‰) is only possible due to the precision offered by modern MC-ICP-MS, as previous studies using older, less-precise measurement techniques such as alpha spectroscopy (Koide and Goldberg, 1965) or thermal ionization mass spectrometry (Delanghe et al., 2002) found no difference between Mediterranean and Oceanic δ^{234}U. Results from the Aegean show a more complicated behavior than those from the Mediterranean at large. Rather than a general Trend of increasing δ^{234}U with depth, there is a pronounced rise in δ^{234}U near the surface and a possible bump at ∼160 m followed by a gradual decrease until ∼280 m. One reason for this difference in behavior is that the Aegean is far enough away from the SoG to not be affected by MAW, and instead the upper

~20 m are influenced by inflow from the Black Sea (BSW), which has a very high δ^{234}U signal on the order of 190‰ (Border et al., 2020). The uneven and irregular bathymetry of the Aegean contributes to a very complicated and dynamic circulation made up of numerous sub-water-masses (Millot and Taupier-Letage, 2006), which may be readily seen in the high variability of salinity and temperature over the CTD depth profile. Additionally, this station (UFO-7) was sampled at much higher vertical resolution than any other station, with 23 samples over a depth range of ~500 m (compared with e.g. UFO-6 with 17 samples over ~3000 m). Sampling other stations at similar resolution may show similar sub-water-mass variability.

The coastal results (Figure 4.4) show values which are all either at or above oceanic δ^{234}U. The extent of this enrichment generally appears to be strongly tied to decreasing salinity. Uranium concentrations show high correlation with salinity. Low salinity is indicative of a high degree of fresh groundwater influence, although higher salinity does not rule out influence from saline groundwater. As both U and salinity are in this case conservative tracers, if there were to exist one singular homogeneous 'groundwater' mixing end-member, the δ^{234}U and salinity from intermediate mixing between this and the Mediterranean would fall upon a singular mixing curve. This is not the case, as there is significant spread in the data, particularly at low salinities, indicating that there are significant differences in δ^{234}U and/or salinity of the various groundwater inputs. However, due to the overall enrichment of the samples it may be concluded that each of these inputs has a much higher δ^{234}U than is typical in the ocean.

4.4 Discussion

In this section, the previously reported results as well as their implications will be discussed. This will initially focus upon the CTD stations from the Mediterranean and nearby Atlantic looking into the geographical differentiation in δ^{234}U, which will afterwards enable the δ^{234}U fingerprinting of many of the major water masses present in the region. The focus will then shift to the coastal samples, to characterize some example SGD inputs into the Mediterranean. Finally, a box model of the Mediterranean, synthesizing these two aspects, will be introduced to provide a first look at overall U-input to the Mediterranean Sea, as well as which processes (i.e. rivers, SGD, inflow from the Black Sea) are the cause of the δ^{234}U offset which is observed.

4.4.1 Mediterranean δ^{234}U offset and water mass fingerprinting

To put the results seen in Figure 4.5 into oceanographic perspective, it is helpful to view them as a transect across the Mediterranean Basin. Figure 4.6 reveals the striking differentiation between various water masses in the Mediterranean Sea as well as the apparent relative homogeneity within these water masses. The extent of the

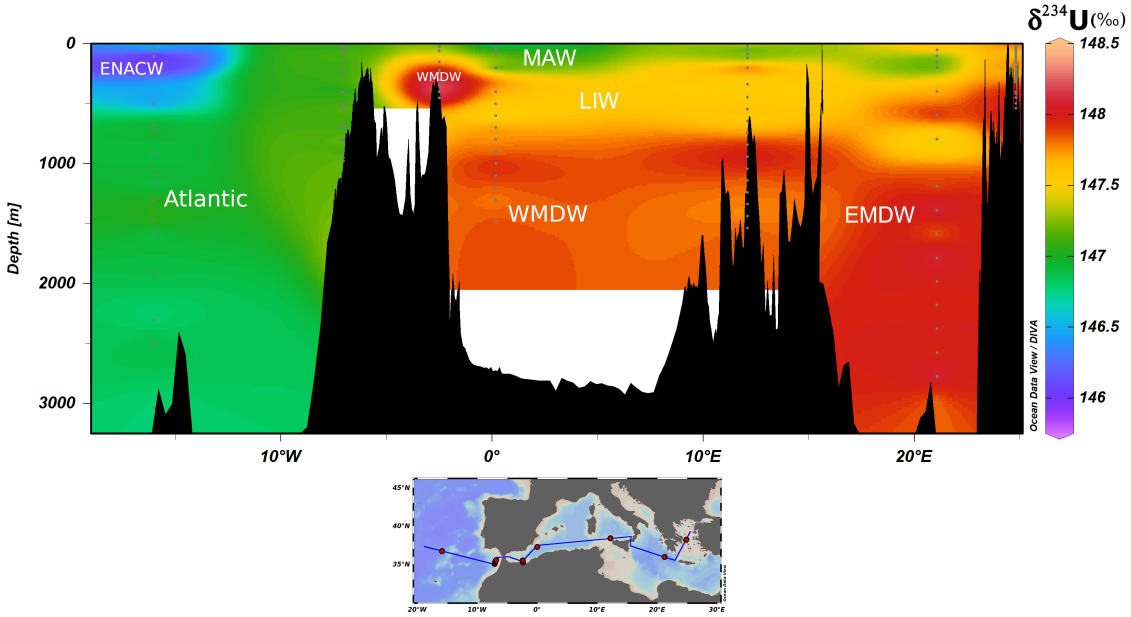

Figure 4.6: Sectional view of CTD-station δ^{234}U results across the Atlantic and Mediterranean, with major water masses labeled. The lower map shows the sectional track. Created using Ocean Data View (Schlitzer (2018)).

enrichment for each water mass correlates with its depth, which is itself correlated with the residence time of the water mass within the Mediterranean Basin (Millot and Taupier-Letage, 2006). MAW, which only recently entered the Mediterranean from the Atlantic, carries a near-oceanic signal which stretches across into the Eastern Basin. MDW (both WMDW and EMDW) show the highest enrichment of over 1‰. LIW, the intermediate water mass has a δ^{234}U signal which lies directly between these two extremes. All of this points towards the Ocean-Mediterranean δ^{234}U offset being the result of a large-scale U-input process within the Mediterranean. Likely candidates are either riverine input or SGD, as these are the typical pathways by which highly-soluble uranium enters the Ocean. This will be investigated further in Section 4.4.3.

To provide a clearer picture of the δ^{234}U differences between water masses present in the Mediterranean and nearby Atlantic, each is assigned an averaged 'fingerprint' value. This assumes that each water mass represents a homogeneous mixture, with internal variability being the source of all scatter. Figure 4.7 shows the major water masses in this study as well as several of their notable regional variants. Water masses are delineated as seen in Figure 4.5 based on salinity and temperature of the CTD profile. A mean value is reported for each water mass, with errors representing the $2\sigma_m$ measurement uncertainty (based on n measurements). The 2σ reported value is the external reproducibility of each water mass, shown as the shaded region for each water mass. As previously mentioned in Section 4.3, the NADW samples precisely agree with the global ocean δ^{234}U value from Andersen

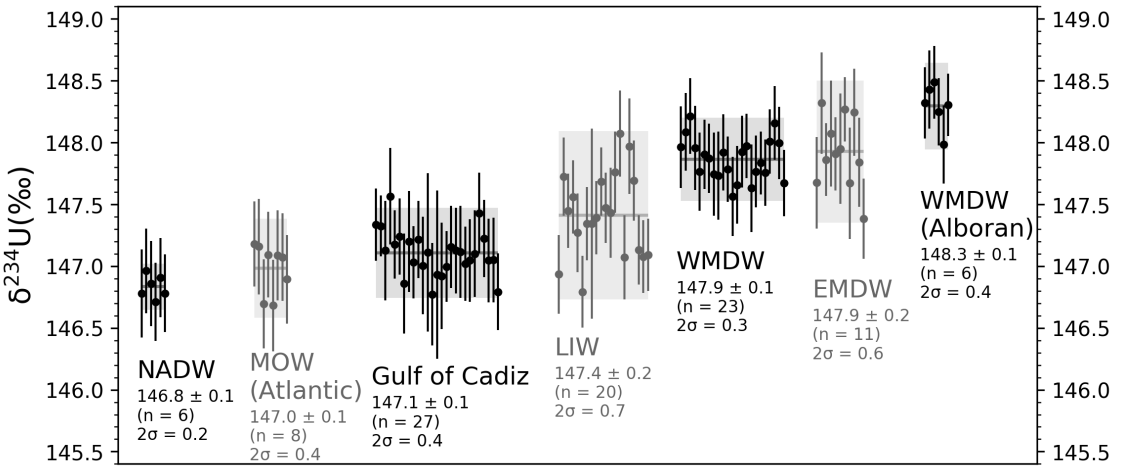

Figure 4.7: δ^{234}U fingerprints for various water masses across the Atlantic and Mediterranean. ENACW and MOW are both split geographically, into one open-ocean fingerprint and one fingerprint from the Gulf of Cadiz (GoC). Similarly, upwelled WMDW in the Alboran Sea has been fingerprinted separately. Shaded regions for each water mass represent the 2σ external reproducibility, while the errors listed with each fingerprint value is the $2\sigma_m$ measurement error based on n measurements.

et al. (2010), while major Mediterranean intermediate and deep water masses are outside of the reproducibility of 0.4‰. EMDW and WMDW (excluding the Alboran Sea) have identical δ^{234}U fingerprints of 147.9‰, which is interesting given that these water masses form separately on either side of the Strait of Sicily (sill depth ∼400 m). The only major water masses regularly traveling between basins are those at depths shallower than this sill, namely MAW and LIW (although there is a limited amount of upwelling on either side). As neither MAW or LIW have δ^{234}U levels as elevated as the two MDWs, yet both MDWs are equally enriched, this points towards whichever process is behind the elevated ^{234}U content functioning similarly in both basins. This would exclude, for instance, one large river being singularly responsible for elevated δ^{234}U in MDW, as this would disproportionately affect one basin over the other. This further indicates that the elevated δ^{234}U in the Mediterranean is likely due to a basin-wide effect rather than any anomalous localized input.

Upwelled WMDW in the Alboran Sea showed the highest δ^{234}U fingerprint, with a value of 148.3 ± 0.1. It is not entirely clear why this sub-water-mass is enriched with respect to the main body of WMDW. While mixing of water masses does occur in the Alboran Sea, it seems unlikely that this would have caused the elevated δ^{234}U fingerprint in Alboran Sea WMDW, as WMDW is already the most enriched water mass which has been measured. Additionally, the Alboran Sea WMDW samples are on average ∼0.05 PSU less saline and 0.07 $^{\circ}C$ warmer than those from within WMDW at UFO-4 or UFO-5 which, when combined with higher δ^{234}U, could be indicative of influence from cold, fresh, high-δ^{234}U SGD. As this influence is not

seen at the nearby UFO-4 station, this gives some clues as to where this input may have occurred. When WMDW is upwelled in the Alboran Sea, it is forced southwards, where it slowly travels along the Moroccan coast (Kinder and Bryden, 1990). SGD influence from the Moroccan coast could then lead to enrichment in Alboran Sea WMDW while leaving WMDW at station UFO-4 largely unaffected. Another possibility is that the Alboran Sea WMDW originates from currents closely hugging the French and Spanish coast, which then circumvents the open-sea station UFO-4 before being upwelled into the Alboran Sea. This would allow the inputs to occur in the Northern Mediterranean, where this study has shown there to be several sources of high-δ^{234}U-input through SGD and springs.

Among the water masses presented in Figure 4.7, LIW shows the largest variability in δ^{234}U, with a 2σ reproducibility of 0.7‰. LIW is the largest Mediterranean water mass by formation volume (Millot and Taupier-Letage, 2006), which stretches across the entire Mediterranean, sandwiched between MAW and MDW. Additionally, it is the saltiest of Mediterranean waters, which makes it very susceptible to vertical mixing due to decreasing the density gradient in the water column (Robinson et al., 2001a). This augments the effect of mixing events, such as temperature-driven vertical mixing in winter, or mixing driven by Ekman transport. This leads LIW to be a water mass which is highly variable, generally defined only as a salinity peak in the water column (Sparnocchia et al., 1994). Looking at the CTD data from the Mediterranean Basin stations in Figure 4.5, this inhomogeneity in LIW can be clearly seen both in the relative 'irregularity' of the salinity and temperature curves within the water mass (when compared to the 'smoothness' of e.g. MDW) as well as the significant differences between the three stations. It therefore follows that LIW would show a much more scattered δ^{234}U signal than other, comparatively more homogeneous water masses, analyzed.

Figure 4.7 includes two instances of likely influence from Mediterranean δ^{234}U in the Atlantic: enriched δ^{234}U values in MOW and across the water column in GoC. MOW, which can be identified at station UFO-2 in Figure 4.5 by the large deviation in salinity between ∼500 m and 1500 m, has a δ^{234}U fingerprint of 147.0 ± 0.1‰. This is only slightly elevated compared to NADW and much lower than either LIW or WMDW (which combine to make up the initial MOW at SoG (Robinson et al., 2001a)). However MOW at the location of UFO-2 is not the same water mass as it was near the SoG. While the MOW flows and spreads out in the Atlantic, it experiences significant mixing with other Atlantic water masses. This can be seen in the CTD data at UFO-2 (Figure 4.5), where the MOW salinity 'peak' reaches a salinity of ∼36 PSU, compared with the LIW and WMDW salinities which are well over 38 PSU. Assuming that the salinity peak accounts for ∼0.5 PSU (as well as assuming a smooth salinity gradient without MOW influence and therefore a salinity of ∼35.5) this would imply that MOW at the location of UFO-2 is made up of only roughly 1/6th Mediterranean Water, with the rest being mixed in Atlantic water. This ∼0.2‰ offset in Atlantic MOW from NADW would then fit relatively well with an initial outflow from the Mediterranean which had a δ^{234}U signature (consisting of mixed LIW and Alboran WMDW) of ∼148‰. Samples from GoC show a light

δ^{234}U enrichment with an average value of 147.1 ± 0.1‰. This slight offset persists across the water column, with no discernible differentiation between the upper 580 m (ENACW, $\delta^{234}\text{U} = 147.1 \pm 0.1$‰ (n = 15)) and $\sim$ 400 m below this (MOW, $\delta^{234}\text{U} = 147.1 \pm 0.1$‰ (n = 12)). These two have therefore been combined as 'Gulf of Cadiz' in Figure 4.7. While the elevated δ^{234}U in the MOW portion of the GoC water column is no surprise, it is less clear what causes this same signal to be present in ENACW, particularly given the strongly depleted nature of ENACW samples from station UFO-2 (Figure 4.5). One possible explanation is that strong upwelling, a near constant feature at various locations in the Northern GoC (García-Lafuente et al., 2006), leads to a slight mixing-in of underlying MOW with the overlying ENACW, raising the δ^{234}U of the overall water mass. This signal would then be circulated with ENACW along the coast of GoC and eventually to the location of GoC stations, along the Moroccan coast.

In all, elevated δ^{234}U levels are found in sea-water across the Mediterranean Sea at levels which lie well outside previously published determinations of global oceanic values. This variability is not randomly distributed, but rather each major water mass in the Mediterranean Basin is able to be given a distinct δ^{234}U fingerprint. The extent of the δ^{234}U offset from oceanic values correlates with the 'age' of each water mass within the Mediterranean which, along with the uniformity between the two MDW water masses points towards the source of this additional ^{234}U being a widespread effect. The highest δ^{234}U values were seen in the Alboran Sea, where WMDW has been assigned a fingerprint of 148.3 ± 0.1‰. The effects of this elevated δ^{234}U in the Mediterranean extend to the Atlantic, where samples from the Gulf of Cadiz, as well as MOW in the open-ocean, show slightly enriched δ^{234}U.

4.4.2 Investigating Mediterranean coastal groundwater U-input

Samples from the French Mediterranean coast show clear indication of influence from SGD. The results in Figure 4.4 exhibit strong correlations between a sample's salinity, ^{238}U, and δ^{234}U, which in this case points towards a groundwater mixing end-member which is fresh, low in U concentration, and high in δ^{234}U when compared to Mediterranean sea-water. Is is important to remember that this need not necessarily be the case, due to both the high degree of variability which has previously been observed in groundwater U content (Porcelli and Swarzenski, 2003; Suksi et al., 2006), as well as the potential for groundwater to be highly saline. Indeed, the fact that the presumable SGD seen here is so strongly differentiated from the Mediterranean in these three conservative tracers is what enables the investigation of U-inputs into the region, as it would otherwise be difficult to prove the extent of groundwater influence on each sample.

While all signs point toward SGD along the coast of the GoL being largely low-salinity, low U concentration, and high δ^{234}U, this does not mean that these inputs are homogeneous. For instance, looking at Figure 4.4, the La Palme spring has a

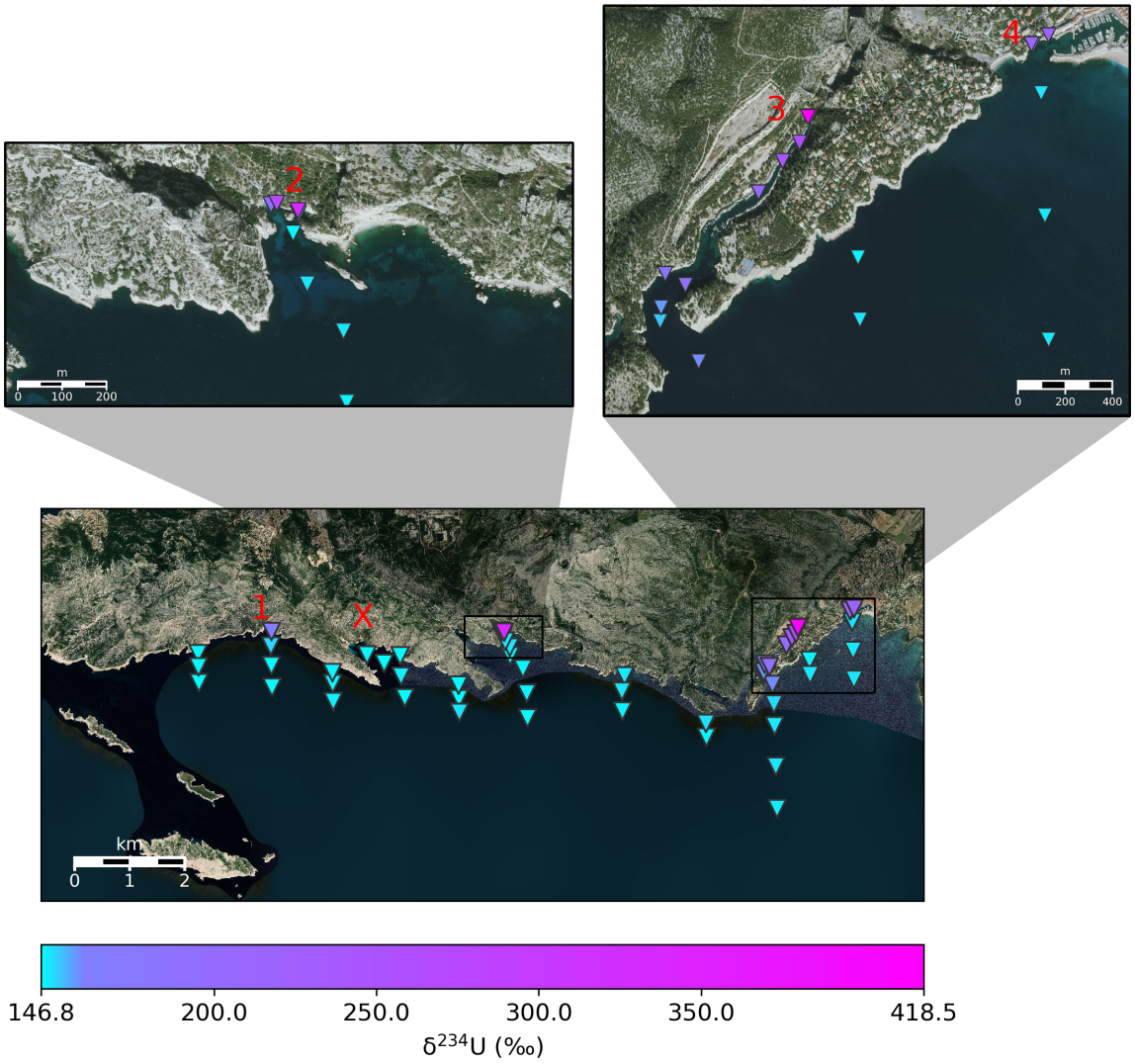

Figure 4.8: Calanques de Marseille results arranged geographically. Zooms of the two areas enclosed by black rectangles are seen in the two upper figures. Red numbers refer to the four SGD sources of δ^{234}U found in the study.

higher salinity than Font Estramar while also having higher U concentration and higher δ^{234}U. Similarly, the highest δ^{234}U (418.5‰) from the Calanques samples has higher salinity than other samples with much lower δ^{234}U (∼210‰). Such situations would be impossible in a conservative two end-member mixing scenario, were there to be no regional variation in the SGD end-member. So although the detected SGD influence is overall similar with respect to Mediterranean seawater makeup, there are significant differences between SGD sources.

To investigate individual SGD sources, Figure 4.8 shows the δ^{234}U results from the region plotted geographically. Four of the five SGD sources found by Bejannin et al. (2017) along the Calanques de Marseille show up as large δ^{234}U anomalies, well above values found in Mediterranean seawater. No other location showed a similar degree of enrichment. These four locations are shown labeled 1-4 in Figure 4.8 (with the fifth location as X) and will hereafter be referred to as SGD 1-4. There are a number of possible reasons why the fifth SGD location does not show a recognizable δ^{234}U signal (e.g. no SGD, SGD signal matches seawater), although it is most likely a sampling issue. During sampling, an attempt was made to sample as near as possible to each SGD outflow, however at this location no significant individual source was able to be found. The stations in this area are therefore likely too far from the SGD source itself (which may in fact be many small disparate sources) for a significant, undiluted δ^{234}U signal to be measured.

To look at finer δ^{234}U differences, particularly in samples away from the SGD sources themselves, Figure 4.9 shows the same results on a scale more relevant to Mediterranean Seawater. At each of SGD 1-4 significant influence (δ^{234}U $>$ ∼149‰) can be seen even at stations away from the source itself. The fifth presumed SGD location (X) still shows at best minimal evidence of SGD influence, with one nearby station having a δ^{234}U of ∼ 148.5‰. Regardless, stations closer to the presumed SGD have lower values, which may indicate that even this small signal is of a different origin. Overall SGD influence is especially noticeable in the eastern portion of the sampled area, where most stations, even those located kilometers offshore, have δ^{234}U signatures of over 149‰. As the SGD influence extends into all eastern samples, the geographical extent of this influence is impossible to ascertain without further sampling. Overall there is large variation in δ^{234}U among samples which may be considered to have 'seawater-like' salinities, indicating that the different SGD inputs are exerting substantial (if localized) impacts on the δ^{234}U of Mediterranean water itself. As seen in Figure 4.4, among samples with a salinity of over 38 PSU (considered higher than most surface water in the Western Mediterranean Basin), δ^{234}U values show an overall range of over 3‰, from 146.8‰ to 150.0‰, and little (if any) correlation between salinity and δ^{234}U. This means that, despite having very similar salinities, seawater samples from near the Calanques showing variation in δ^{234}U on a scale 3-4x larger than that seen among all Mediterranean CTD samples. The average δ^{234}U value for samples above 38 PSU is 148.3‰, on par with the highest δ^{234}U water mass fingerprint (Alboran Sea WMDW). If looking only at seawater samples originating from east of 5.5 E (corresponding with the bay where SGD-3 and -4 are located), that average climbs to 149.0‰. The SGD near the Calanques is

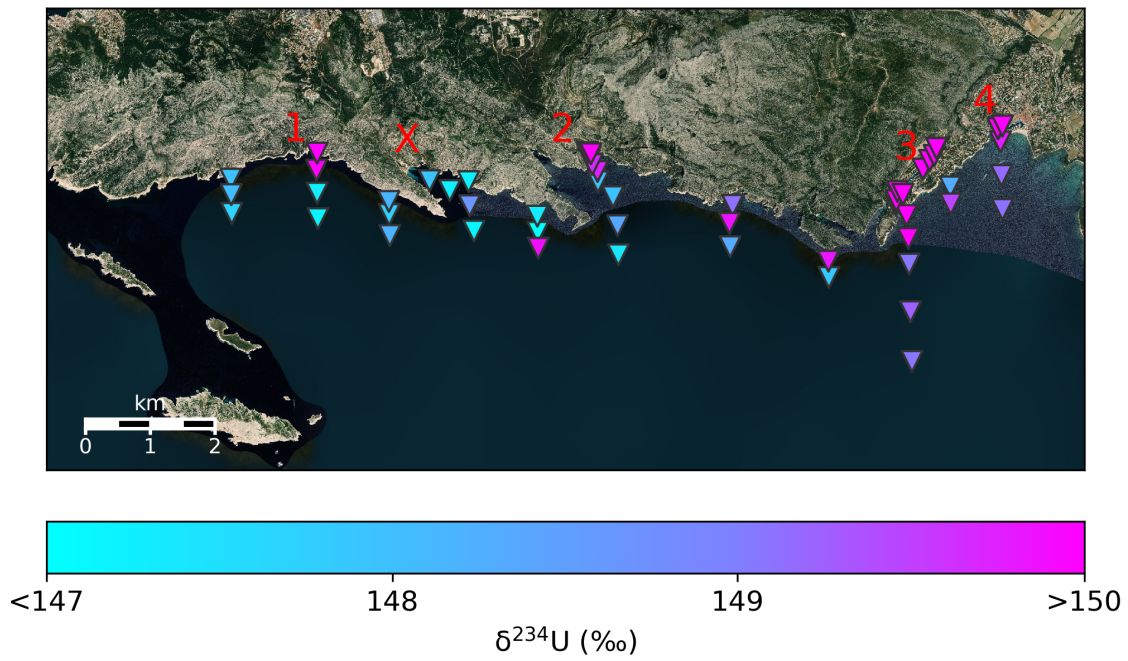

Figure 4.9: The results from Figure 4.8 re-scaled to more easily see differences in seawater samples. The signal from SGD sources 3 and 4 can be seen to propagate into nearby seawater samples, with nearly all eastern samples having δ^{234}U values of over 149‰. The fifth SGD source identified in Bejannin et al. (2017) (X) also shows no consistent SGD signal at this scale.

clearly exerting a very large impact on the U-isotopic makeup of regional seawater.

Now that these four SGD U-sources in the Calanques have been identified and their effects on the nearby Mediterranean observed, the differences between these sources will be investigated with the use of a 'Keeling Plot' (Keeling, 1958; Pataki et al., 2003). This involves plotting the isotopic composition of measured samples (here: δ^{234}U) against the reciprocal concentration (here: $1/^{238}$U). Samples which are the result of mixing between two shared end-members will lie along a straight line. If a sample is affected by more than two end-members, the system falls apart and no linear relationship will be seen. Figure 4.10 shows a Keeling Plot of the Calanques samples, with each sample colored according to the SGD source (SGD 1-4) which it is geographically closest to. Springs from the western GoL are also included for comparison. A linear regression has been made for each grouping of samples, displayed as a line with matching color. Outside of the clumped seawater samples in the lower-left of the figure, there are very strong linear relationships for each data grouping (particularly so for SGD 2-4). This indicates that these samples are the product of two end-member mixing between seawater and their respective groundwater end-member. For the seawater samples bunched in the lower left, the linear relationship is either much less clear or non-existent, indicating that these samples are influenced by multiple U-sources and no longer in the two end-member regime.

Theoretically each groundwater end-member can lie anywhere along its respective mixing line, as long as each sample lies between it and the seawater end-member. Among the four SGD sources, only SGD-1 and -4 appear to be similar, while the others vary significantly. For the sake of comparison, if equal end-member concentrations of 1 μg l^{-1} were assumed for each Calanques SGD source, SGD-2 would have the highest δ^{234}U of $\sim$ 600‰, followed by SGD-3 with $\sim$400‰, and SGD-1 and -4 which would have the lowest with $\sim$200‰. Although these SGD sources are located quite close to one another geographically, they show significant variation in their U characteristics.

One interesting feature of Figure 4.10 is that the Font Estramar spring lies very close to the SGD-2 fit line. Given that these two locations are separated by approximately 200 km, this does not mean that they share a mixing end-member. It does, however, indicate that both sources have the potential to exert impacts on the U composition of local seawater which would be indistinguishable from one another. The La Palme spring, by comparison, lies well above both Font Estramar and all of the Calanque SGD mixing curves. It follows therefore that two-member mixing between La Palme and seawater has the greatest potential for δ^{234}U enrichment at comparable concentrations.

Evidence of influence from groundwater (albeit in this case not strictly SGD) can also be found in the two Western GoL samples. The Canet and Leucate samples both have a salinity of 36.7 PSU and are separated by a mere 20 km, yet have δ^{234}U signatures (Leucate: 160.9‰, Canet: 147.5‰) which differ by $\sim$13‰. This is likely due to the differences in nearby groundwater input. The Leucate sample lies next to Leucate Lagoon, which is fed by both the Font Estramar spring (δ^{234}U = 959.5‰) as

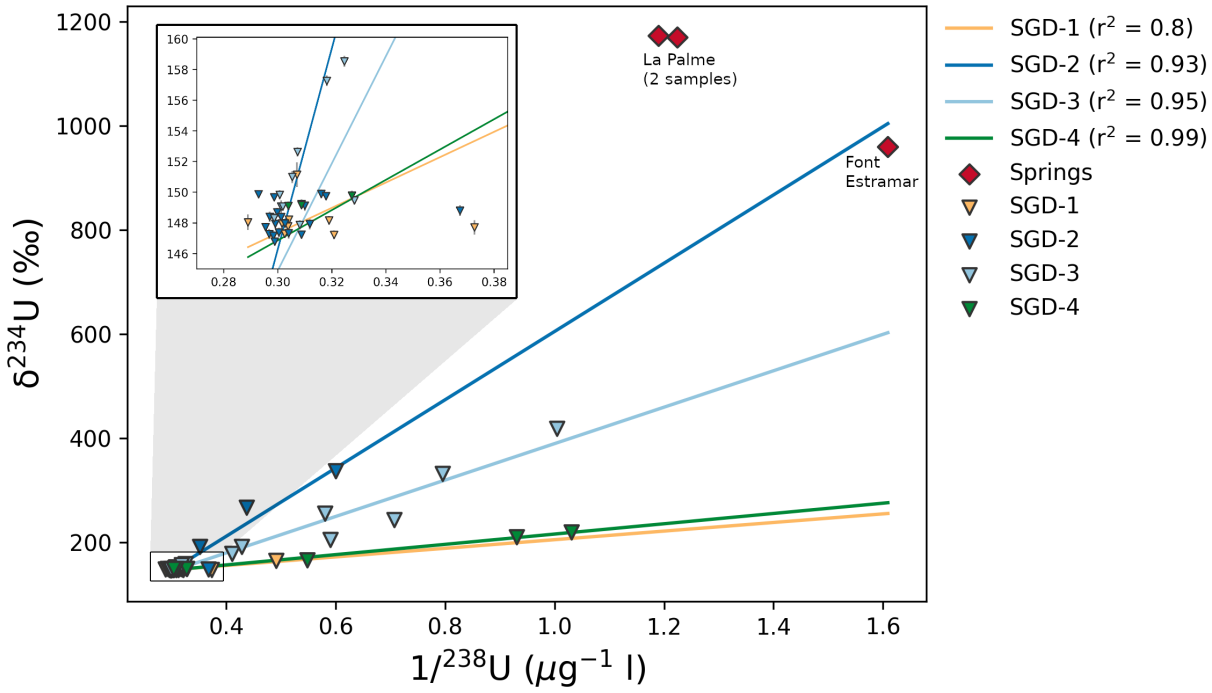

Figure 4.10: Keeling plot (δ^{234}U against $1/^{238}$U) of samples from Calanques de Marseille (inverted triangles), with spring samples from western GoL (diamonds) for reference. Calanques samples are colored according to which of the four SGD sources identified in Figure 4.8 they are located closest to. Lines with matching colors denote the linear regression of all samples from within each grouping. r^2 values for each line are found in the legend.

well as significant SGD (Stieglitz et al., 2013). Additionally, the La Palme Lagoon lies nearby and is fed by both the La Palme spring (δ^{234}U = 1173.2‰) as well as several other karstic springs (Carlier et al., 2008). By contrast, the Canet sample was taken just outside of the Canet Lagoon for which inputs are dominated by river inputs (Carlier et al., 2008). While many more samples would be needed to analyze these samples with a similar thoroughness to those from the Calanques, this does provide an example of a seawater δ^{234}U enrichment, likely being brought about by groundwater influence, taking place at a second location in the Mediterranean.

Here, multiple instances of groundwater influence on coastal seawater in the Mediterranean Sea were shown. Direct evidence for seawater δ^{234}U enrichment was able to be seen, which was in many cases concluded to be the product of two end-member mixing between seawater and SGD. Still, these results do not provide any sort of temporal information, which would allow the determination of U flux or SGD volume flow rates. Without such knowledge, it is impossible to differentiate whether the δ^{234}U enrichment seen in many samples is the result of small amounts of SGD influence over long time-scales or large amounts of SGD influence over short time-scales. In the next section, a basin-wide approach will be taken, which allows for the use of SGD volume flow rate estimations from previous basin-wide studies.

4.4.3 Modeling overall U-inputs to the Mediterranean Sea

In Section 4.4.1 it was shown that the Mediterranean has a significant δ^{234}U offset of over 1‰ compared to the oceans. Section 4.4.2 investigated multiple instances of high-δ^{234}U SGD input to the Mediterranean, as well as their effect on the δ^{234}U of nearby seawater. This section will attempt to combine these two aspects, along with previously published data, into a simple box model to look into what typical Mediterranean U-input would need to be for such a Mediterranean-Ocean δ^{234}U offset to occur.

A schematic view of the model is outlined in Figure 4.11. It consists of five primary pieces:

- the Mediterranean basin (box)
- known inputs (Atlantic and Black Sea inflow), with defined volumetric flow, ^{238}U and δ^{234}U
- radioactive decay of ^{238}U and ^{234}U
- outflow from Mediterranean
- unknown inputs (SGD and rivers), for which volumetric flow is known while concentration and δ^{234}U will be determined.

For the purposes of the model, Mediterranean water is assumed to have a uniform δ^{234}U and ^{238}U of 147.9 ± 0.1‰ and 3.54 ± 0.01 μg l^{-1} respectively. These are the values for combined (that is, EMDW and WMDW) MDW, which accounts for the

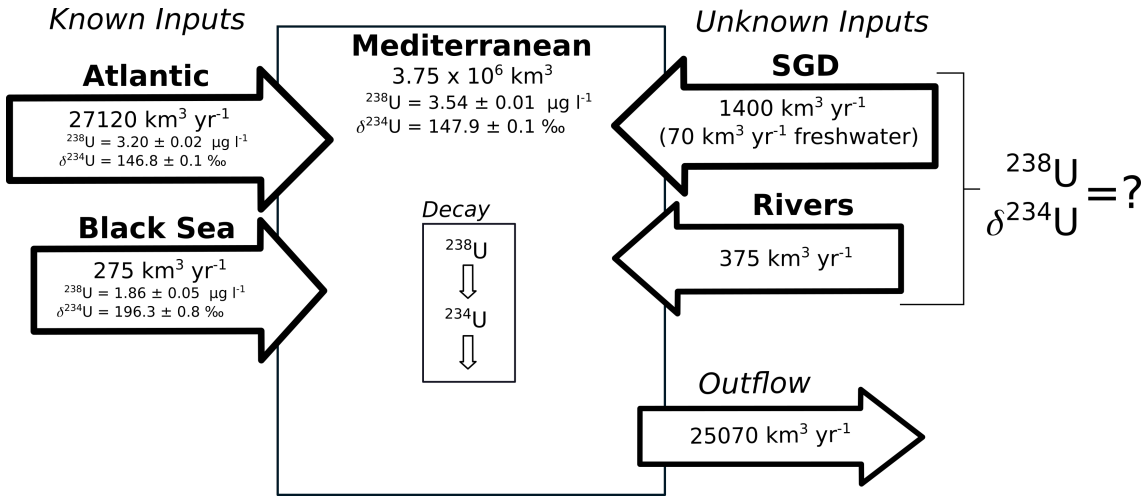

Figure 4.11: Schematic view of the box model for estimating the U concentration and δ^{234}U of the combined river and SGD input to the Mediterranean Basin. Inputs are represented in terms of their volumetric flow of water, uranium concentration (^{238}U) and δ^{234}U. ^{238}U decay to ^{234}U excludes the short lived intermediate isotopes of ^{234}Th and ^{234}Pa. SGD inflow is from Rodellas et al. (2015), with all other water fluxes from Jordà et al. (2017). Atlantic ^{238}U and δ^{234}U are from Chen et al. (1986) and Andersen et al. (2010) respectively. Black Sea ^{238}U and δ^{234}U are from Border et al. (2020). Mediterranean ^{238}U and δ^{234}U are the values for MDW from Section 4.4.1.

vast majority of Mediterranean water by volume. Water fluxes into and out of the Mediterranean are from Jordà et al. (2017) with the exception of SGD inflows (both general and the freshwater component) which are from Rodellas et al. (2015). The uranium values for the Atlantic are the oceanic values from Chen et al. (1986) and Andersen et al. (2010), while Black Sea values are from Border et al. (2020). All inputs and fluxes are assumed to be constant with respect to time.

The model will provide a novel insight into the average δ^{234}U and U concentration of combined SGD and riverine inputs into the Mediterranean. These two inputs, SGD and rivers, must be looked at together as there is no feasible way of differentiating between them. This may become possible in the future, if the uranium content of Mediterranean rivers were to become more well studied, allowing the riverine portion to be extracted and thereby leaving behind the remaining SGD portion. At the time of writing however, such studies are very limited, with only the Rhône River (among major Mediterranean rivers) having been measured for both U concentration (Ollivier et al., 2011) and δ^{234}U Zebracki et al. (2017). Although this is not enough to separate rivers from SGD for the purpose of this analysis, it will serve as a baseline (along with the average global riverine U isotopic makeup from Chabaux et al. (2003)) for comparison. For the sake of clarity the combined river and SGD input will hereafter be referred to as SGD+R.

The basis for construction of the model is mass conservation. In this case, there are in fact two systems for which mass must be conserved, ^{234}U and ^{238}U. As ^{238}U decays (via the short-lived intermediate products ^{234}Th and ^{234}Pa) into ^{234}U, these two systems are join with one another. The model is assumed to be in steady-state, which means that for each mass-balance inputs and outputs must be equal. For ^{238}U, this is relatively trivial, giving:

$$C_{med}\left(k_{out} + \lambda_{^{238}U}\right) = k_{atl}C_{atl} + k_{bs}C_{bs} + k_{sgd+r}C_{sgd+r} \tag{4.1}$$

where the left side of the equation represents U removal and the right side is U-input. C_{med}, C_{atl}, C_{bs}, and C_{sgd+r} represent the concentrations of the Mediterranean, Atlantic, Black Sea, and SGD+R respectively. The k_x values are the associated input/removal rates, defined as the volumetric flow rates divided by the volume of the Mediterranean. $\lambda_{^{238}U}$ is the decay rate of ^{238}U.

A similar formulation can be extended to ^{234}U, with the addition of a term describing the input of ^{234}U due to the decay of ^{238}U:

$$C_{4,med}\left(k_{out} + \lambda_{^{234}U}\right) = k_{atl}C_{4,atl} + k_{bs}C_{4,bs} + C_{med}\lambda_{^{238}U} + k_{sgd+r}C_{4,sgd+r} \tag{4.2}$$

where $C_{4,x}$ represents the concentration of ^{234}U as opposed to the overall U concentration (which is generally approximated to be equal to that of ^{238}U). Through rearranging the definition of the ^{234}U/^{238}U activity ratio, the $C_{4,x}$ values may be formulated in terms of overall U concentration (C_x) and activity ratio (A_x),

$$C_{4,x} = A_x C_x \frac{\lambda_{^{234}U}}{\lambda_{^{238}U}} \tag{4.3}$$

which, when substituted back into Equation 4.2 gives:

$$A_{med}C_{med}\left(k_{out}+\lambda_{^{234}U}\right)=k_{atl}A_{atl}C_{atl}+k_{bs}A_{bs}C_{bs}+C_{med}\lambda_{^{234}U}+k_{sgd+r}A_{sgd+r}C_{sgd+r} \tag{4.4}$$

Finally, combining Equations 4.1 and 4.4 and subsequently solving for A_{sgd+r} gives:

$$A_{sgd+r}=\frac{1}{k_{sgd+r}C_{sgd+r}}\left[\left(\frac{A_{med}\left(k_{out}+\lambda_{^{234}U}\right)-\lambda_{^{234}U}}{k_{out}+\lambda_{^{238}U}}\right)\left(k_{atl}C_{atl}+k_{bs}C_{bs}+k_{sgd+r}C_{sgd+r}\right)-k_{atl}A_{atl}C_{atl}-k_{bs}A_{bs}C_{bs}\right] \tag{4.5}$$

where the activity ratio of SGD+R is defined in terms of the U content of the Mediterranean Sea as well as its inputs and removals. As a reminder, the activity ratios discussed here are not equal to the δ^{234}U values. δ^{234}U is an expression of the activity ratio in δ-notation ($\delta^{234}U_x=(A_x-1)\times 1000$). This is useful when discussing small isotopic differences however the formulation of Equation 4.5 is much clearer in terms of A_x. For discussion of the results δ^{234}U will be used.

Figure 4.12 shows the resulting curve from Equation 4.5 plotted over a range of SGD+R U concentrations. It should be noted that this curve is independent of the measured U concentration in the Mediterranean as the overall δ^{234}U value in the Mediterranean Sea could theoretically be equally affected by both a low-concentration, high-δ^{234}U-input or a high-concentration, low-δ^{234}U input. Nevertheless, the concentrations of U-inputs to the Mediterranean impact the U concentration in the Mediterranean Sea. According to Equation 4.1, a second x-axis is created which shows the respective C_{med} for each C_{sgd+r} (Figure 4.12, top). The gray shaded region corresponds with the measured ^{238}U in the Mediterranean (3.54 ± 0.01 μg l^{-1}) and constrains the possible concentrations (and by extension δ^{234}U) of SGD+R. Using this, the model predicts that the ^{238}U and δ^{234}U of SGD+R into the Mediterranean Sea are approximately 0.8 ± 0.1 μg l^{-1} and 200 ± 10‰ respectively.

To put this estimation into context, Figure 4.12 also includes a number of reference values. From this study, the springs (Font Estramar and La Palme) as well as the most representative end-member sample from each of the four Calanques de Marseille SGD source are shown. External riverine data, for both the Rhône River (Ollivier et al., 2011; Zebracki et al., 2017) and a worldwide U isotopic average from 35 major rivers around the globe (Chabaux et al., 2003) are also included. According to the model, SGD-4 is closest to be representative of average SGD+R input. in a more general sense, this dataset highlights that SGD is likely the primary contributor towards the δ^{234}U offset seen in the Mediterranean. While rivers make up only around ~21% of SGD+R input, evidence points towards their δ^{234}U being much too low to raise Mediterranean δ^{234}U to such an extent as is seen. The Rhône is the largest river by volume draining into the basin, representing approximately

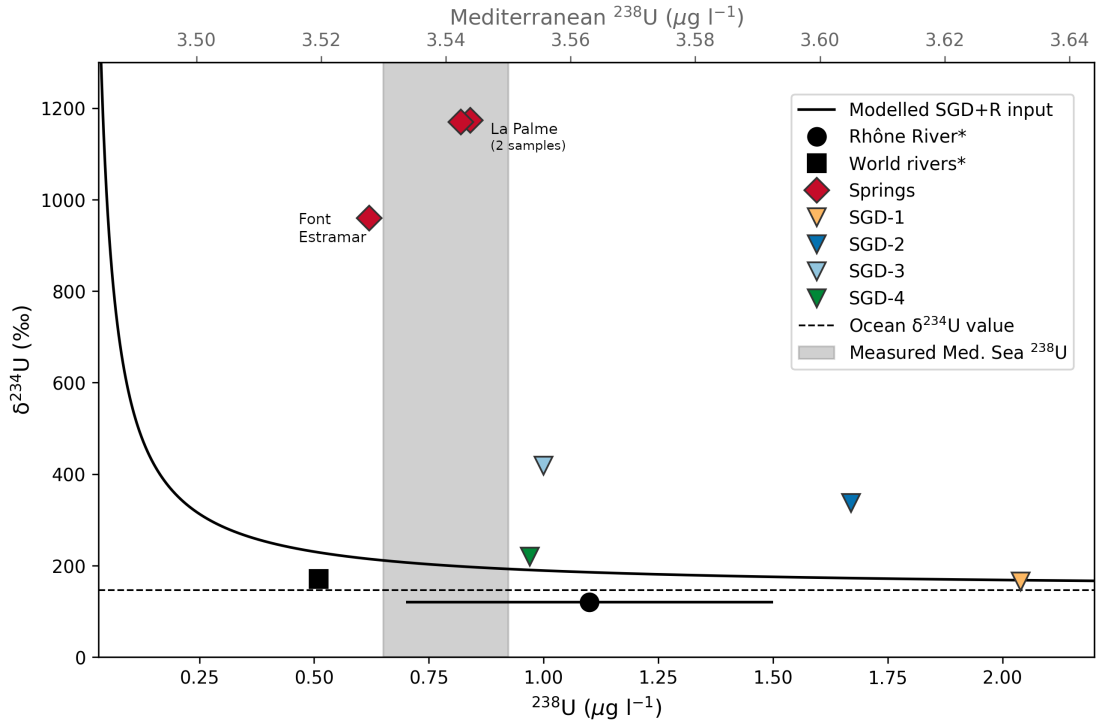

Figure 4.12: Modeled input (black curve) from SGD and rivers into the Mediterranean Sea according to Equation 4.5 in terms of U concentration (^{238}U) and δ^{234}U. The top axis is the modeled Mediterranean U concentration, which is related to the input U concentration through Equation 4.1. The shaded region is the U concentration measured in EMDW and WMDW in this thesis. The oceanic δ^{234}U value of 146.8 ± 0.1‰ as determined by Andersen et al. (2010) is represented by the dashed line. Rhône River U concentration and δ^{234}U are from Ollivier et al. (2011) and Zebracki et al. (2017) respectively. The world rivers data point is the average value of U concentration and δ^{234}U from world rivers as compiled by Chabaux et al. (2003).

one-seventh of all Mediterranean river input and yet has a δ^{234}U which is lower even than the Atlantic. The world-wide riverine average is enriched compared to the oceans, but still lays well below the modeled SGD+R curve. If either of these is representative of overall riverine input, then rivers do not play a significant role in creating the Mediterranean δ^{234}U offset.

SGD samples on the other hand all lie above the modeled SGD+R curve. Were these samples to be representative of the overall SGD input to the Mediterranean, the observed offset would be even larger. It is important to again emphasize that SGD is a wide-reaching term, which includes many 'varieties' of groundwater flowing into a given body of water (Moore, 2010). What has been measured here is largely fresh near-shore SGD, driven by both terrestrial (e.g. freshwater recharge) and physical oceanic forces (e.g. tidal pumping), while offshore SGD driven by geothermal heating and overpressurized zones within the sediments has not yet been studied. Rodellas et al. (2015) estimates the vast majority of Mediterranean SGD to be saline. Together, this may indicate that offshore/saline SGD tends towards lower δ^{234}U which, when averaged with the high δ^{234}U coastal/relatively fresh SGD, results in an average SGD input which is more in line with the model prediction.

4.5 Summary

The Mediterranean exhibits an offset in δ^{234}U with respect to the world's oceans of ~1-2‰. This is small enough to only be observable when measuring with modern high-precision MC-ICP-MS, yet is well outside of the established range of oceanic δ^{234}U variation. The differentiation was even seen among water masses within the Mediterranean, which were able to be fingerprinted for δ^{234}U. Very slight evidence of Mediterranean influence, in the form of elevated δ^{234}U, was able to be seen in both samples from the Gulf of Cadiz as well as within Mediterranean Overflow Water in the East Atlantic. The highest δ^{234}U enrichment was found in Western Mediterranean Deep Water samples from within the Alboran Sea, which had an average δ^{234}U value of 148.3 ± 0.1‰. Within both the eastern and western basins, Mediterranean Deep Water showed a uniform signature of 147.9 ± 0.1‰.

To investigate whether Submarine Groundwater Discharge (SGD) could play a role in causing this offset, a number of samples were taken along the coast of the Gulf of Lions, as well as from two nearby coastal springs. These identified four suspected SGD sites in the Calanques de Marseille as sources of high-δ^{234}U, while the two springs exhibited the highest δ^{234}U among all samples measured (up to 1173.2‰). There was evidence of SGD having a significant influence on near-coastal samples which would be (due to salinity) classified as seawater, with samples at similar salinities in the Calanques region having δ^{234}U values which range over 3‰.

A simple mass-balance model of the Mediterranean U budget was constructed to investigate what a theoretical SGD + riverine (SGD+R) input would need to be in order for the observed offset to occur. The model showed that riverine input to the Mediterranean is unlikely to play a larger role in the creation of this offset, with

SGD likely to have a larger impact. The studied SGD/springs had higher δ^{234}U and U concentration than predicted by the model, indicating that other SGD varieties or locations are likely to have lower δ^{234}U and U concentration to balance this out. Of the SGD sources, riverine data, and springs, SGD-4 was the closest to the SGD+R δ^{234}U-input predicted by the model and therefore most representative of 'typical' U-input to the Mediterranean.

5 U systematics in the the Amazon River Estuary

5.1 Introduction

The Amazon is the world's largest river with a volumetric flow of 5.7 km^3 yr^{-1}, which alone accounts for approximately 20% of the total riverine input to the world's oceans (Meade et al., 1985). This is largely the result of having a gigantic, tropical catchment basin, covering over 6 million km^2 (Figure 5.1), which has the additional effect of dampening the interannual variability in its discharge (Nittrouer and DeMaster, 1996). The majority of dissolved constituents in the Amazon come from the Andes Mountains, which lie at the far western edge of the basin and account for only 13% of the total drainage area (McClain and Naiman, 2008). Within the year, the Amazon shows a high degree of seasonality, during which discharge volume varies by a factor of four between the high-discharge (May-June) and low-discharge (November-December) seasons (Smoak et al., 2006).

The Amazon Estuary represents the interface between the Amazon River and the Atlantic Ocean (Figure 5.2). The riverine outflow into the estuary forms a large delta which is split into two primary channels on either side of Marajó Island, with the more northern channel referred to as the Amazon River and the more southern channel the Pará River. Just south of the estuary are the Pará Mangroves, a large mangrove forest which makes up part of the Guianan-Amazon mangrove system, one of the largest in the world. The Amazon Estuary is atypical among estuaries in that it does not exist within a semi-enclosed mixing basin (Pritchard, 1967), but rather as a wide-ranging salinity gradient reaching hundreds of kilometers out onto the Amazon Shelf. The extent of this gradient is dependent on the seasonality of the Amazon discharge and extends much further outward during high-discharge than during low-discharge (Lentz, 1995). Circulation within the estuary has a large impact on the local Atlantic, as it entrains a volume of ocean water 10 times greater than the total Amazon outflow into this estuarine mixing regime (Smoak et al., 2006), where this ocean water then becomes exposed to the complex chemistry which may occur within. Due to the large differences in salinity (and therefore density) between Amazon and Atlantic, water within the estuary is highly stratified. Within the majority of the Amazon Shelf region, a 3-10 m thick low-salinity 'film' known as the Amazon Plume overlies higher-salinity bottom water which extends down to the shelf (Lentz, 1995; Koschinsky et al., 2018). This plume is carried northwards with the North Brazil Current (NBC) and Northeast with the North Equatorial Counter Current (NECC) (Bourles et al., 1999) and its influence can be seen thousands of

Figure 5.1: A view of the entire Amazon catchment basin. Adapted from Calhman and da Hora (2017).

kilometers away in both the Caribbean and equatorial Atlantic (Smoak et al., 2006).

Tides in the Amazon Estuary are very energetic, and can lead to tidal currents reaching velocities of up to 200 cm s^{-1} (Geyer et al., 1996), while the NBC itself can reach velocities of over 90 cm s^{-1} (Johns et al., 1998). This combination leads to a high degree of reworking and resuspension of sediment across much of the Amazon Shelf, but particularly so at lower salinities within the estuary (Kuehl et al., 1986, 1996). Additionally, these tides lead to a continually shifting salinity gradient, which extends outwards into the Atlantic during low-tide and contracts inward during high-tide.

The behavior of dissolved uranium as a whole has been studied within the Amazon Estuary (Moore, 1967; McKee et al., 1987; Swarzenski et al., 1995a; Swarzenski and McKee, 1998; Swarzenski et al., 2004), though there has been only limited measurements of the isotopic ratios (Moore, 1967; Swarzenski et al., 2004) and none have thus far used high-precision MC-ICP-MS. Measurements of the riverine end-member have shown the Amazon to have very low U concentration (0.06 μg l^{-1}) and elevated δ^{234}U (205‰) at a salinity of 0.3 PSU (Swarzenski et al., 2004)). Despite this low concentration, the enormous flow volume of the Amazon means that this would constitute a significant source of oceanic uranium (Chabaux et al., 2003). However, this neglects possible effects on U concentration and δ^{234}U from processes within the estuary. The majority of studies have shown the Amazon Estuary to function as a uranium sink, particularly at salinities below 10-20 PSU, likely as the result of flocculation and aggregation driven by hydrous metal oxides and reactive particles released during sediment resuspension (Swarzenski et al., 1995a; Swarzenski and McKee, 1998; Swarzenski et al., 2004). McKee et al. (1987) showed conservative mixing across the salinity gradient and speculated that the shelf could potentially function

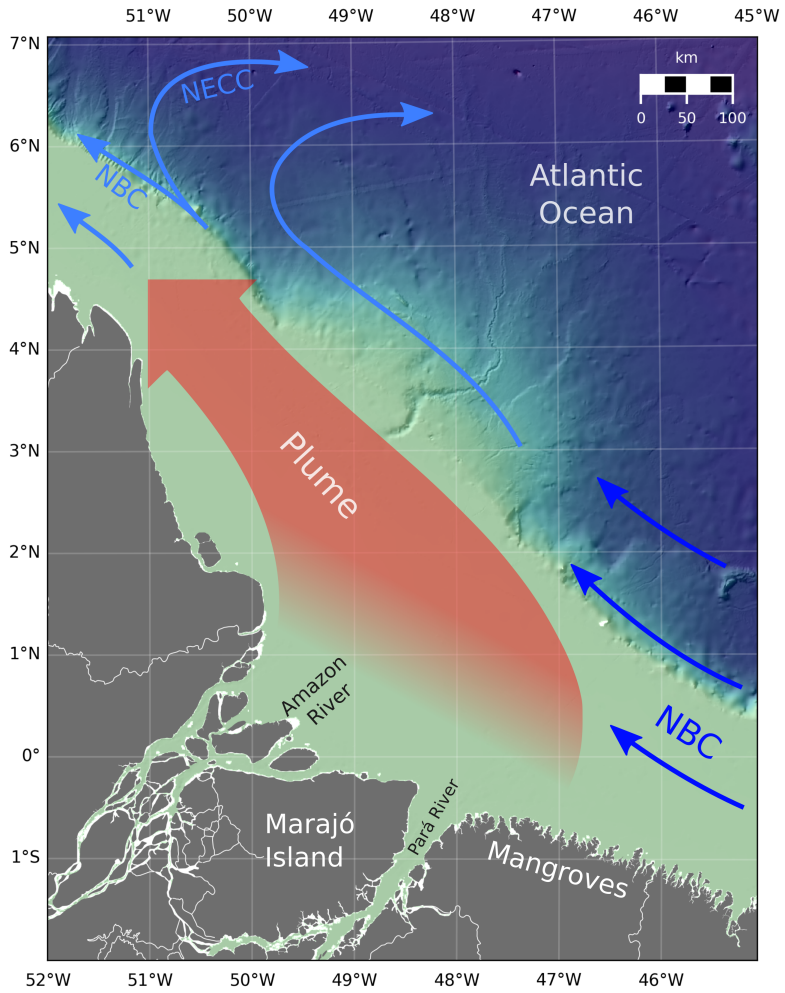

Figure 5.2: The Amazon Estuary region with an approximation of the Amazon Plume in red. The incoming North Brazil Current (NBC) is in dark blue. Lighter blue denotes surface currents heavily influenced by the plume: the northwest continuation of the NBC and the North Equatorial Counter Current (NECC). (Geyer et al., 1996; Johns et al., 1998; Bourles et al., 1999).

as a large source of oceanic U, although the analysis included very few samples from salinities below 10 PSU. The behavior of the uranium sink has been shown to display a high degree of seasonality and become stronger during the low-discharge season, although it remains a sink during high-discharge as well (Swarzenski and McKee, 1998).

This chapter will present the most in-depth investigation into the behavior of dissolved U within the Amazon Estuary to date, as well as the first to provide a comprehensive look into δ^{234}U. It will begin with a description of the samples and sampling process, followed by a presentation of the results. Afterwards, the discussion will turn towards establishing an Amazon end-member to enable further analysis of the estuarine samples. With this in place, geographical differences in U behavior within the estuary at low salinities will be looked into before switching to the dynamics seen at the high-salinity end of the spectrum. Ultimately this will lead to a discussion about the overall impact of the Amazon River on the δ^{234}U of the Atlantic Ocean.

5.2 Sample overview

59 samples from the Amazon Estuary region were analyzed. These were collected during the April-May 2018 M147 Amazon-GEOTRACES cruise (Koschinsky et al., 2018) aboard the RV *Meteor* using the onboard Seabird SBE 9 plus CTD. Samples were collected in 250 ml PP bottles and acidified to a pH of 2 by adding 400 ml 30% HCl to ensure that dissolved U remained in solution. The cruise took place during the Amazon River's high-discharge season.

As seen in Figure 5.3 samples were taken throughout the Amazon Estuary and surrounding region, providing the most comprehensive view of Amazon δ^{234}U dynamics to date. Samples were taken from across numerous salinity 'transects' to investigate U dynamics at various stages of mixing between Amazon (freshwater, 0 PSU) and Atlantic (∼34-36 PSU in this region) water. Among the samples, 40 were taken from as close to the surface as was possible given the magnitude of the waves at the time of sampling, with typical depths of 2-5 m. The remaining 19 are from depths of 6-806 m. These two groupings may be seen on the left-hand side of Figure 5.3. The shallower group represents primarily samples from within the Amazon Plume, while the deeper samples are from the higher-salinity water below. It should be remembered that the salinity gradient in the estuary is not static, but is instead heavily dependent upon the tidal cycle. During low-tide salinity lows reach further towards the ocean, while during high-tide high-salinity ocean water encroaches further towards the Amazon River mouth. While in broad terms the geographic location of the samples remains important, the most critical factor for directly comparing samples is the salinity, which is largely representative of the exact Amazon-Atlantic water mixing composition. The overall salinity range of the samples is from 0.03 PSU to 36.23 PSU.

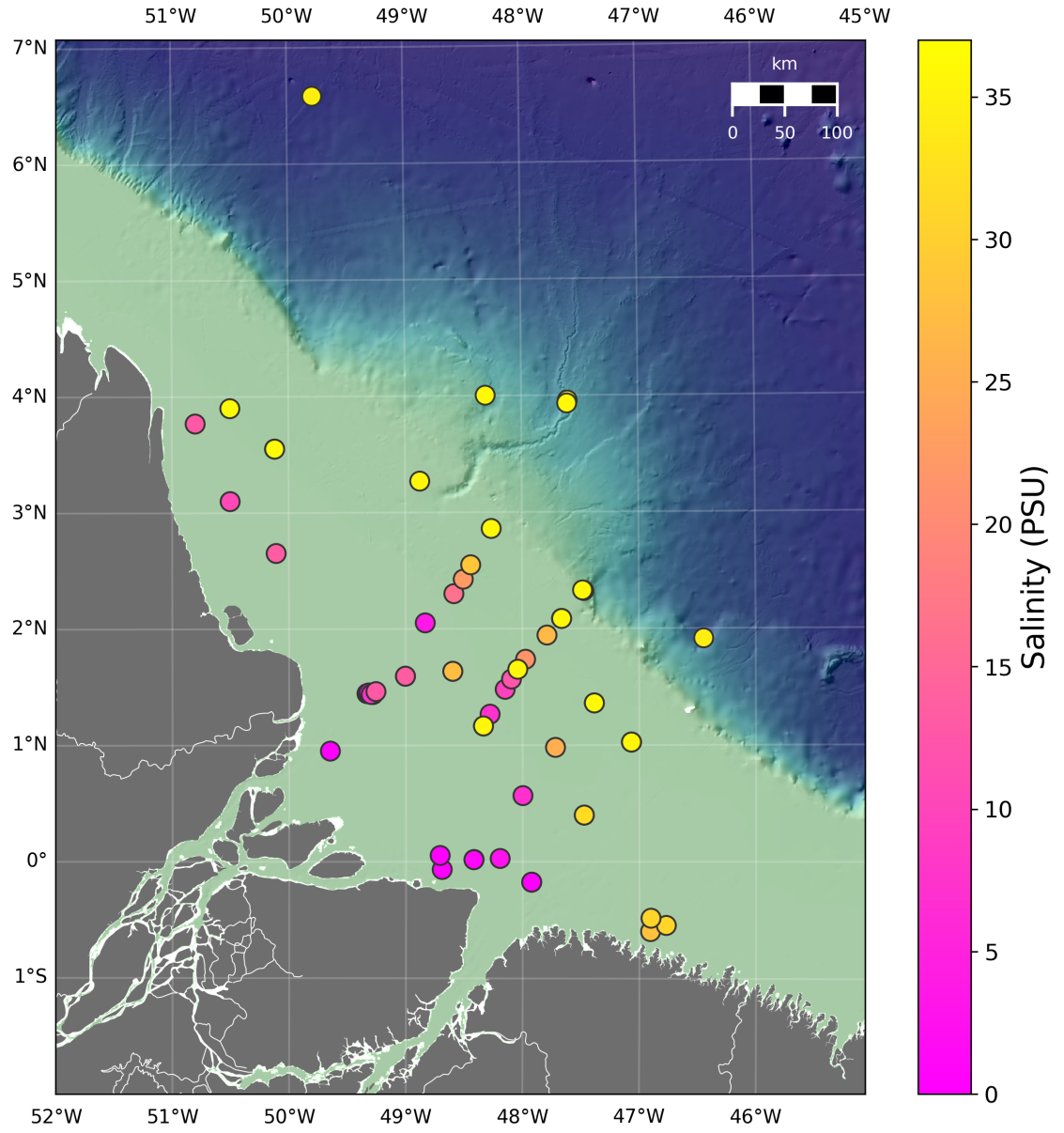

Figure 5.3: Locations of samples taken from the Amazon Estuary, colored according to salinity. The left-hand subplots show samples taken from shallower than 5 m depth (top) and those from over 5 m depth (bot).

5.3 Results

Results for U concentration and δ^{234}U are shown in Figure 5.4. Overall δ^{234}U ranged from 145.7-247.6‰, with U concentrations between 0.04-3.26 μg l^{-1}. A strong correlation exists between salinity, U concentration, and δ^{234}U. Low salinity samples have lower concentration and higher δ^{234}U, while high salinity samples have high concentrations and low δ^{234}U. δ^{234}U uncertainties are highly dependent upon U concentration. Samples with U concentrations above 1.5 μg l^{-1} have uncertainties typical of oceanic samples on the order of 0.3‰. This rises to ∼1‰ for samples between 0.5 and 1.5 μg l^{-1}. At the very low end of the concentration spectrum, coinciding with the highest δ^{234}U values, uncertainties are on the scale of 10‰ (max: 13.2‰). Analytical uncertainties for U concentration were negligible.

Samples show significant spread in both δ^{234}U and ^{238}U at low salinities (<15 PSU). If conservative 2-end-member (Atlantic and Amazon) mixing of water masses were to be taking place, smooth curves with little to no scatter would be expected. This will be discussed further in Section 5.4.2.

5.4 Discussion

This section will look into the results presented in Section 5.3. This will begin with the establishment of a mixing end-member for the Amazon River and Atlantic Ocean, followed by a look at the geographical differences seen in the Amazon Estuary, with emphasis on the low salinity regime. Finally, focus will shift to the high-salinity end of the spectrum and the apparent impact of the Amazon Estuary on Atlantic δ^{234}U.

5.4.1 Establishing the Amazon River and Atlantic Ocean U mixing end-members

To analyze the mixing which is seen in the Amazon Estuary, it is necessary to define the end-members of the mixing components. The Atlantic end-member has been discussed previously in Chapter 4 and is defined according to literature. U concentration varies conservatively with salinity according to the relationship ^{238}U (μg l^{-1})=(0.0919±0.0005)∗salinity (Chen et al., 1986), while oceanic δ^{234}U = 146.8± 0.1‰ (Andersen et al., 2010). Surface ocean salinity in this region can vary from ∼35-37 PSU due to strong evaporation and precipitation, so there is no singular Atlantic salinity end-member from which the U concentration can be determined. However, this is not of great concern for the purpose of this analysis, as salinity and U concentration both behave conservatively. Of primary importance is that the Atlantic end-member has a salinity (and corresponding ^{238}U) which is higher than all of the samples from this dataset, so that they may all be analyzed in terms of being the product of two-member mixing. As the highest salinity seen in the Amazon Estuary samples is 36.23 PSU, this was rounded up to the nearest quarter-PSU unit

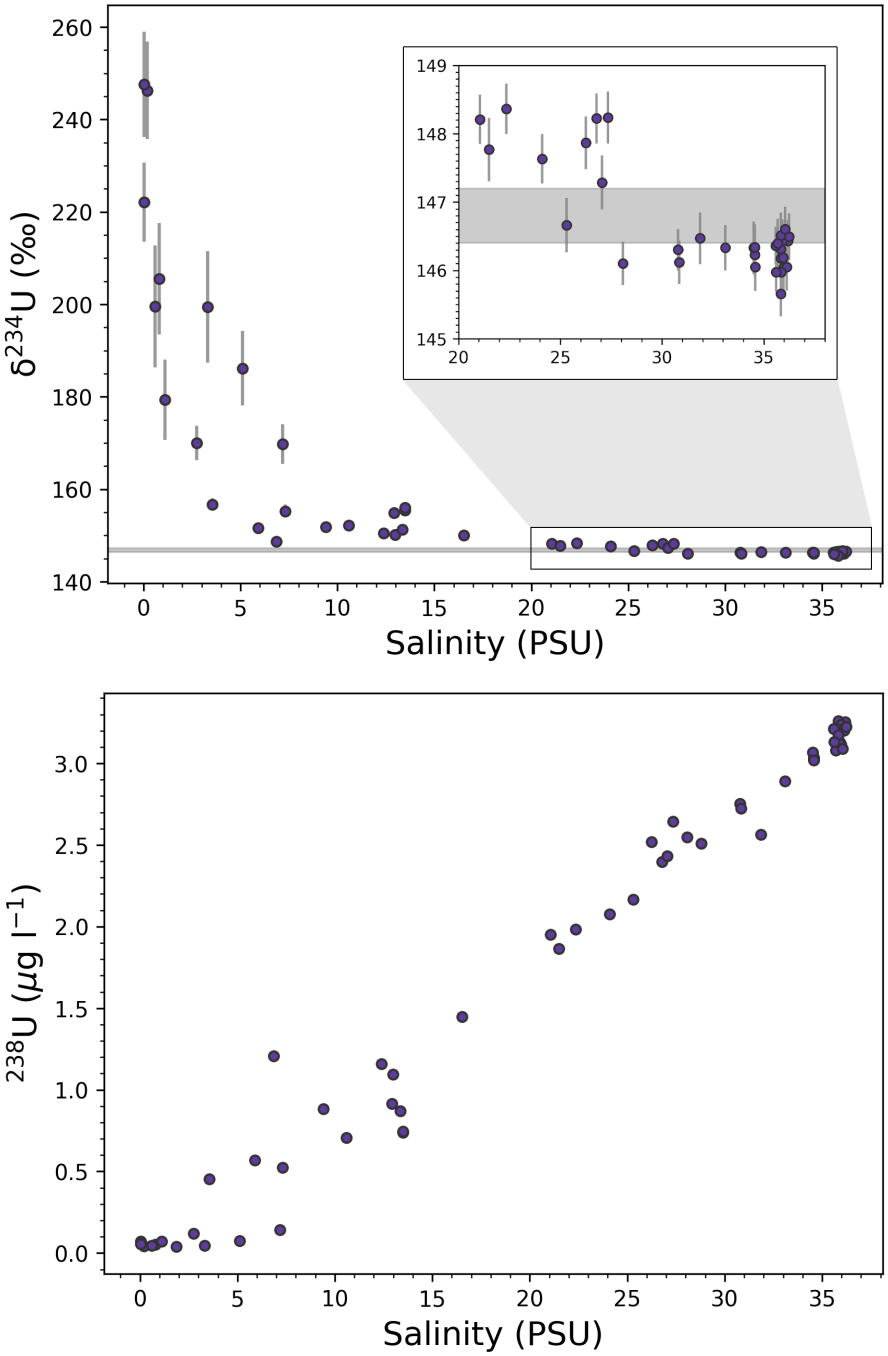

Figure 5.4: (Top) δ^{234}U results from all Amazon Estuary samples. The inset figure shows a zoomed in view of high salinity samples. The shaded horizontal section represents the oceanic δ^{234}U from Andersen et al. (2010) of 146.8 ± 0.1‰. All errors are 2σ, although most are smaller than the plot symbols. (Bottom) Salinity vs. U concentration (^{238}U) for Amazon Estuary samples.

resulting in a chosen Atlantic end-member with a salinity of 36.25 PSU and ^{238}U of 3.33 μg l^{-1}.

The Amazon River end-member will be defined by the single lowest salinity sample among the dataset (0.03 PSU), with corresponding ^{238}U and δ^{234}U of 0.05 μg l^{-1} and 247.6‰ respectively. In addition to being the lowest salinity, this sample also represents the highest δ^{234}U among the data. Four other samples, with salinities ranging from 0.60-3.32 PSU, have U concentrations which are slightly lower than the chosen end-member, which is likely to be indicative of low-salinity non-conservative U behavior as has been recorded in previous studies (Swarzenski et al., 1995a; Swarzenski and McKee, 1998; Swarzenski et al., 2004). The end-member sample is similar to the one which was found by Swarzenski et al. (2004) with ^{238}U = 0.06 μg l^{-1} and δ^{234}U = 205‰, although the previous end-member has a slightly higher salinity of 0.3 PSU, compared to the 0.03 PSU here.

5.4.2 Geographical differences in U behavior within the Amazon Estuary

When analyzing the behavior of U within the Amazon Estuary, it is important to keep in mind that an estuary, like any turbulent system, is not a uniform entity. Differences in properties such as flow velocity, particle load, or local geography can strongly vary within a single estuarine system, which may lead to the existence of various and differing biogeochemical environments within the estuary. The scatter seen at low salinities (<20 PSU) in Figure 5.4 may possibly be explained by the dissolved uranium behaving differently in different areas. To look into this, Figure 5.5 shows the ^{238}U (left) and δ^{234}U (right) results at their sampling locations. These are split into two generalized groupings: samples from the northwest of the estuary (NW, 27 samples) and samples from the southeast (SE, 32 samples). This provides two easily comparable groups, which both contain roughly equal numbers of samples, and which both span the entire spectrum of mixing between Amazon and Atlantic.

When considering the groupings in Figure 5.5, it is not clear from merely looking at the ^{238}U and δ^{234}U values if there is any difference between NW and SE. Both areas display a relatively smooth transition between the low-U, high-δ^{234}U Amazon and the high-U, low-δ^{234}U Atlantic. Both also have a number of perceived outliers that don't appear to follow this trend. Ultimately however, this representation is missing any information about the constituent makeup of each sample in terms of proportion of Amazon- and Atlantic-sourced water, which makes direct comparison impossible. A comparison of two U concentrations or δ^{234}U values is meaningless if it does not consider the properties which each sample would be 'expected' to have. This can be achieved through instead analyzing each sample with regards to how it relates to ideal, conservative mixing at its associated salinity. This will take place in two parts, first looking at U concentrations before transitioning to δ^{234}U.

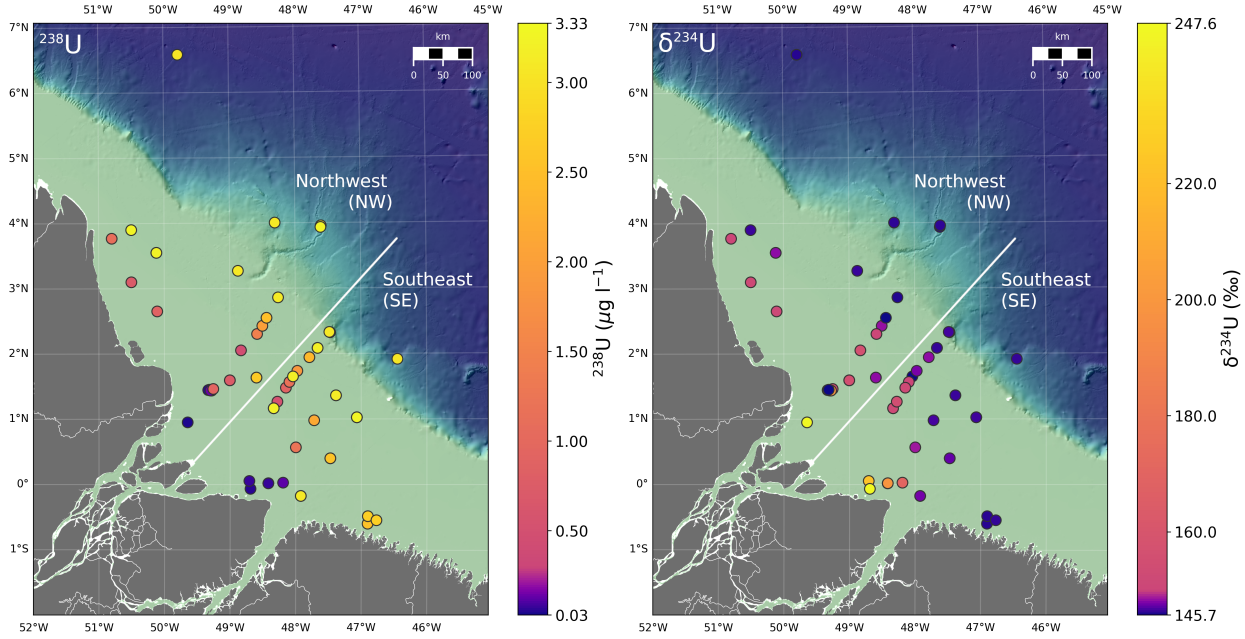

Figure 5.5: Amazon results shown geographically. (left) U concentration, (right) δ^{234}U. The white lines show the boundary between samples from the northwest (NW) or southeast (SE) of the Amazon Estuary, a designation which will be used to look into regional differences in U behavior.

U concentrations

Focusing first on U concentration, the top plot in Figure 5.6 shows the ^{238}U from NW and SE samples as well as the Amazon-Atlantic conservative mixing line. In this, it is clear that there are significant differences between U behavior in the NW and SE, particularly at salinities below 15 PSU. Within this regime, NW samples tend to lie further from the conservative mixing line than similarly saline SE samples, indicative of a stronger 'U-sink' effect in the NW than the SE. Additionally, the NW behaves as a U-sink on a broader range of salinities (up to ∼14 PSU), while the SE only shows U-sink behavior below ∼3 PSU and largely conservative mixing above ∼ 6 PSU. Previous studies on U dynamics in the the Amazon Estuary have focused almost exclusively on the NW region and have shown behavior similar to that which has been observed here. Swarzenski et al. (1995a), Swarzenski and McKee (1998), and Swarzenski et al. (2004) all found strong U-sink behavior up to salinities of 16-20 PSU. It therefore appears that the U-sink in the NW has been functioning similarly for at least the last 3 decades. There is, as of the time of writing, no known external study which comprehensively covers U-dynamics in the SE portion of the Amazon Estuary, as none of the previously listed works contain more than a handful of samples from the region, particularly at low salinity.

To better compare the extent of U-removal between samples at different salinities and enable meaningful comparisons between sampling locations, the samples will

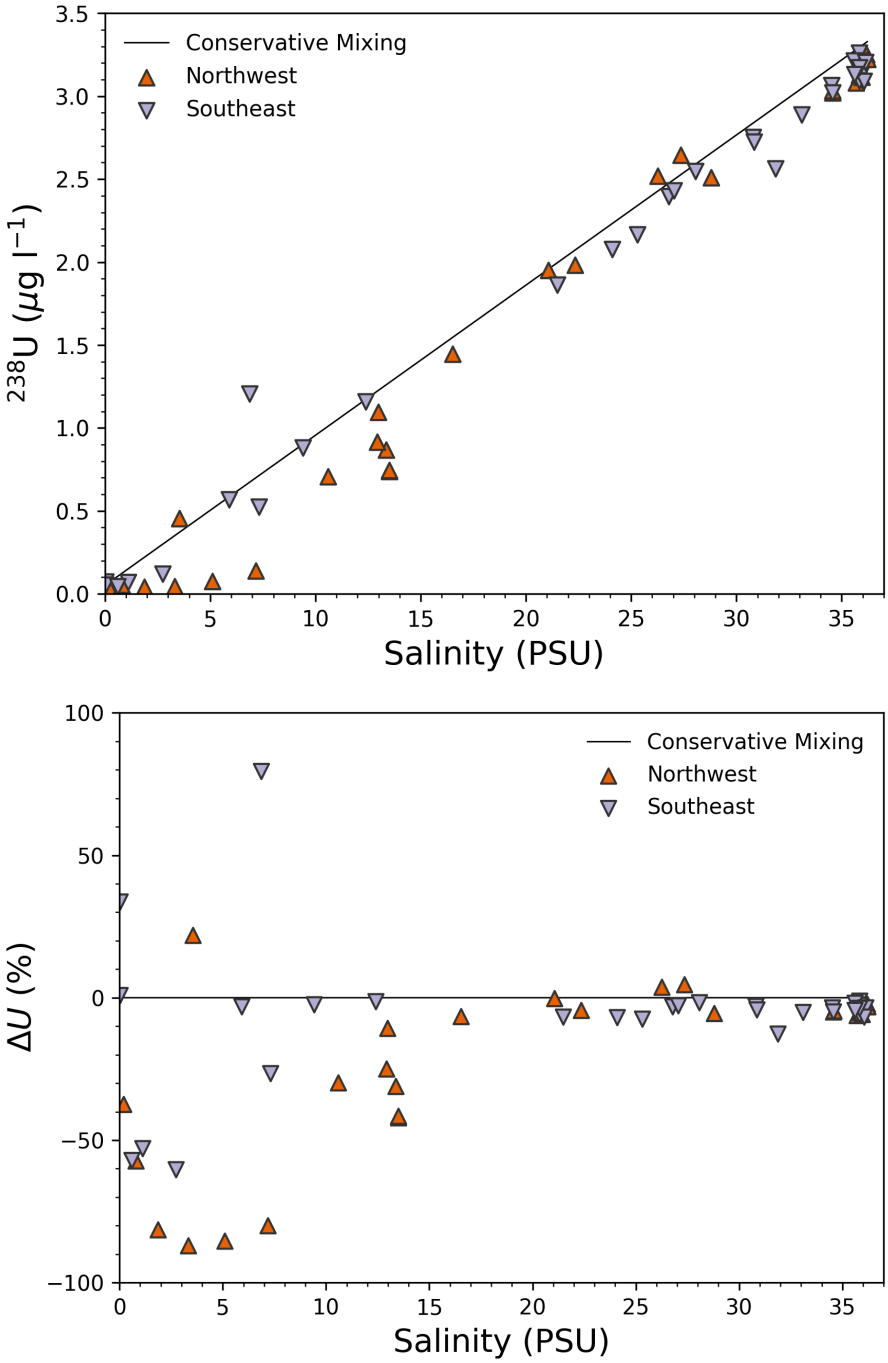

Figure 5.6: (Top) ^{238}U results from Amazon Estuary samples colored according to whether they came from the NW or SE sections. The black line represents hypothetical conservative mixing across the salinity gradient between Amazon and Atlantic end-members from Section 5.4.1. (Bottom) The U content of each sample relative to conservative mixing (ΔU), i.e. -100% represents all U being removed, while +100% represents double the expected U.

now be formulated in terms of the percentage offset of ^{238}U relative to conservative mixing (which will hereafter be referred to as ΔU). This is achieved through the relationship:

$$\Delta U = \frac{U_{sample} - (U_{Amazon} f_{Amazon} + U_{Atlantic} f_{Atlantic})}{U_{Amazon} f_{Amazon} + U_{Atlantic} f_{Atlantic}} \times 100\,(\%) \tag{5.1}$$

where U_x represents U concentration (^{238}U). $f_{Atlantic}$ and f_{Amazon} represent the fraction of water within each sample which comes from the Atlantic or Amazon end-member based upon their salinities (i.e. $f_{Atlantic} = 1$ means a sample is completely Atlantic water). These are defined as:

$$f_{Atlantic} = \frac{S_{Atlantic} - S_{sample}}{S_{Atlantic} - S_{Amazon}} \tag{5.2}$$

and

$$f_{Amazon} = 1 - f_{Atlantic} \tag{5.3}$$

with the S_x values equal to the associated salinity. A negative ΔU therefore represents U concentrations which are lower than those which would be found with conservative mixing, down to a minimum of -100% (representing a sample completely free from U). Conversely, positive values mean that the sample has more U than would be expected through conservative mixing, with 100% representing a doubling of U compared to conservative mixing.

The bottom plot in Fig 5.6 shows the ΔU for all samples from NW and SE as well as the conservative mixing line (which in this case is by definition always $\Delta U = 0\%$). This highlights the true extent of U removal at low salinities within the Amazon Estuary, as well as how differently this removal occurs in the NW and SE. U removal peaks in the NW at salinities of ∼2-8 PSU where ΔU reaches between -80% and -90%, indicating that nearly all U has been removed from the water. For the SE this minimum occurs between ∼0.5-3 PSU with ΔU values of reaching between -50% and -60%. This confirms that, overall, the NW behaves both as a much stronger U-sink than the SE, as well as over a larger range of salinities. At higher salinities (>16 PSU in the NW, >6-9 PSU in SE) both areas behave much more conservatively, appearing to closely following ideal dilution.

The ΔU formulation provides a much more meaningful comparison between samples when viewed geographically than the raw ^{238}U because it takes into account differences in salinities between samples, which is an important factor due to the shifting nature of the estuarine salinity gradient. Figure 5.7 shows the ΔU for each sample, revealing the locations of the U-sinks in both NW and SE (circled in blue). The NW sink is geographically much larger and extends from the Amazon River mouth northwestward following the Amazon Plume. The SE sink is confined to a comparatively small area, which is surrounded by non-sink conditions. The three samples with significantly positive ΔU (stars, $\Delta U > +10\%$) are all located directly adjacent to the sinks. As these likely represent localized sources of U release, their

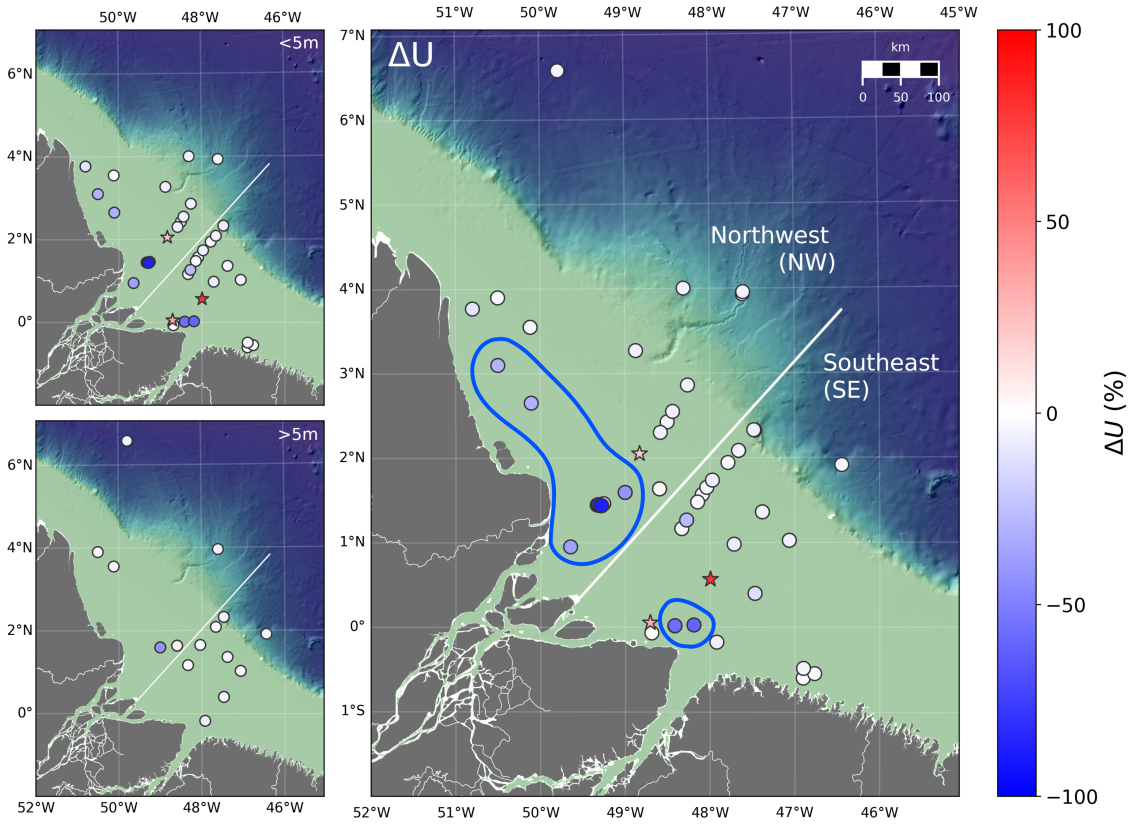

Figure 5.7: Geographical view of ΔU results. The main map (right) shows all samples, while left-hand maps only show samples from surface (<5m, top) or bottom (>5m bottom). Samples are split between NW and SE as in Figure 5.5. Circled areas designate the regions with strong U-sink behavior. Stars are samples with $\Delta U > +10\%$, indicating local U-sources.

being located near the sinks is indicative of variability in the position or extent of the U-sinks over time. When a sink removes U from the water column, this U is generally transferred to the sediment, where it builds up over time. If local biogeochemical conditions change at some point from those favoring U-removal to those allowing U-release, some of this stored U may then be released back into the water column (McKee et al., 1987; Barnes and Cochran, 1993). Accordingly, it is likely that in the past the U-sinks extended into the areas now marked as sources, leading to a build up of excess U at these locations, and that either shrinking or relocation of the U-sinks has allowed for the release of much of this accumulated U. As these samples were all collected during the high-discharge season in the Amazon, this may be a consequence of seasonality. Swarzenski and McKee (1998) analyzed the U content of water samples collected from the Amazon Estuary during three times of the year corresponding with low-, rising-, and high-discharge. It was found that the U-sink was strongest during low-discharge, while rising- and high-discharge corresponded with a slightly weaker U-sink. It may therefore be the case that during the low-discharge season the U-sinks expand to include the areas which were found here to be acting as U-sources and then contract during times of high-discharge, allowing the re-release of some of this U. There are possible issues with this theory however, due to the way in which sampling was carried out in the aforementioned study. In it, samples were collected strictly based on salinity from a broad sampling area which lies approximately 2/3 in the NW and 1/3 in the SE. As no individual sampling locations are listed, it may simply be the case that the observed U-sink seasonality is actually the result of the in-homogeneous geographical behavior of U within the estuary. It is therefore impossible to conclude with any certainty whether the U-sources adjacent to U-sinks observed in this study are the result of seasonal or long-term changes without further investigation of similarly-located samples from the low-discharge season.

δ^{234}U

Having now looked at the U concentrations, the top plot in Figure 5.8 shows the associated δ^{234}U values, as well as curve representing ideal conservative mixing between the Amazon and Atlantic. At first glance this appears to behave similarly to the U concentration data, with significant deviations from conservative mixing at low salinities, particularly among samples from the NW. The SE samples appear to be comparatively closer to conservative mixing. As was also the case for U concentrations, it is difficult to compare the magnitude of δ^{234}U deviations from conservative mixing across the salinity gradient when looking at the raw results, as the conservative mixing function is highly non-linear (in this case behaving as $1/x$). Therefore, as an analogue to ΔU when discussing U concentration, the comparatively simple formulation of '$\Delta\delta^{234}$U' will be used to discuss δ^{234}U. $\Delta\delta^{234}$U is defined as

$$\Delta\delta^{234}U = \delta^{234}U_{sample} - \delta^{234}U_{conservative\ mixing}. \tag{5.4}$$

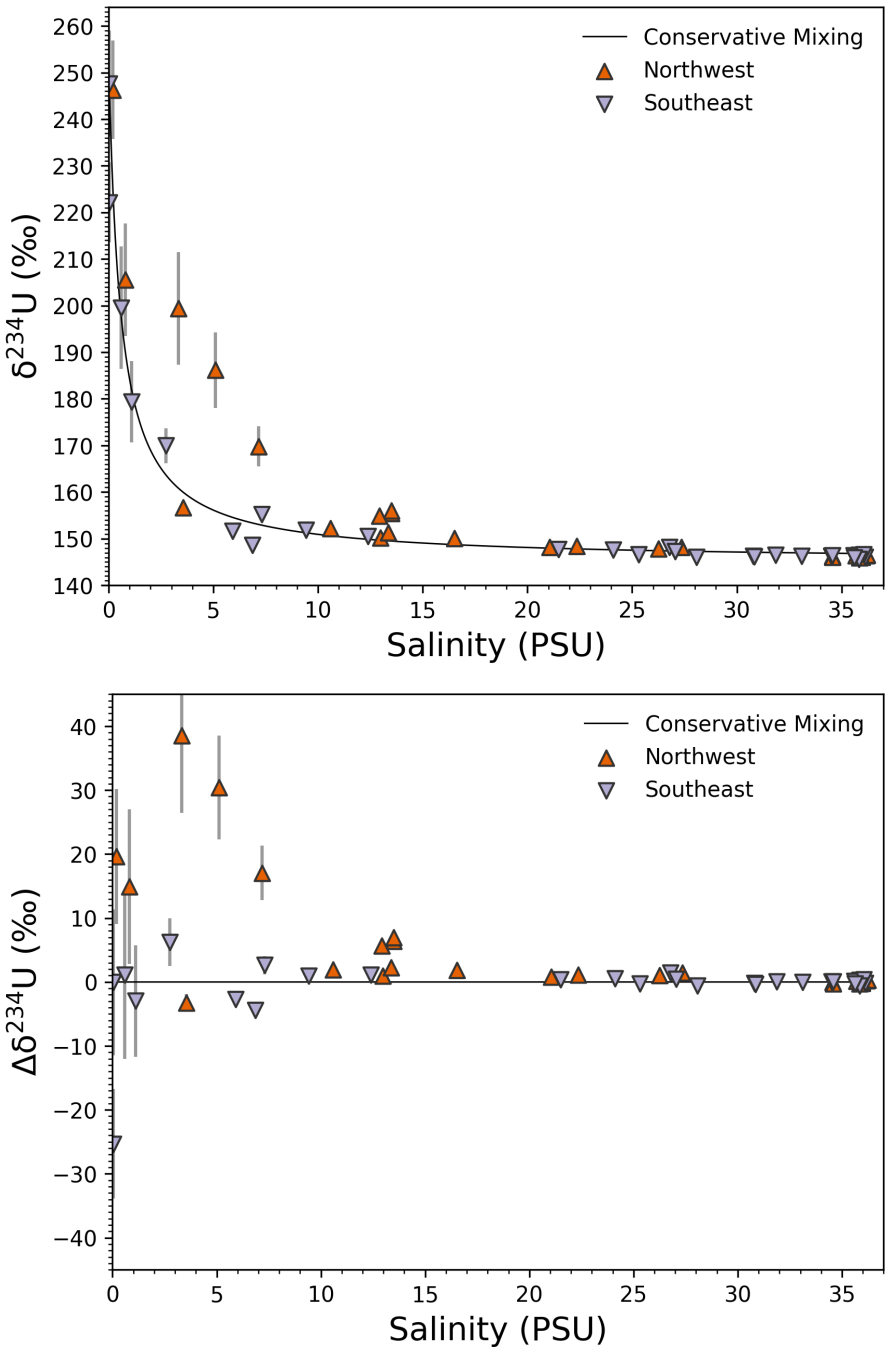

Figure 5.8: (Top) δ^{234}U results from Amazon Estuary samples colored according to whether they came from the NW or SE sections. The black curve represents hypothetical conservative mixing across the salinity gradient between Amazon and Atlantic end-members established in Section 5.4.1. (Bottom) The offset in δ^{234}U between each sample and the conservative mixing curve.

or simply the difference (in ‰) between the δ^{234}U of a given sample and the expected δ^{234}U from conservative mixing at the associated salinity. Therefore, positive $\Delta\delta^{234}$U indicates higher than expected δ^{234}U values and negative $\Delta\delta^{234}$U represents lower than expected δ^{234}U. The bottom plot in Figure 5.8 shows the $\Delta\delta^{234}$U-formulated results. NW samples show high degrees of δ^{234}U enrichment at salinities below ~16 PSU, maxing out at a $\Delta\delta^{234}$U of just under 40‰. SE samples are again comparatively conservative. With the exception of one outlier at ~0 PSU, all of the SE samples are within 6 permil of conservative mixing. At higher salinities both NW and SE converge to more closely follow the ideal mixing scenario.

The behavior of $\Delta\delta^{234}$U appears to closely mirror that of ΔU (Figure 5.6), albeit with inverted sign, as low salinities show enrichment in NW δ^{234}U rather than a reduction. This implies that in areas where U is being actively removed from the water column (i.e. negative ΔU), the δ^{234}U is simultaneously becoming elevated (i.e. positive $\Delta\delta^{234}$U). Such a correlation is confirmed when plotting the two values ($\Delta\delta^{234}$U and ΔU) against one another (Figure 5.9). Here, samples with negative ΔU also overwhelmingly show high $\Delta\delta^{234}$U values, while the three samples with highly positive ΔU (identified previously as localized U-sources) all have negative $\Delta\delta^{234}$U. This appears to be a robust trend across the Amazon Estuary, although geographical differences remain as NW samples in the upper left quadrant appear to have notably higher $\Delta\delta^{234}$U than their counterparts from the SE at similar ΔU. Given the strength of this ΔU-$\Delta\delta^{234}$U relationship, it is no surprise that the geographical distribution of $\Delta\delta^{234}$U also matches well with that of ΔU (Figure 5.7). Figure 5.10 shows $\Delta\delta^{234}$U samples with the previously identified U-sinks (blue enclosed areas) and U-sources (stars) from Figure 5.7. As expected, the high-$\Delta\delta^{234}$U samples are well within the U-sink areas, with the highest values being found in the center of the NW sink.

Explaining this observed relationship between loss of overall U concentration and δ^{234}U enrichment is not trivial. This cannot be solely attributed to α-recoil fractionation (responsible for the elevated ^{234}U content in most aqueous systems), as that is an inherently additive process and not connected to the removal of U from the water column (i.e. α-recoil fractionation always involves introducing new uranium to a system, rather than removing it). In many isotopic systems this combination of reduction in concentration and changes in isotopic makeup would be indicative of isotopic fractionation attached to the removal process itself, where heavier or lighter isotopes are preferentially removed, leading to a reciprocal alteration of the remaining isotopic makeup as well. Uranium however represents one of the heaviest naturally occurring elements, and as such the relative difference in mass between its isotopes is small (<2% for ^{234}U and ^{238}U), limiting the possibility for significant mass-dependent isotope fractionation to take place. Previous studies of non-redox U exchange have shown limited to no alteration in isotopic makeup even at high levels of U-removal (Brennecka et al., 2011; Shiel et al., 2013; Andersen et al., 2017). In anoxic or suboxic environments, additional U-isotope fractionation can take place due to nuclear field shift effects during reduction from U(VI) to U(IV) (Nomura et al., 1996; Bigeleisen, 1996). This is unlikely to have played a role however, as no

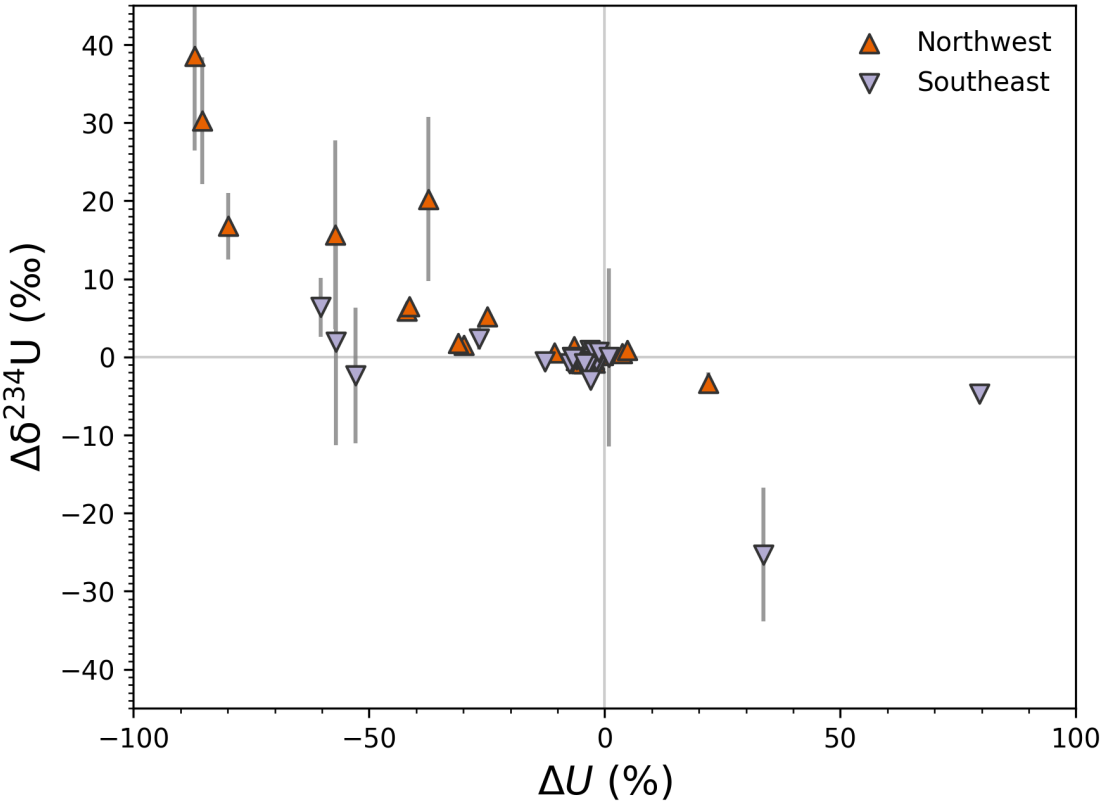

Figure 5.9: Comparison between ΔU and δ^{234}U offset (as seen in Figures 5.6 and 5.8 respectively). Samples with negative ΔU tend to show elevated δ^{234}U, while positive ΔU corresponds with lowered δ^{234}U.

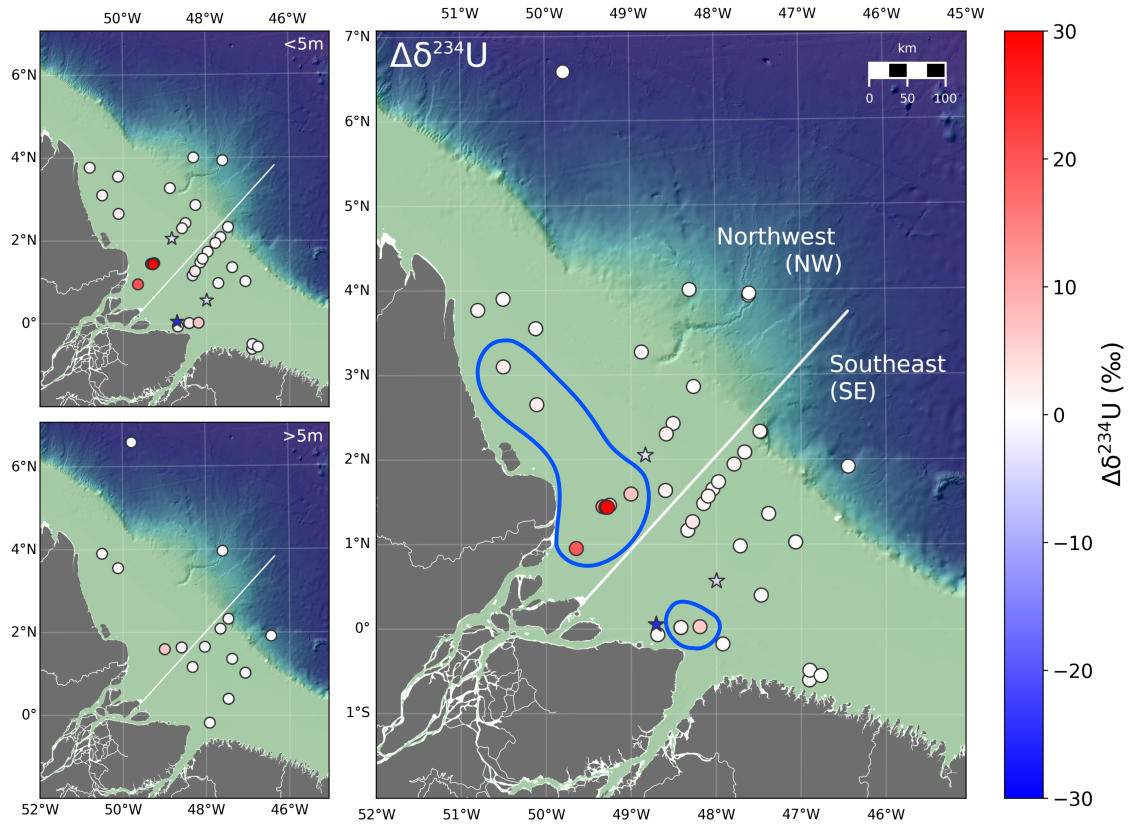

Figure 5.10: Geographical view of $\Delta\delta^{234}$U (as defined by Equation 5.4) relative to conservative mixing between Amazon and Atlantic. Main map shows all samples, while left-hand maps only show samples from surface (<5m, top) or bottom (>5m bottom). Samples are split between NW and SE as in Figure 5.5. Circled areas designate the regions with strong U-sink behavior, as defined in Figure 5.7. Stars are samples with $\Delta U > 10\%$, indicating local U-sources.

evidence of low-oxygen conditions were found during sampling by the CTD-mounted oxygen sensor. Oxygen levels showed an overall minimum value of 121 μmol l^{-1}, which is well above the standard threshold used to define suboxic conditions of 10 μmol l^{-1}.

The U-behaviors seen in the Amazon Estuary are likely due to a combination of factors. Previous studies of U in the estuary have suggested that the U-sink seen at low salinities is due to U being preferentially absorbed onto oxides, flocs, and re-suspended sediments, which were then themselves removed from the water-column by colloidal aggregation, flocculation, and particle settling (Sholkovitz, 1993; Swarzenski et al., 1995b, 2004). In groundwater, it has been shown that areas of U removal can often be associated with high-δ^{234}U in the remaining dissolved uranium, as the build-up of precipitated U enhances the relative strength of the α-recoil effect (Porcelli and Swarzenski, 2003). Additionally, as U concentration in water is lowered,

less input of high-δ^{234}U uranium is required to change the overall δ^{234}U, while the reservoir from which these α-recoil effects can take place grows ever larger. Following this, one possible scenario which would explain the observed behavior of U in the Amazon Estuary U-sink regions would be as follows:

1. U attaches to particles and becomes stored in the sediments
2. α-recoil leads to a raising of the δ^{234}U in the pore-waters within these sediments
3. Resuspension of sediment releases some of this high-δ^{234}U, while continuing to contribute towards the overall removal of U from the ambient water.

While this fits with the U behavior seen in the U-sink areas, this does not explain the existence of three high-^{238}U, low-δ^{234}U U-sources (stars in Figures 5.7 and 5.10). As previously mentioned as part of the ΔU discussion, these apparent sources lie near the boundaries of the U-sinks and likely represent the re-release of previously accumulated U in an environment which no longer promotes U-removal. As these sources all show a negative $\Delta\delta^{234}$U, the released U must have a δ^{234}U value lower than the δ^{234}U expected due to conservative mixing at their associated salinity. A possible explanation for this behavior may be the seasonal nature of the salinity gradient within the Amazon Estuary. These samples were collected during the high-flow season, when the increased flow of water from the river pushes the salinity gradient outwards towards the Atlantic, however this contracts significantly during the low-flow season. Mascarenhas et al. (2016) found that the perpendicular extent of the Amazon Plume into the Atlantic to vary from 200 km to 30 km during the high- and low-discharge seasons, respectively. The salinity at the location of each of the sources is therefore likely to be higher during other portions of the year, when the salinity gradient contracts towards the Amazon River mouth. If these locations were to swap to U-sink conditions rather than those of U-release, this would lead to a build-up of relatively high-^{238}U, low-δ^{234}U uranium (i.e. more 'ocean-like' uranium) due a higher proportion of Atlantic water being present than in the high-flow season. When the high-flow season returns and the estuary extends outward, a portion of this accumulated U could then be re-released. While this is a possible explanation, further analysis of the low-flow season in the Amazon Estuary showing U-sink behavior at these locations would be necessary to show that these sources are indeed the result of a seasonal cycle.

Throughout this section, it has been shown that the behavior of U in the Amazon Estuary differs significantly, not just along the salinity gradient, but also geographically. The NW portion of the estuary contains a large U-sink, present until a salinity of 16 PSU, which at its maximum removes ~90% of U from the water column. By comparison, mixing in the SE is largely conservative, with only a weak U-sink present at salinities below 6-9 PSU. Particularly the large NW sink is associated with strongly elevated δ^{234}U of up to ~40‰ above that which would be expected by conservative mixing between the Amazon and Atlantic. This may be the result of high-δ^{234}U pore-waters being released due to sediment re-suspension simultaneous

to the overall removal of U from the water column. Additionally, three localized U-sources were identified, where U concentrations were significantly above those which would be expected due to conservative mixing. As each of these also has a lower δ^{234}U than expected and the samples were collected during the Amazon's high-flow season, it was proposed that these sources represent the re-release of U accumulated outside of the high-flow season from higher salinity (i.e. more Atlantic-influenced) water.

5.4.3 High salinity U-behavior and evidence of mangrove influence

Having looked at the low-salinity regime, it is clear that there are significant differences, both geographically and across the salinity gradient, in the behavior of U within the Amazon Estuary. By comparison, at higher salinities (>20 PSU), U appears to behave much more conservatively. Looking at Figures 5.6 and 5.8, it is clear that values tend towards the conservative mixing line at higher salinities, in both the 'raw' ^{238}U and δ^{234}U as well as the 'reformulated' ΔU and $\Delta\delta^{234}$U. This does not mean that there are no interesting dynamics taking place, but rather that they must be investigated at a different scale. This end of the salinity gradient approaches the oceanic regime, where U is generally seen as homogeneous, and δ^{234}U differences on the scale of 1‰ or a 10% change in U concentration would be considered highly unusual. As the U concentrations in the Atlantic are two orders of magnitude larger than the Amazon, such seemingly small changes at high-salinities can actually represent significant bulk additions/removals of U from the water column, even if the overall impact on U concentration or δ^{234}U is diluted.

Figure 5.11 shows the results from the high-salinity samples in terms of ΔU (top) and $\Delta\delta^{234}$U (bottom), colored by depth. This demonstrates how the samples can be broadly split into two initial categories, those from within the Amazon Estuary (salinity 20-34 PSU) and those which can be considered oceanic (salinity >34 PSU). The oceanic samples can be further split into two sub-groupings based on the depths from which the samples were collected. The majority of Atlantic samples were collected from depths of less than 70 m, well within the mixed-layer of the NBC, which extends to a depth of approximately 100 m in this region. The remaining four samples are from depths of 750-810 m, representing the very lowest reaches of the NBC, just above the transition to the Deep Western Boundary Current (DWBC). The mixed-layer samples can be seen to cluster at a salinity of ∼36 PSU, while the deep samples all have a salinity of 34.5 PSU. What is important to emphasize about these two groups of oceanic samples is that, in the context of assessing the impact of the Amazon on the uranium content of the Atlantic, they represent two important and opposite frames of reference. Due to the highly stratified nature of Amazon outflow, any mixing with Atlantic water will take place primarily at the surface and thereafter propagated throughout the local mixed-layer. Therefore, mixed-layer samples are more likely to show signs of influence from Amazon mixing than the

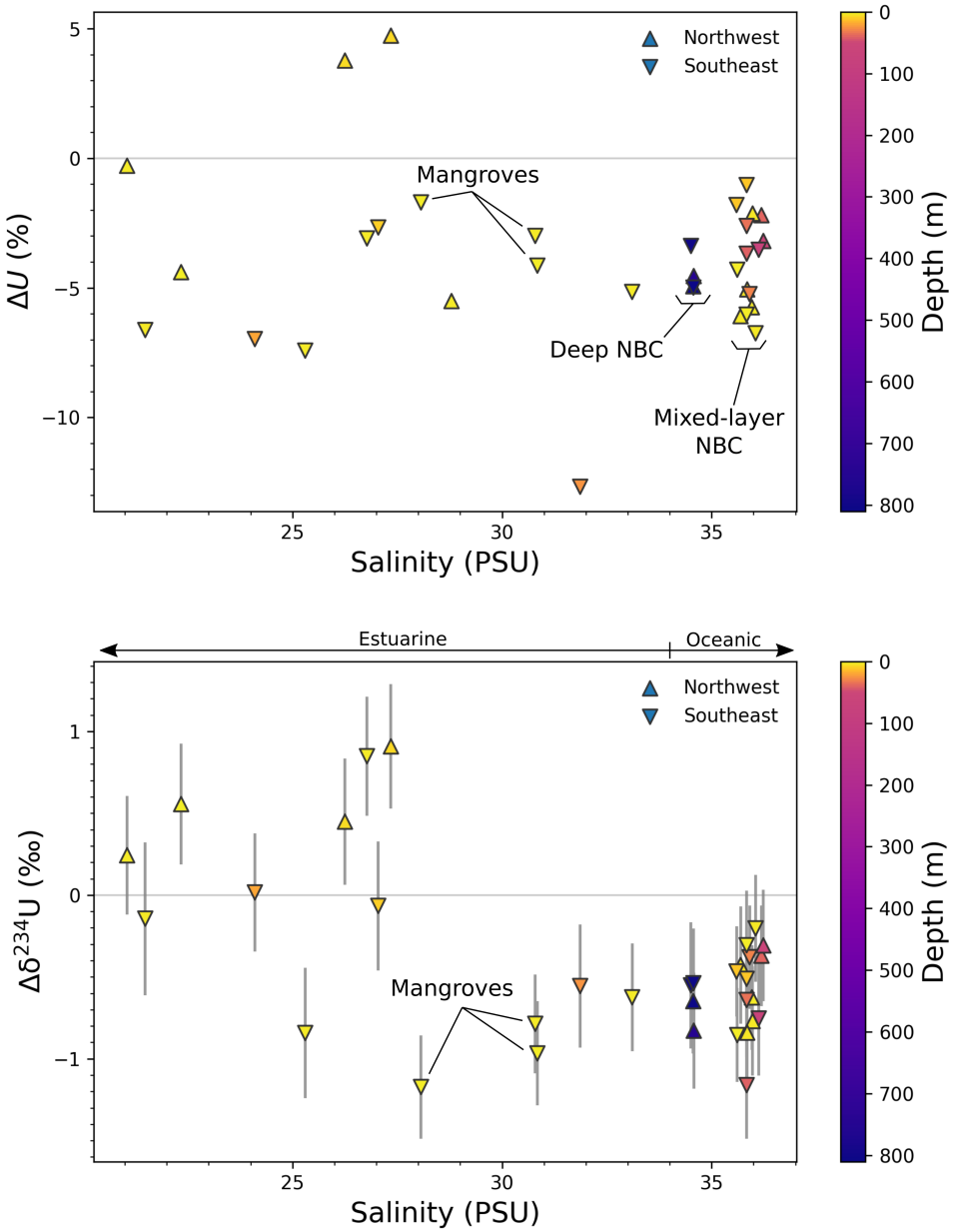

Figure 5.11: The ΔU (top) and $\Delta\delta^{234}$U (bottom) results from the high-salinity (>20 PSU) samples. Samples are split between NW and SE as in Figure 5.5. NBC stands for North Brazil Current.

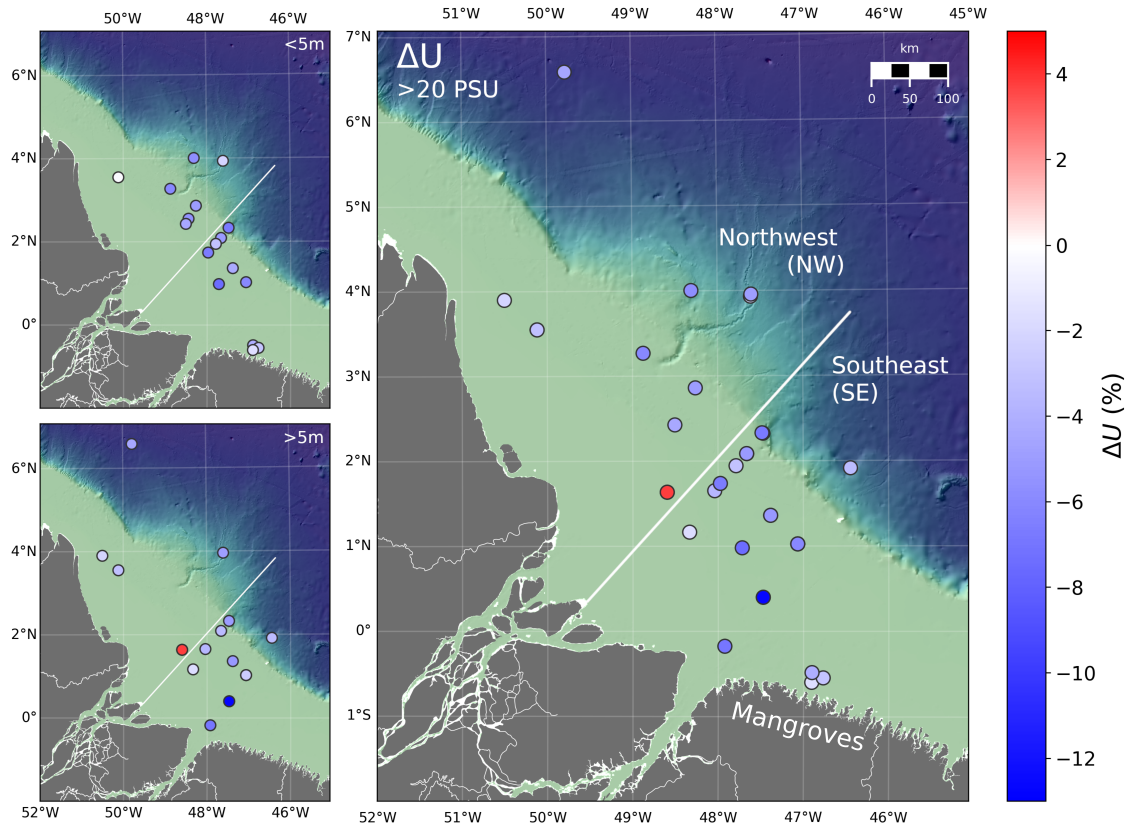

Figure 5.12: A map of the high-salinity (>20 PSU) ΔU results. The location of the Pará Mangroves are labeled. The three samples located just off the coast near the mangroves are labeled as "Mangroves" in Figure 5.11.

deep samples.

Looking at the data in Figure 5.11 there are a number of interesting features. Among all 34 samples, only two have a positive ΔU. While this may be indicative of widespread U-removal at high salinities in the Amazon Estuary (which is then transmitted to the nearby ocean) it may also be hinting at the Atlantic end-member itself deviating from the oceanic literature values. Mixed-layer and deep oceanic samples show similar values in both ΔU and $\Delta\delta^{234}$U which are consistently negative. This is in fitting with what was seen in samples from the Eastern Atlantic in Chapter 4 and will be discussed further in Chapter 6. Both samples with positive ΔU were collected at the same location (Figure 5.12), and also both show elevated δ^{234}U. This is interesting as it deviates from the general trend within the estuary of anti-correlation between ΔU and δ^{234}U (Figure 5.9). Other samples with positive $\Delta\delta^{234}$U are located nearby (Figure 5.13), with nearly all of them located in the NW. This may be indicative of a geographically large, high-δ^{234}U release of U toward the outer edges of the Amazon Shelf.

A notable shift takes place in the $\Delta\delta^{234}$U values (Figure 5.11) around salinity ~28 PSU. At lower salinities $\Delta\delta^{234}$U is largely positive, while above 28 PSU all samples

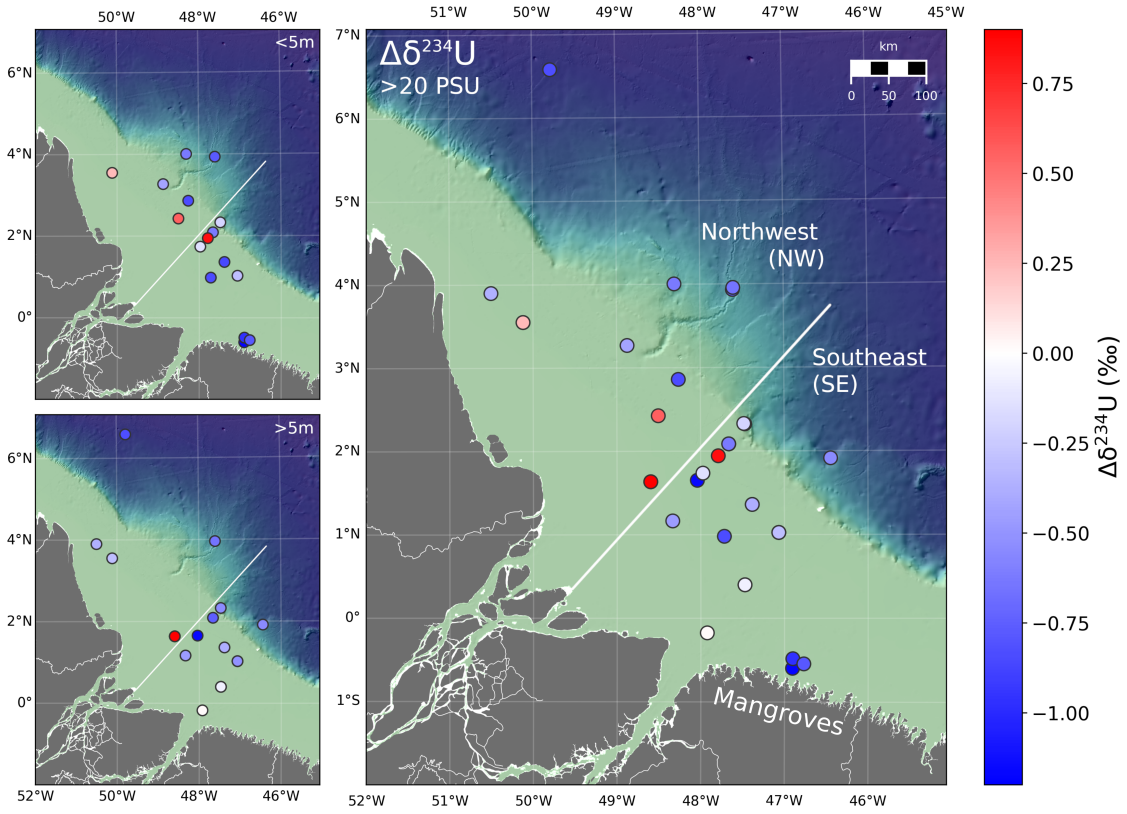

Figure 5.13: A map of the high-salinity (>20 PSU) $\Delta\delta^{234}$U results.

are negative. This shift is more likely to be the result of sampling coverage and a localized effect than an overall estuarine feature. The three samples with δ^{234}U data between 28 and 31 PSU were all collected from just off the coast near the Pará Mangrove Forest (Labeled as 'Mangroves' in Figures 5.11,5.12, and 5.13). These three samples also show a significantly lower δ^{234}U and higher ΔU than nearby samples, which could be indicative of the Mangroves functioning as a low-δ^{234}U source of U similarly to the low-salinity sources identified in Section 5.4.2 (stars in Figures 5.12 and 5.13). A prior study of U behavior in the Ganges-Brahmaputra Estuary and mangrove forest established that the mangroves there function as U-sinks during the low-discharge season due to microbial reduction of U(VI) to U(IV) in the sediments and speculates that this uranium is then released during the high-discharge season (Carroll and Moore, 1993). Such a relationship would explain the results seen here in the near-mangrove samples, as during the low-discharge season the collected U would be likely to have significantly lower δ^{234}U due to having a higher fraction of oceanic water as a result of the contraction of the estuary. Though a fitting theory, without a comparative low-discharge data-set this is impossible to verify.

5.4.4 Overall influence of the Amazon River on Atlantic δ^{234}U

If the Amazon River and Estuary have a significant impact on the δ^{234}U of the Atlantic, this should be detectable in nearby oceanic water which has been influenced by Amazon outflow. Previous studies have used high-precision MC-ICP-MS of δ^{234}U to trace riverine input in the Arctic Ocean over a thousand kilometers offshore (Andersen et al., 2007) and determined these to have a measurable impact on the overall δ^{234}U within the Arctic Ocean even when the low-salinity signature is gone (Andersen et al., 2010). Similarly, it was shown in Chapter 4 that Mediterranean Outflow Water carries an elevated δ^{234}U signature well into the Eastern Atlantic. To assess the overall impact of the Amazon River and Estuary on the Atlantic δ^{234}U, the focus will be on the two groups of oceanic samples shown in Figure 5.11: 'mixed-layer' and 'deep' NBC. As previously mentioned in Section 5.4.3, the mixed-layer samples are much more likely to show influence from Amazon outflow than the deep-water samples. Therefore, a significant difference in δ^{234}U between these two groups of samples would be indicative of Amazon influence.

As seen in Figure 5.14, this is not the case, and the mixed-layer and deep NBC groups of samples have identical average δ^{234}U values of 146.2 ± 0.1‰. Any impact that the Amazon has on nearby Atlantic δ^{234}U appears to be negligible. The Amazon region therefore functions as an overall sink for U and, despite being the world's largest riverine input with a δ^{234}U much higher than the oceanic value, has no measurable impact on the δ^{234}U of the nearby Atlantic.

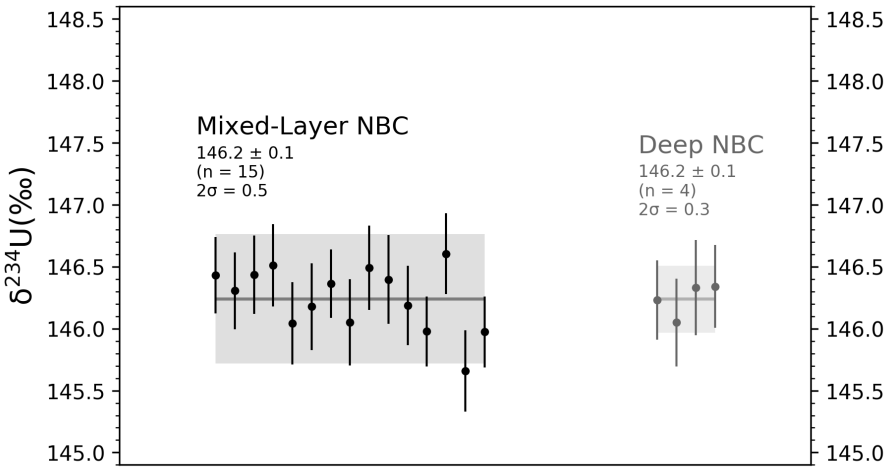

Figure 5.14: Comparison of δ^{234}U from oceanic samples within the mixed-layer (black) and below the mixed-layer (gray). Samples are split as shown in Figure 5.11.

5.5 Summary

Measurements of dissolved U concentration and δ^{234}U from water samples collected throughout the Amazon Estuary region during the high-discharge season show that, rather than functioning as a source of uranium, the Amazon Estuary functions as a sink for oceanic U. This sink shows differing behavior within the estuary, with the northwest behaving as a much stronger sink (up to 90% U removal) than the comparably conservative southeast. Localized sources of U were found adjacent to the strongest sink-like areas which, based on the lowered δ^{234}U in these samples, may be indicative of these locations favoring U-removal during the low-discharge season followed by its re-release during high-discharge. A similar effect was seen in the samples nearest to the Pará Mangroves just south of the Amazon Estuary, indicating that the mangroves may also seasonally switch between being a U-sink and U-source. Despite the complex behavior of U within the Estuary and the Amazon itself having a significantly higher δ^{234}U than the oceans, there appeared to be no noticeable impact from the Amazon on the δ^{234}U of nearby Atlantic samples, pointing towards the Amazon Estuary functioning primarily as a U-sink without significantly altering the isotopic makeup of the Atlantic.

6 Atlantic δ^{234}U disequilibrium

6.1 Introduction

Though not the largest ocean, the Atlantic is arguably the most important when it comes to understanding global circulation, climate, and biogeochemical cycling. Macro circulation in the Atlantic is defined by the so-called Atlantic Meridional Overturning Circulation (AMOC, Figure 6.1), in which warm surface waters are gradually transported northwards where they cool and eventually sink. This sinking water forms North Atlantic Deep Water (NADW) which slowly returns southward, below the northward flowing upper layers. The North Atlantic is one of the few locations world-wide where such deep-water production takes place, and as such it represents an important link between the upper and deep ocean. In general sense, the Atlantic can therefore be viewed as a giant conveyor belt, where thermocline water in the upper Atlantic is brought northwards and the deep Atlantic flows southwards. The boundary between these two flow regimes is generally on the order of 1000 m.

As an integral part of the global ocean, δ^{234}U in the Atlantic has long been thought to be both homogeneous on a ‰ to sub-‰ scale as well as equal to that of other ocean basins such as the Pacific and Indian Oceans (Chen et al., 1986; Delanghe et al., 2002; Andersen et al., 2010). As such, there have been very few high-precision measurements of δ^{234}U in the Atlantic, particularly in the upper reaches of the water column. For example, the most recent global seawater δ^{234}U calibration by Andersen et al. (2010) includes only two measurements from the Atlantic, both of which are from depths greater than 3000m. Uranium inputs to the Atlantic are relatively well constrained. In addition to the Amazon (discussed in Chapter 5), most major rivers flowing into the Atlantic have had their U content analyzed (e.g. Moore, 1967; Martin et al., 1978; Scott, 1982; Palmer and Edmond, 1993; Dunk et al., 2002; Chabaux et al., 2003) and typically show very low concentrations (well below 1μg l^{-1}) and strongly elevated δ^{234}U compared to oceanic values. In fact, among those which have been analyzed only the Congo River (U concentration = 0.08μg l^{-1}, δ^{234}U = 90 ± 70‰ (Martin et al., 1978)) has shown δ^{234}U values likely to be lower than those found in the oceans, although the very low U concentration makes it unlikely that the Congo exerts a significant impact on Atlantic δ^{234}U.

This chapter will focus upon high-precision δ^{234}U measurements from across the Tropical and North Atlantic, with emphasis on basin-wide differences between the upper and deep regimes. It has long been theorized that the surface ocean should have a slightly higher δ^{234}U than the deep ocean due to U-inputs occurring primarily near the surface and removal to the sediments from the deep ocean assumed to be the primary pathway by which U leaves the ocean (Chen et al., 1986). Various studies

Figure 6.1: A schematic view of the Atlantic Meridional Overturning Circulation (AMOC). Warm water is transported northwards where it sinks and returns southwards as North Atlantic Deep Water (NADW). This deep water formation takes place in both the Arctic Ocean and Labrador Sea. Figure adapted from Ruddiman (2001).

of global oceanic δ^{234}U have failed to record a measurable difference and have thus concluded that the surface-deep offset is smaller than the 2σ reproducibility of the apparent average oceanic δ^{234}U (Chen et al., 1986; Andersen et al., 2010). The North Atlantic is an ideal region to investigate such a difference as it is one of the few regions in which the upper and deep ocean interface with one another (in the form of deep-water production). If such a theoretical framework is to be a valid, it must be observable in the upper ocean water which is being transformed to deep water.

After looking into a possible δ^{234}U offset between the upper and deep Atlantic, discussion will move towards determining a probable cause of the altered δ^{234}U in the upper ocean. Ultimately, this will lead to a discussion of the implications of such an offset for both the Atlantic as well as the global U system. An important theme in this section will be proposals for future investigations and measurements. In many cases, specifics of the oceanic U system are not sufficiently well studied to move beyond the realm of speculation. However, this provides ample opportunity for future research in a system which is clearly more dynamic than previously thought.

6.2 Sample overview

Samples are a compilation of high-precision δ^{234}U measurements from across the Equatorial to North Atlantic (Figure 6.2. The 26 samples from the Rockall Trough are shown here for the first time. These were collected in June-July 2016 aboard the RV *L'Atalante* as part of the Mingulay Rockall cruise. The 20 Eastern North Atlantic samples and 19 Amazon Region samples were discussed previously in Chapters 4 (stations UFO-1 and UFO-2) and 5 (all samples above 34 PSU) respectively. All remaining samples are from the literature and consist of 2 deep-sea (depths of 3000m and 5000m) seawater samples from the tropical Atlantic analyzed by Andersen et al. (2010) as well as 7 modern shallow water carbonate skeletons (tropical corals and *Halimeda*) from the near the Bahamas from Robinson et al. (2004a). As these carbonates are modern (i.e. living at the time of collection), they should have a δ^{234}U value which matches that of the ambient seawater. All together, this collection provides a comprehensive overview of North Atlantic δ^{234}U, covering depths spanning from the surface to 5000m.

6.3 Results

The combined δ^{234}U results are shown against depth in Figure 6.3 along with the oceanic δ^{234}U from Andersen et al. (2010). Overall δ^{234}U ranges by almost 3‰ from 144.3 (Rockall Trough, 1000m) to 147.2 (Eastern North Atlantic, 1470m). Among each group of samples, those from the Rockall Trough show the most variability, with values spanning this entire range. All water samples measured as part of this thesis show similar δ^{234}U error (2σ) on the order of 0.3‰.

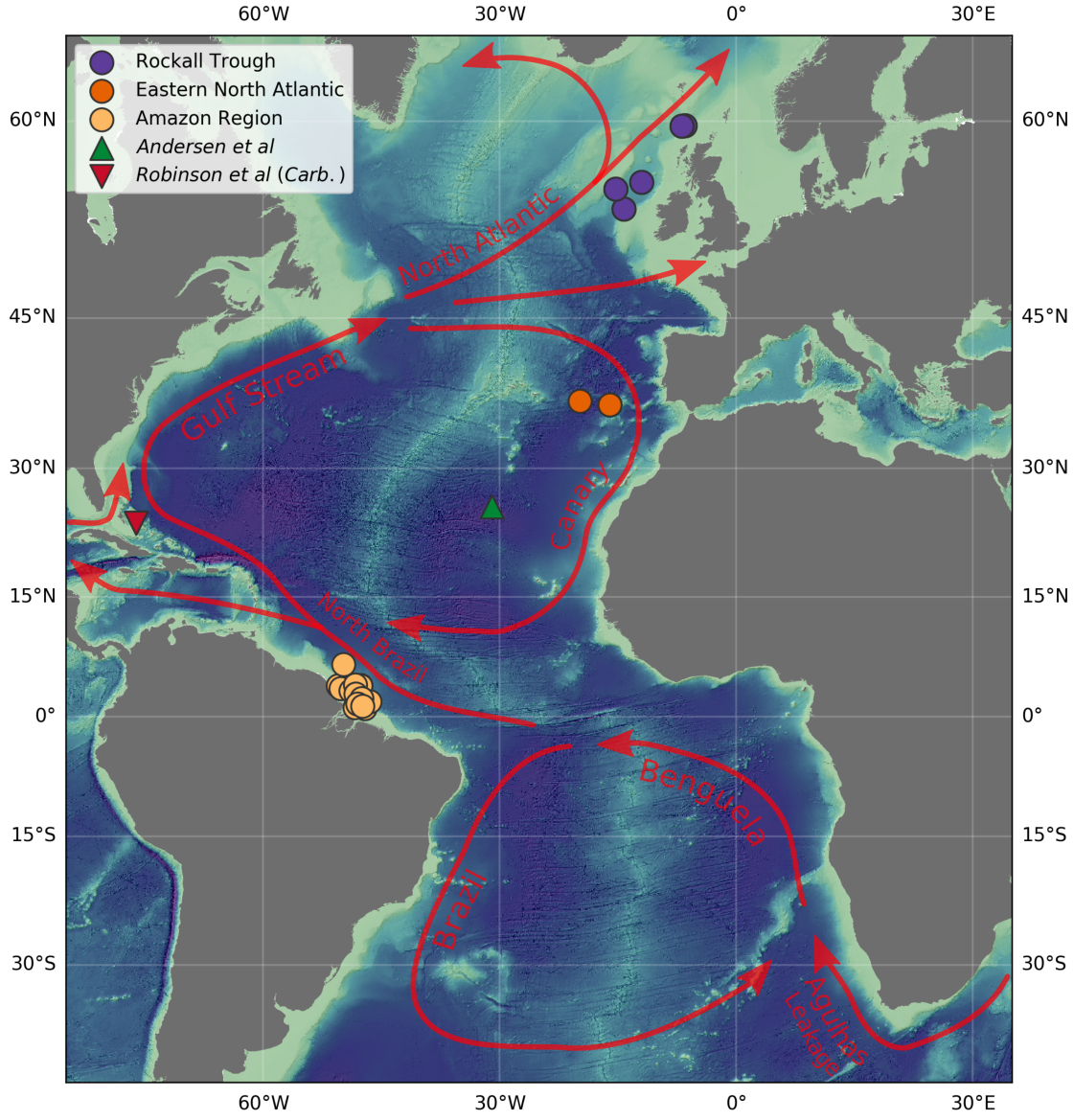

Figure 6.2: Location of samples from the Atlantic. Eastern North Atlantic samples were previously discussed in Chapter 4 (Stations UFO-1 and UFO-2). Western Equatorial Atlantic samples are the 'oceanic' samples (salinity >34 PSU) discussed in Chapter 5. Circles are from this work. Upward pointing green triangles are water samples from Andersen et al. (2010). Downward pointing red triangles represent modern carbonate (coral and *Halimeda*) samples measured by Robinson et al. (2004a).

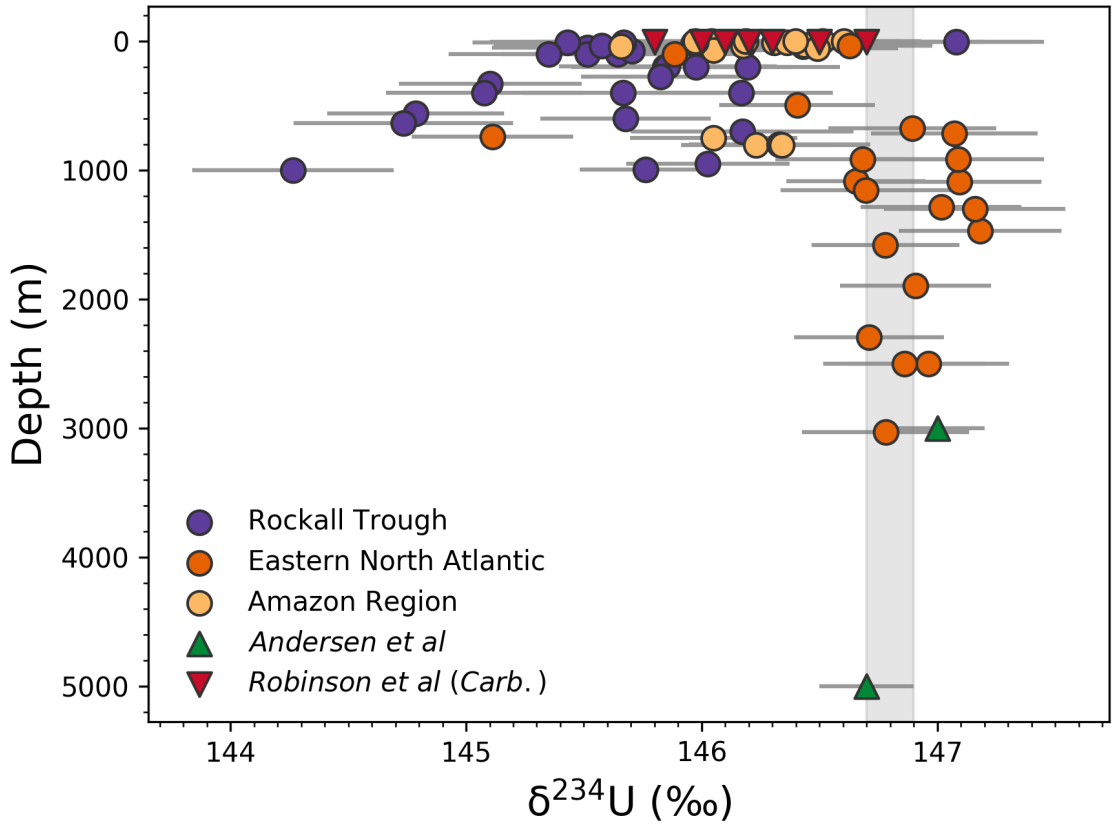

Figure 6.3: δ^{234}U results of all samples from the open Atlantic Ocean. Locations are shown in Figure 6.2. Circles are from this work. Upward pointing green triangles are water samples from Andersen et al. (2010). Downward pointing red triangles are from modern carbonate (coral and *Halimeda*) samples measured by Robinson et al. (2004a).

There exists a clear correlation between sample δ^{234}U and depth. Samples from depths greater than 1000m, are all within error of the oceanic δ^{234}U value from Andersen et al. (2010) of 146.8 ± 0.1‰. At thermocline depths (less than 1000m), the vast majority of samples show significantly lower δ^{234}U values. The overall shift between 'deep' and 'thermocline' samples is on the order of ∼1‰. In addition to this shift, samples from the upper Atlantic display much larger variability than the comparatively uniform deep Atlantic. This will be quantified and discussed further in Section 6.4.1.

6.4 Discussion

To begin discussion will take place about the nature of the δ^{234}U offset between thermocline and deep samples. Afterwards, the source of this offset will be looked into followed by a discussion about the implications of this offset and how it fits into past and future δ^{234}U in the ocean.

6.4.1 δ^{234}U offset between thermocline and deep Atlantic

The observed behavior of δ^{234}U within the upper 1000m in Atlantic demonstrates that δ^{234}U the open ocean is not uniform on a sub-‰ scale, and that deviations even on a ‰-scale are possible. Figure 6.4 shows the average δ^{234}U of samples from Figure 6.3 split between 'upper' (<1000m) and 'deep' (>1000m). Samples from Station UFO-2 (Eastern North Atlantic) which are from within the MOW (as discussed in Section 4.4.1) have been excluded, as well as the shallowest Rockall Trough sample (6m) which has a δ^{234}U (147.1 ± 0.4‰) ∼1‰ higher than all others. Overall, the upper and deep Atlantic show a difference in average δ^{234}U of just under 1‰. The magnitude of this deviation is therefore approximately twice as large as the 0.5‰ offset between the Arctic Ocean (147.3 ± 0.1‰) and the global ocean (146.8 ± 0.1‰) identified by Andersen et al. (2010). In addition to merely showing a different average δ^{234}U value, the upper Atlantic also appears to have much larger variability ($2\sigma = 1.0$‰) in δ^{234}U than the comparatively homogeneous deep Atlantic ($2\sigma = 0.3$‰). This fits with the notion that the upper ocean is in general much less uniform than the deep-sea, being made up of a complex mix of water-masses and currents, each of which may have a distinct biogeochemical composition. Accordingly, the high variability in δ^{234}U at thermocline depths may point towards particular Atlantic water masses being able to be differentiated in terms of δ^{234}U similarly to the Mediterranean water masses in Section 4.4.1.

While an in-homogeneous Atlantic δ^{234}U profile disagrees with previous studies of oceanic δ^{234}U, the reasons for this discrepancy are likely down to two factors: the high-precision of measurements with MC-ICP-MS and the widespread nature of the sampling within the Atlantic. Previous studies of global δ^{234}U which incorporate samples from across the Atlantic water column each utilized either α-spectroscopy (Ku et al., 1977) or TIMS (Chen et al., 1986; Delanghe et al., 2002) and were

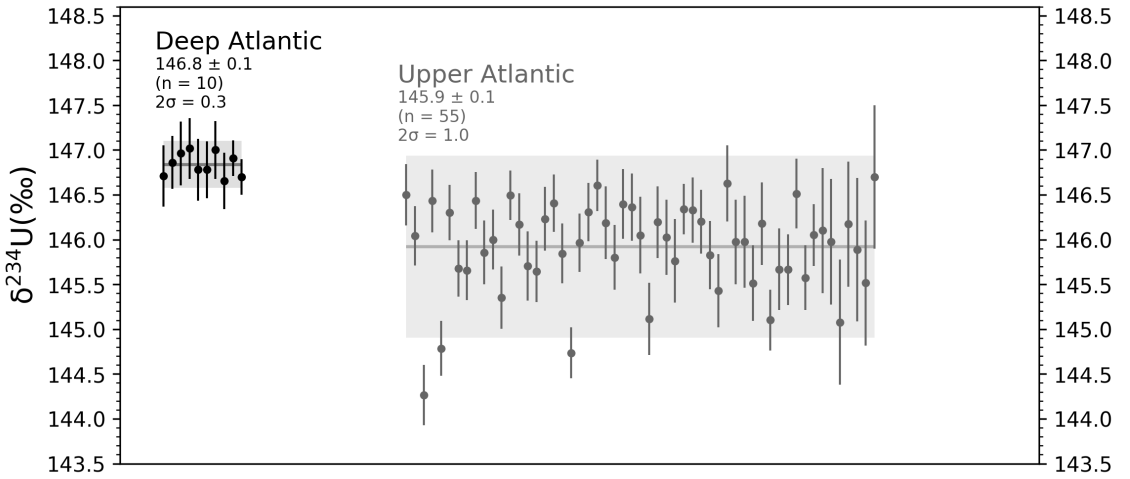

Figure 6.4: Difference in δ^{234}U in the deep and upper(thermocline) Atlantic. Samples from the Eastern North Atlantic from within the MOW (as discussed in Section 4.4.1) are excluded.

unable to reliably resolve differences on the scale of 1-‰. On the other hand, the global δ^{234}U of Andersen et al. (2010) is the result of very precise MC-ICP-MS measurements, yet relies nearly entirely upon samples from the North Pacific and includes only two Atlantic samples. Both of these are from well below the thermocline (>3000m) and agree very well with the NADW measurements from this work (Figure 6.3). For the upper-Atlantic the only comparable MC-ICP-MS measurements are those of modern tropical carbonates from the Bahamas (Robinson et al., 2004a) (red triangles in Figure 6.3). These have an average δ^{234}U of 146.2 ± 0.2‰, in precise agreement with the seawater samples analyzed in this thesis from the Amazon Region, which lies just 'upstream' from the Bahamas with regards to the AMOC. This offset between δ^{234}U in the thermocline- and deep-Atlantic, along with the Mediterranean offset discussed in 4 and the Arctic Ocean offset found in Andersen et al. (2010) point towards the oceans being much more variable in their uranium isotopic makeup than previously believed.

Ideally, more measurements are needed from stations which span both the thermocline and deep regimes. Currently, only the two stations from the Eastern North Atlantic show the transition towards lower δ^{234}U at lower depths. Additionally, there have been as of yet no measurements from the South Atlantic, which does raise the possibility that this is not a basin-wide effect, but rather confined to the Equatorial and North Atlantic. However, as all open-ocean Atlantic data which has been measured thus far fits the trend, it will be assumed for the remainder of the discussion that the observed 1‰ offset in thermocline δ^{234}U is present throughout the Atlantic.

6.4.2 Indian Ocean as source of low-δ^{234}U water

Determining the source of the thermocline-Atlantic δ^{234}U offset is difficult in large part due to a lack of available seawater data which has been measured at sufficient (sub-‰) precision. As of the time of writing only the North Pacific (Andersen et al., 2010), Arctic Sea (Andersen et al., 2007, 2010), and North Atlantic (this thesis) have been broadly analyzed across the water column. Andersen et al. (2010) includes four further measurements, two from the South Pacific and two from the Indian Ocean, however only two of these (Henderson Island surface water from the South Pacific and Northwest Indian Ocean water from 3000m depth) were measured at high-precision using a dual Faraday cup arrangement. Directly tracing the thermocline δ^{234}U offset beyond the North Atlantic, and thus knowing its true extent, is currently not possible and will require more measurements from other ocean basins to determine. However, through combining all extant high-precision seawater δ^{234}U measurements, knowledge of modern ocean circulation, and known riverine U-inputs, it is possible to reasonably speculate about what could conceivably be driving the observed low δ^{234}U values in the thermocline-Atlantic.

Rivers are believed to be by far the largest source of oceanic U, as well as being much more well studied than other sources (e.g. groundwater). They have previously been shown to be capable of causing wide-ranging regional δ^{234}U anomalies in the Arctic Ocean, where high-δ^{234}U riverine inputs were shown to be behind a 0.5‰ enrichment in seawater δ^{234}U (Andersen et al., 2007, 2010). Rivers are therefore the clear choice when attempting to decipher the origin of a large scale oceanic δ^{234}U anomaly. Additionally, the location of the source is likely not in the North Atlantic. Upper ocean transport in the Atlantic (as part of the AMOC) is largely northwards, while the apparent low δ^{234}U values are observed reaching from the Equator until far into the North Atlantic. Each of the thermocline-Atlantic δ^{234}U study sites lies either along major AMOC pathways (e.g. North Brazil Current, Gulf Stream, North Atlantic Current) or areas of re-circulation of these currents (e.g. the Eastern North Atlantic samples along the Canary Current). A signal introduced by a river in e.g. the subtropical or subpolar North Atlantic would be largely propagated northwards and therefore be unlikely to have a large effect on the δ^{234}U of water from the south-lying Amazon region. Thus, to effect all of the analyzed stations, the signal likely originates from south of the Amazon, further 'upstream' with regard to the upper branch of the AMOC.

The most recent compilation of the riverine uranium input by Chabaux et al. (2003) lists 35 major rivers which have been analyzed for both uranium concentration and δ^{234}U. Taking the combined U flux, these rivers account for approximately 50% of total uranium input to the ocean according to estimated oceanic U-budgets (Dunk et al., 2002; Henderson, 2002). When compared to the ocean, the average U concentration of these rivers is relatively low (0.5 μg l^{-1}) and the δ^{234}U is relatively high (171‰) (Chabaux et al., 2003). The thermocline-Atlantic appears to show influence from a very large, low-δ^{234}U source relative to the oceans. This excludes the majority of analyzed rivers. Additionally, balanced budget calculations for oceanic

U have predicted that in order to uphold the elevated δ^{234}U in the ocean (i.e. well above unity), the overall riverine input must have an even higher δ^{234}U of 223‰ (Henderson, 2002). This indicates that the ∼50% of river input not yet analyzed or included in the compilation by Chabaux et al. (2003) would, on average, be even higher in δ^{234}U than those included in producing the average riverine value.

Given all of this, the clearest candidate for a large-scale, low-δ^{234}U source of oceanic U are the three major rivers originating in the Himalayas and draining into the Indian Ocean: the Indus, Ganges, and Brahmaputra rivers. These are relative outliers, with very high U concentration (1-5μg l^{-1}) and δ^{234}U values lower than those found in the ocean (δ^{234}U = 26-50‰) (Chabaux et al., 2001), yet due to their high concentrations account for approximately 20% of all ocean U-input from rivers (Chabaux et al., 2003). Though these drain into the Indian Ocean, there are a number of reasons why it is believable that they may heavily impact δ^{234}U in the upper Atlantic. As part of the global THC (Figure 2.1) the Indian Ocean is a major source water to the upper Atlantic in the form of the Agulhas Leakage (shown in Figure6.2) with an estimated inflow of approximately 5-15 Sv (de Ruijter et al., 1999; Richardson, 2007). This then merges with the Benguela Current and gradually travels northwards as part of the upper branch of the AMOC. The total northward transport of the AMOC has been variously estimated to be 12-19 Sv (Lumpkin and Speer, 2007; Talley, 2013; McCarthy et al., 2015; Meinen et al., 2018; Cessi, 2019) and as such, the Agulhas Leakage would constitute a sizable portion of this. Previous studies have shown that roughly half of all water from the Agulhas Leakage makes its way into the North Atlantic (Rühs et al., 2013) and that this has a marked effect on Atlantic salt and heat budgets (Weijer et al., 2001; Biastoch et al., 2009; Lübbecke et al., 2015). It is therefore reasonable to assume that Agulhas Leakage could also have an effect on the uranium budget of the North Atlantic as well if δ^{234}U in the Indian Ocean (and by extension the Agulhas Leakage) were to be significantly divergent. Following the AMOC, this signal may then be propagated northwards and consequently affect the stations analyzed in this thesis.

To date, there have been no high-precision δ^{234}U measurements from the upper Indian Ocean. Given the δ^{234}U results in the Atlantic, future high-precision analysis across the water column would reveal systematic differences in the Indian Ocean between the upper and deep ocean, with the upper ocean showing a markedly lower δ^{234}U. Due to deep-water propagation as part of the THC, deep water in the Indian Ocean is likely to be very similar to that in the Pacific and NADW, as they share a common origin. This is backed up by the lone deep-water measurement from the Indian Ocean by (Andersen et al., 2010), which is within error of the average oceanic value found in the Pacific and deep Atlantic. TIMS analysis of seawater samples by Delanghe et al. (2002) from various depths in the the Mediterranean, Northeast Atlantic, Pacific, and Indian Ocean, found the average δ^{234}U to be 2-3‰ lower in the Indian Ocean than all other analyzed basins. Additionally, there existed greater variability among δ^{234}U values within the Indian Ocean (1σ = 4.8‰) than all others (0.6-1.7‰). Interestingly, within the Indian Ocean the lowest δ^{234}U values appear to be clustered at thermocline depths between 142-1048m. The average δ^{234}U values

within this depth range were 143.5±1.7‰ (n=3) while samples outside of this depth range had a notably higher average of 150.2±1.6‰ (n=5). This may be indicative of a split between the upper and deep ocean, however given that typical uncertainties for each individual measurement are on the order of 5-6‰, a high-precision MC-ICP-MS reanalysis would be necessary to draw any firm conclusions.

6.4.3 Implications for δ^{234}U in the global ocean

An offset in the δ^{234}U between the upper and deep Atlantic has implications for the entire global ocean U system and goes beyond merely demonstrating systemic variability in a system previously considered to be largely homogeneous. Particularly interesting is the direction of the offset, with the upper Atlantic having a lower δ^{234}U than its deeper counterpart, which is in direct contradiction to conventional models of oceanic uranium (Chen et al., 1986). Due to the overall δ^{234}U in the oceans being above unity, it has long been theorized that in order for the ocean to remain in steady-state, there should be a slight positive difference between the upper and deep ocean. This is due to U-inputs occurring primarily near the surface and U removal to sediments largely occurring in the deep ocean (Chen et al., 1986). Previous studies have used this theoretical difference, as well as the assumption that the system is in steady-state, to constrain the mixing time for the global ocean to no longer than ∼1000 years (Chen et al., 1986; Andersen et al., 2010). This model is not consistent, however, with a negative δ^{234}U in the upper ocean compared to the deep ocean. This is particularly so for the North Atlantic as it is one of the very few places worldwide where surface water is actively transformed into deep water, which is then distributed throughout the worlds oceans as part of the THC. As it appears unlikely that there are large unaccounted-for U-sources in the deep-sea (given the apparently identical δ^{234}U in the deep Atlantic and Pacific) and that, without inputs, nuclear decay causes δ^{234}U to gradually return towards unity (i.e. go down), the δ^{234}U of the upper North Atlantic essentially constitutes an 'upper limit' on future deep-sea values.

Low δ^{234}U in the upper Atlantic is therefore likely indicative of the system not being in steady state, and that oceanic δ^{234}U is currently decreasing with time. This is fitting with what is seen in past records of Atlantic δ^{234}U based on the U-series dating of the carbonate skeletons of cold-water corals. Figure 6.5 shows the last 60 kyrs of the Heidelberg δ^{234}U Record (AUR), a compilation of over 1000 δ^{234}U values (further information available in (Krengel, 2020)) reconstructed as part of the process of dating the carbonate skeletons of Cold Water Corals (CWC) using U-series methods (Cheng et al., 2000). The purple line represents a 2 kyr (centered) running mean of the AUR data. Compared to the LGM, Holocene δ^{234}U is much less variable but still shows a near-linear downward trend following the peak at around 15 kyr ago, with a similar decline having been previously shown to have taken place simultaneously in the Mediterranean (Krengel, 2020). A linear regression of this

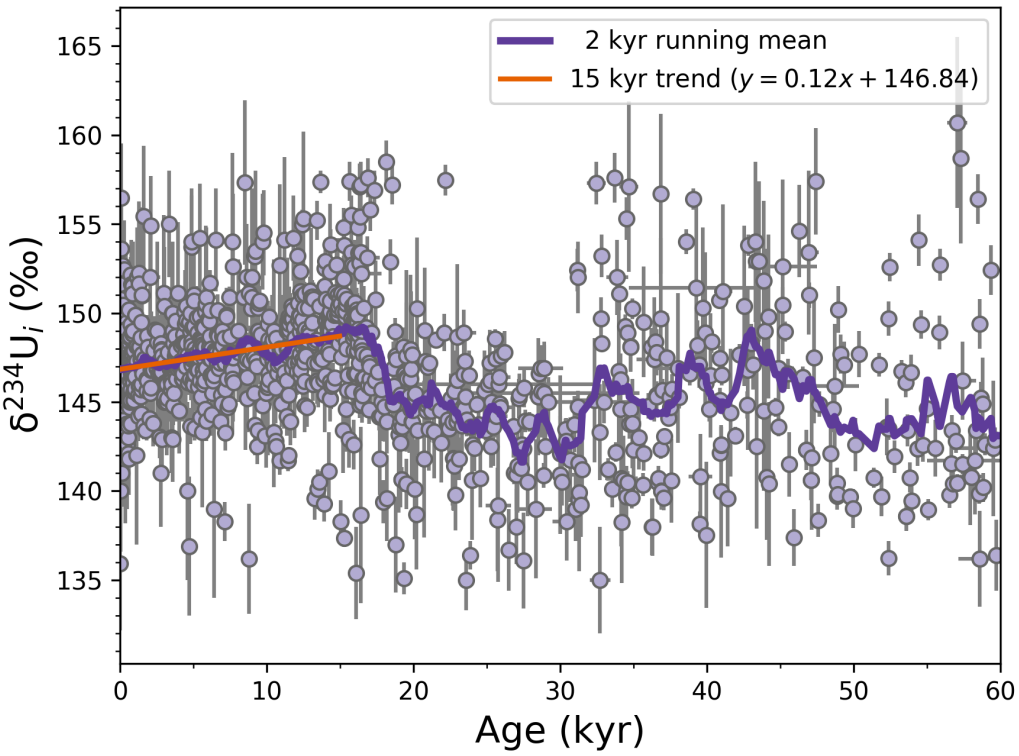

Figure 6.5: Atlantic δ^{234}U over the last 60 kyr. Data is from the IUP Heidelberg Atlantic Uranium Record (AUR), a collection of previously published δ^{234}U values based on the U-series dating of cold-water corals (sources are in text).

trend (shown in orange) leads to the relationship:

$$\delta^{234}U = 0.12 * Age + 146.84 \tag{6.1}$$

where *Age* is the age of the sample in kyr. This linear trend indicates an average Atlantic δ^{234}U value which has decreased from 148.7‰ to 146.8‰ over the past 15 thousand years at a rate of just over 0.1‰ per kyr. Interestingly, the modern value (i.e. 0 kyr) of this linear fit corresponds precisely with the modern δ^{234}U in the deep Atlantic. The low δ^{234}U seen in upper Atlantic seawater could therefore be indicative that this trend is ongoing and may even be increasing given that the ∼1‰ offset between upper and deep Atlantic would be equivalent to nearly half of the overall ∼2‰ decrease seen over the past 15 kyr.

One factor which may dampen the effect of the upper Atlantic offset and bring it more in line with historical trends, is mixing with water originating from the Arctic Ocean during the process of transformation to NADW. As previously mentioned, the Arctic Ocean has been shown to have an opposite (positive) offset in δ^{234}U (Andersen et al., 2007, 2010) relative to the deep Atlantic of 0.5‰. Dense, cold Arctic Sea water which overflows the Greenland-Scotland ridge is an important contributor to NADW and has been shown to account for roughly 20-50% of all deep water formation in the North Atlantic with the remainder sourced from the upper Atlantic either through downwelling in the Labrador Sea or entrainment by arctic overflow currents (LeBel et al., 2008; Ferreira and Kerr, 2017). The U composition of newly formed NADW should be representative of this fractional mixing of these water-masses. Using the Arctic ocean end-member from Andersen et al. (2010) of 147.3‰ and the upper Atlantic end-member from Figure 6.4 of 145.9‰, this would place the expected δ^{234}U of modern newly-formed NADW somewhere between 146.2-146.6‰. This is roughly 0.2-0.6‰ lower than the δ^{234}U measured at at stations in the Eastern North Atlantic, however if it is assumed that the δ^{234}U in the ocean is decreasing, this lower δ^{234}U signal may not yet have penetrated so far south. Deep water propagation occurs very slowly and as such the NADW analyzed in the Eastern North Atlantic likely represents deep water which was formed somewhere between 200-300 years ago (Matsumoto, 2007). Essentially, as part of the process of oceanic δ^{234}U decreasing (as is indicated by the AUR data), NADW forming today would be expected to have a lower δ^{234}U than 'older' NADW found further along the flow-path. This therefore fits with the predicted δ^{234}U of newly formed NADW being lower than the NADW measured at stations away from deep water formation sites.

While the AUR and the predicted δ^{234}U of newly formed NADW both show a downward trend, the speed of this trend does not necessarily align. Assuming a conservative estimate of 300 years transit time between deep water formation and its arrive in the Eastern North Atlantic, a 0.2-0.6‰ difference in δ^{234}U would represent a trend of 0.7-2.0‰/kyr, which is much larger than the 0.12‰/kyr trend seen in the AUR (Figure 6.5). Accordingly, this may imply a speeding up of the process of oceanic δ^{234}U decreasing. It was put forward in Section 6.4.2 that the low δ^{234}U in the upper Atlantic may be due to input from the Indian Ocean via

the Agulhas Leakage. This leakage is not constant and has been shown to have been strongly increasing since at least the 1970s by 1.2 Sv per decade as a result of anthropogenically driven atmospheric circulation changes (Biastoch et al., 2009). This signal requires only two decades to reach as far as the Gulf Stream (Rühs et al., 2013), from which it is then distributed throughout the North Atlantic. If inputs of low-δ^{234}U water from the Indian Ocean is the cause of the low-δ^{234}U seen in the upper Atlantic, then a recent and sustained increase in these inputs could also be connected to the apparent acceleration in the decrease of δ^{234}U in NADW.

Much of this is largely speculative and would require further measurements to prove. An ideal investigation would be to sample in and around the Labrador Sea, close to where NADW is formed. This would give an idea of whether the low-δ^{234}U signal from the upper Atlantic is actually being transferred to the deep Atlantic. It may be the case that the signal is diluted by the enriched δ^{234}U of the Arctic Ocean and the end result is a value similar to that of the NADW and Pacific. However, assuming that there are signs of lowered δ^{234}U in Labrador Sea NADW (such as the predicted values of 146.2-146.6‰), a second step would be to sample along the Western Atlantic following the primary NADW pathways. This should show a noticeable trend of increasing δ^{234}U as one travels further from the Labrador Sea and encounters progressively 'older' NADW. With regard to the possible anthropogenically driven acceleration of this downward trend in δ^{234}U, this depends first upon determining whether the upper Indian Ocean and/or Agulhas Current itself has notably low δ^{234}U (as discussed in Section 6.4.2). If this is not the case, then the cause of the low δ^{234}U signal in the upper Atlantic lies elsewhere, and recent increases in Agulhas Leakage are unlikely to have affected the Atlantic uranium isotopic balance.

6.5 Summary

Seawater samples from across the Atlantic show δ^{234}U approximately 1‰ lower at thermocline depths (<1000 m) than in the deep-sea (>1000 m). Deep-sea samples agree well with previously published values for global oceanic δ^{234}U, which were based primarily on measurements from the North Pacific. The source of this low-δ^{234}U water is theorized to be large Himalayan-sourced rivers which output large amounts of low-δ^{234}U uranium into the Indian Ocean, where δ^{234}U has not yet been thoroughly analyzed. This signal is then transported to the Atlantic via the Agulhas Leakage. The presence of lower δ^{234}U in the upper ocean than at depth, particularly so close to major centers of deep-water production, implies that the oceanic U system is not in steady state, but rather that oceanic δ^{234}U is slowly decreasing. This is backed up by Atlantic δ^{234}U records from the skeletons of cold water corals, which show a near-linear trend of decreasing δ^{234}U over the past 15 kyr. The observed difference between the upper and deep Atlantic is larger than that which would be implied by the 15 kyr linear trend and therefore implies that the decrease in oceanic δ^{234}U is currently accelerating, possibly linked to recent anthropogenically driven increases in Agulhas Leakage.

7 Conclusions and Outlook

High-precision MC-ICP-MS measurements of seawater δ^{234}U from across the Mediterranean Sea, Amazon Region, and North Atlantic show that the isotopic makeup of oceanic uranium is much less homogeneous than previously believed. The observed variability is largely systematic in nature, with δ^{234}U differing on a ‰-scale across various water masses and regions. Very few locations in the world's oceans have thus far been analyzed at such high-precision, and these results point toward further δ^{234}U variations waiting to be discovered. This raises interesting questions about both the cycling of uranium in the oceans as well as the stability of its current isotopic makeup.

Chapter 4 focused on the Mediterranean Sea, where water masses showed a 1-2‰ enrichment in δ^{234}U relative to nearby Atlantic samples. The magnitude of this enrichment increased alongside the average residence time of the water mass in question, with the highest values being found in upwelled Western Mediterranean Deep Water (WMDW) in the Alboran Sea ($\delta^{234}\text{U} = 148.3 \pm 0.1$‰). To investigate the cause of this offset, various groundwater and nearby seawater samples from the Gulf of Lions (an important region for the formation of WMDW) were analyzed. The groundwater samples were found to have δ^{234}U values hundreds of permil higher than those found in Mediterranean seawater. Many of the local seawater samples themselves showed elevated δ^{234}U values of approximately 149-150‰, which were often able to be traced back to specific sites of submarine groundwater discharge. Using the basin-wide seawater results, a simple mass-balance model of the Mediterranean was constructed to investigate the uranium inputs which give rise to the observed offset. The results of this model were compared with previously published data on the U content of Mediterranean rivers as well as the measured groundwater samples. Ultimately, it was found that groundwater is likely to play an important role in the formation of the Mediterranean δ^{234}U offset, as the groundwater samples were much more similar than known rivers to the U-input predicted by the model.

Afterwards, in Chapter 5, focus shifted to δ^{234}U in and around the Amazon Estuary. The analysis focused upon providing good coverage both geographically as well as across the estuarine salinity gradient. Each sample was compared with ideal conservative mixing between presumed Amazon and Atlantic end-members based upon the salinity of the sample. This revealed an estuarine system in which uranium behavior is highly variable, with the northwest of the estuary behaving more like a uranium sink (with up to 90% U removal) and the southeast more conservatively. Scattered throughout were a number of highly localized U-sources. With regards to conservative mixing, sink areas were strongly associated with elevated δ^{234}U, possibly indicative of an enhanced α-recoil effect at these locations. Source areas on

the other hand were marked by lowered δ^{234}U, which could be indicative of seasonal changes in the behavior of U within the estuary. Analysis of nearby Atlantic samples showed no signs of altered δ^{234}U which, in addition to the low U concentration of the river end-member as well as the estuaries largely sink-like behavior, points towards the Amazon having little to no measurable impact on Atlantic δ^{234}U.

Finally, Chapter 6 combined new measurements with relevant samples from previous chapters to focus on δ^{234}U differences within the Atlantic Ocean. It was revealed that the upper (thermocline) Atlantic has an average δ^{234}U which is approximately 1‰ lower than in the deep Atlantic. Upper Atlantic values also showed considerably larger variability than the deep Atlantic, which was comparatively homogeneous. It was put forward that this offset may be the result of a low-δ^{234}U signal originating from the Indian Ocean and introduced to the Atlantic by way of the Agulhas Leakage. That the upper ocean has a lower δ^{234}U than the deep ocean indicates that the system is not in steady state but rather slowly decreasing, in agreement with the δ^{234}U trend seen in Holocene cold-water coral skeletons.

The results in this thesis open up a number of interesting possibilities for further work. Most generally, it has become clear that when looked at on the ‰ or sub-‰ scale, oceanic δ^{234}U is a surprisingly dynamic system which remains as-of-yet largely unstudied at such high-precision. As a first step, it is crucial that further measurements are carried out in the Atlantic so as to confirm the observed offset between upper- and deep-water, ideally with as wide a geographical scope as possible. Focus on deep-water along the western edge of the North Atlantic (from the Labrador Sea southward) may show a gradient in δ^{234}U, giving insight into any possible shift in newly-formed deep water. Beyond the Atlantic, the most tantalizing area for study is the Indian Ocean, which is theorized to carry a low δ^{234}U value at thermocline depths. Measurements in the Indian Ocean or Agulhas Current could confirm whether the low upper Atlantic values originate there or elsewhere. Moving beyond areas directly connected to this thesis, another interesting area to analyze would be the Southern Ocean. It is integrally involved in global circulation, serving as the 'crossroads' of the THC. It is both the major connection between the Atlantic, Indian, and Pacific Oceans, as well as an area of deep-water production. If ‰-scale δ^{234}U variability is a widespread phenomenon beyond the Atlantic, it is almost certainly observable in the Southern Ocean.

One thing which became increasingly clear over the course of this work was just how much remains unknown regarding riverine and groundwater uranium inputs to the ocean. This is likely at least partially due to the prevailing notion that oceanic uranium is largely homogeneous and, as such, not an exciting prospective system to study in-depth. Constraining riverine input is no easy task, as it can be highly seasonally or even annually variable, as well as requiring careful analysis of any associated estuarine system. For example, the Amazon samples analyzed here were all collected during the high-discharge season, and the observed estuarine dynamics are likely to function much differently during the low-discharge season when the salinity gradient contracts. Regardless, further constraining oceanic U-input from rivers would provide a powerful tool for indirectly investigating other

inputs, specifically submarine groundwater. If more data existed on the uranium content of Mediterranean rivers, it would have been possible to provide an estimate of the uranium content of Mediterranean groundwater. However since so few rivers have thus far been comprehensively analyzed it was not possible to separate the groundwater and riverine sources. If river and groundwater U content becomes much more well constrained over time, it may even be possible to utilize these in such simple mass balance models to help estimate the total volume of global groundwater discharge, a value for which current estimates range over nearly an order of magnitude.

One of the advantages of this technique is that the sampling process is, in comparison to many other biogeochemical systems, very easy. It is therefore almost trivial to include δ^{234}U analysis as part of any research cruise which was already planning to carry out CTD measurements. Very little water is required, and samples need only be treated with a small amount of HCl. Samples need not be stored in special conditions or measured within a certain time-frame. With the proper equipment and expertise, sample preparation and measurement are also relatively straight-forward. In all, high-precision analysis of dissolved δ^{234}U is an easily approachable yet largely unstudied field, promising many new and interesting discoveries.

Appendix

A Data

A.1 Mediterranean Sea

Lab Number	Station	Latitude	Longitude	Depth m	Salinity PSU	Temperature °C	^{238}U μg l^{-1}	2σ	δ^{234}U ‰	2σ
9019	UFO-4	37.2588	0.1682	1099	38.49	13.12	3.5080	5.9E-05	148.0	0.3
9020	UFO-4	37.2588	0.1682	999	38.49	13.14	3.6777	5.8E-05	148.1	0.3
9021	UFO-4	37.2588	0.1682	999	38.49	13.14	3.5883	6.7E-05	148.2	0.3
9022	UFO-4	37.2588	0.1682	899	38.50	13.16	3.5371	6.7E-05	148.0	0.3
9023	UFO-4	37.2588	0.1682	798	38.52	13.20	3.5093	6.5E-05	147.8	0.3
9025	UFO-4	37.2588	0.1682	599	38.54	13.30	3.5009	6.3E-05	146.9	0.3
9433	UFO-4	37.2588	0.1682	1488	38.48	13.14			147.9	0.3
9434	UFO-4	37.2588	0.1682	1386	38.48	13.13			147.9	0.3
9435	UFO-4	37.2588	0.1682	1299	38.48	13.12			147.7	0.3
9436	UFO-4	37.2588	0.1682	1198	38.48	13.12			147.7	0.4
9437	UFO-4	37.2588	0.1682	1099	38.49	13.12			147.9	0.3
9438	UFO-4	37.2588	0.1682	999	38.49	13.14			147.8	0.3
9439	UFO-4	37.2588	0.1682	899	38.50	13.16			147.6	0.3
9440	UFO-4	37.2588	0.1682	798	38.52	13.20			147.7	0.3
9441	UFO-4	37.2588	0.1682	699	38.53	13.25			147.9	0.3
9442	UFO-4	37.2588	0.1682	599	38.54	13.30			147.7	0.3
9443	UFO-4	37.2588	0.1682	499	38.56	13.38			147.4	0.3
9444	UFO-4	37.2588	0.1682	399	38.57	13.44			147.6	0.3
9445	UFO-4	37.2588	0.1682	299	38.54	13.49			147.3	0.3
9446	UFO-4	37.2588	0.1682	202	38.43	13.46			146.8	0.3
9447	UFO-4	37.2588	0.1682	85	38.11	14.24			147.3	0.3
9448	UFO-4	37.2588	0.1682	44	37.30	15.16			147.1	0.3
9449	UFO-4	37.2588	0.1682	20	36.92	23.52			146.6	0.3
9450	UFO-4	37.2588	0.1682	13	36.93	23.53			146.7	0.3
9050	UFO-5	38.4325	12.0875	86	38.15	15.17	3.4314	7.0E-05	147.3	0.8
9051	UFO-5	38.4325	12.0875	50	37.57	16.14	3.4067	4.2E-05	147.0	0.3
9052	UFO-5	38.4325	12.0875	19	37.87	22.48	3.4544	7.0E-05	147.5	0.7
9451	UFO-5	38.4325	12.0875	1537	38.53	13.34			148.0	0.3
9452	UFO-5	38.4325	12.0875	1435	38.53	13.33			147.6	0.4
9453	UFO-5	38.4325	12.0875	1337	38.54	13.33			147.8	0.3
9454	UFO-5	38.4325	12.0875	1238	38.54	13.33			147.8	0.3
9455	UFO-5	38.4325	12.0875	1139	38.55	13.33			147.8	0.3
9456	UFO-5	38.4325	12.0875	1040	38.55	13.34			148.0	0.3
9457	UFO-5	38.4325	12.0875	940	38.56	13.37			148.2	0.3
9458	UFO-5	38.4325	12.0875	842	38.58	13.41			148.0	0.3
9459	UFO-5	38.4325	12.0875	743	38.62	13.53			147.7	0.3
9460	UFO-5	38.4325	12.0875	643	38.67	13.73			147.4	0.3
9461	UFO-5	38.4325	12.0875	546	38.75	14.02			147.7	0.3
9462	UFO-5	38.4325	12.0875	447	38.83	14.32			147.5	0.3
9463	UFO-5	38.4325	12.0875	337	38.86	14.49			147.4	0.4
9464	UFO-5	38.4325	12.0875	242	38.83	14.54			147.8	0.3
9465	UFO-5	38.4325	12.0875	199	38.82	14.75			148.1	0.3
9466	UFO-5	38.4325	12.0875	118	38.29	14.52			147.1	0.3
9053	UFO-6	35.9858	21.0603	2971	38.73	13.93	3.5545	5.2E-05	147.7	0.4
9054	UFO-6	35.9858	21.0603	2772	38.73	13.89	3.5261	4.9E-05	148.3	0.4
9055	UFO-6	35.9858	21.0603	2575	38.74	13.87	3.5280	3.8E-05	147.9	0.3
9056	UFO-6	35.9858	21.0603	2377	38.74	13.85	3.5147	5.2E-05	148.1	0.4

Lab Number	Station	Latitude	Longitude	Depth	Salinity	Temperature	^{238}U	2σ	$\delta^{234}U$	2σ
				m	PSU	°C	$\mu g\ l^{-1}$		‰	
9057	UFO-6	35.9858	21.0603	2178	38.74	13.85	3.5521	4.0E-05	147.9	0.3
9058	UFO-6	35.9858	21.0603	1981	38.75	13.84	3.5155	5.3E-05	147.9	0.4
9059	UFO-6	35.9858	21.0603	1784	38.75	13.83	3.5466	4.4E-05	148.3	0.3
9060	UFO-6	35.9858	21.0603	1585	38.76	13.82	3.5127	5.0E-05	147.7	0.5
9061	UFO-6	35.9858	21.0603	1387	38.76	13.80	3.5383	4.5E-05	148.2	0.4
9062	UFO-6	35.9858	21.0603	1190	38.76	13.80	3.5460	4.3E-05	147.8	0.4
9064	UFO-6	35.9858	21.0603	793	38.80	13.89	3.5340	4.6E-05	147.4	0.3
9065	UFO-6	35.9858	21.0603	596	38.85	14.12	3.5221	4.8E-05	148.0	0.4
9066	UFO-6	35.9858	21.0603	398	38.95	14.62	3.5492	4.1E-05	147.7	0.3
9067	UFO-6	35.9858	21.0603	200	39.00	15.30	3.5471	4.1E-05	147.1	0.3
9068	UFO-6	35.9858	21.0603	150	39.08	15.85	3.5479	4.3E-05	147.1	0.3
9069	UFO-6	35.9858	21.0603	103	39.05	16.42	3.5543	3.9E-05	147.1	0.3
9070	UFO-6	35.9858	21.0603	51	39.25	23.08	3.5817	5.0E-05	147.9	0.3
9071	UFO-7	38.1942	24.7937	538	38.94	14.13	3.5802	4.3E-05	148.2	0.3
9072	UFO-7	38.1942	24.7937	497	38.93	14.10	3.5319	4.4E-05	147.6	0.3
9073	UFO-7	38.1942	24.7937	448	38.95	14.17	3.5616	4.2E-05	148.2	0.2
9074	UFO-7	38.1942	24.7937	418	38.96	14.22	3.5662	3.8E-05	148.2	0.3
9075	UFO-7	38.1942	24.7937	399	38.94	14.18	3.5436	3.8E-05	147.9	0.3
9077	UFO-7	38.1942	24.7937	320	38.94	14.28	3.5982	4.4E-05	148.0	0.2
9078	UFO-7	38.1942	24.7937	299	38.94	14.32	3.5647	3.8E-05	148.0	0.2
9079	UFO-7	38.1942	24.7937	280	38.94	14.35	3.5447	4.1E-05	147.4	0.3
9080	UFO-7	38.1942	24.7937	260	38.95	14.43	3.6098	4.00E-05	147.5	0.3
9081	UFO-7	38.1942	24.7937	239	38.94	14.44	3.5342	4.20E-05	147.5	0.3
9082	UFO-7	38.1942	24.7937	221	38.95	14.5	3.5918	3.90E-05	147.7	0.3
9083	UFO-7	38.1942	24.7937	201	38.95	14.53	3.7485	4.20E-05	147.8	0.3
9084	UFO-7	38.1942	24.7937	181	38.95	14.56	3.5904	3.70E-05	147.8	0.2
9085	UFO-7	38.1942	24.7937	161	38.88	14.4	3.539	4.00E-05	147.9	0.2
9086	UFO-7	38.1942	24.7937	142	38.93	14.68	3.611	4.10E-05	148	0.2
9087	UFO-7	38.1942	24.7937	121	39.03	15.18	3.6206	3.70E-05	147.6	0.3
9088	UFO-7	38.1942	24.7937	102	39.08	15.45	3.6064	3.70E-05	147.5	0.3
9089	UFO-7	38.1942	24.7937	80	39	15.6	3.574	4.20E-05	147.5	0.3
9090	UFO-7	38.1942	24.7937	63	39.01	16.17	3.5669	3.90E-05	147.5	0.3
9091	UFO-7	38.1942	24.7937	48	38.96	17.4	3.6493	4.20E-05	147.8	0.3
9092	UFO-7	38.1942	24.7937	32	39.01	19.66	3.5816	8.50E-05	147.8	0.3
9093	UFO-7	38.1942	24.7937	23	38.57	20.06	3.5337	4.60E-05	148.1	0.3
8428	Geob18101-1	35.4299	-2.5155	150	37.95	14.16	3.4926	8.80E-05	147.4	0.4
8429	Geob18101-1	35.4299	-2.5155	60	36.78	15.05	3.3709	1.00E-04	146.7	0.6
8430	Geob18101-1	35.4299	-2.5155	21	36.76	15.06	3.365	8.80E-05	147	0.5
8570	Geob18101-1	35.4299	-2.5155	450	38.48	13.15	3.5435	4.40E-05	148.3	0.3
8571	Geob18101-1	35.4299	-2.5155	400	38.48	13.14	3.5629	4.70E-05	148.4	0.3
8572	Geob18101-1	35.4299	-2.5154	349	38.48	13.14	3.5678	4.30E-05	148.5	0.3
8573	Geob18101-1	35.4299	-2.5155	300	38.45	13.19	3.5701	5.40E-05	148.2	0.3
8574	Geob18101-1	35.4299	-2.5155	240	38.42	13.17	3.5699	5.10E-05	148	0.3
8575	Geob18101-1	35.4299	-2.5155	150	37.95	14.16	3.5217	4.40E-05	147.8	0.3
8576	Geob18101-1	35.4299	-2.5155	60	36.78	15.05	3.41	4.30E-05	147.5	0.3
8577	Geob18101-1	35.4299	-2.5155	21	36.76	15.06	3.4051	4.50E-05	147.3	0.3
8568	Geob18110-1	35.3315	-2.4935	219	38.44	13.18	3.5162	3.60E-05	148.3	0.3
8569	Geob18110-1	35.3315	-2.4935	20	36.78	15.06	3.5125	4.40E-05	147.1	0.3

A.2 Gulf of Lions: coastal samples

Lab Number	Location	Latitude	Longitude	Depth	Salinity	Temperature	^{238}U	2σ	$\delta^{234}U$	2σ
				m	PSU	°C	$\mu g\ l^{-1}$		‰	
9473	Calanques	43.2060	5.4166	0	37.1		3.1351	5.9E-05	148.2	0.3
9474	Calanques	43.2042	5.4166	0	37.0		3.2910	6.4E-05	147.8	0.3
9475	Calanques	43.2012	5.4166	0	38.3		3.2885	5.9E-05	148.2	0.3
9476	Calanques	43.2087	5.4245	0	38.0		3.2065	6.2E-05	147.9	0.3
9477	Calanques	43.2073	5.4282	0	38.2		3.3695	6.1E-05	147.3	0.3
9478	Calanques	43.2051	5.4319	0	37.8		3.3353	6.0E-05	148.7	0.3
9479	Calanques	43.2015	5.4326	0	38.2		3.3513	6.5E-05	147.2	0.3
9480	Calanques	43.2033	5.4448	0	38.4		3.2891	6.9E-05	147.3	0.4
9481	Calanques	43.2011	5.4448	0	38.3		3.3463	6.6E-05	146.8	0.3
9482	Calanques	43.1989	5.4448	0	38.3		3.1637	5.3E-05	149.9	0.3
9483	Calanques	43.2093	5.4565	0	38.1		3.1458	5.4E-05	149.7	0.3
9484	Calanques	43.2079	5.4565	0	38.2		3.3040	5.9E-05	148.0	0.3
9485	Calanques	43.2057	5.4593	0	38.2		3.3437	5.8E-05	147.9	0.3
9486	Calanques	43.2017	5.4600	0	38.3		3.3668	6.2E-05	148.4	0.3
9487	Calanques	43.1976	5.4600	0	38.3		3.3292	6.0E-05	147.4	0.3
9488	Calanques	43.2040	5.4820	0	38.3		3.2263	6.5E-05	149.1	0.3
9489	Calanques	43.2016	5.4813	0	38.3		3.4137	5.0E-05	149.9	0.2
9490	Calanques	43.1983	5.4813	0	38.2		3.3197	6.3E-05	148.4	0.3
9491	Calanques	43.1959	5.4999	0	38.2		3.3254	6.5E-05	149.8	0.3
9492	Calanques	43.1936	5.4999	0	38.3		3.2454	5.8E-05	147.9	0.3
9493	Calanques	43.2035	5.5131	0	37.2		3.2544	5.8E-05	152.6	0.3
9494	Calanques	43.2019	5.5150	0	37.0		3.0803	5.9E-05	158.5	0.4
9495	Calanques	43.1987	5.5152	0	37.4		3.2744	7.2E-05	151.0	0.4
9496	Calanques	43.1951	5.5152	0	38.3		3.3192	6.5E-05	149.1	0.4
9497	Calanques	43.1885	5.5152	0	38.3		3.2384	6.0E-05	149.2	0.3
9498	Calanques	43.1816	5.5152	0	38.3		3.3130	4.9E-05	149.1	0.3
9499	Calanques	43.2057	5.5235	0	38.2		3.3483	6.2E-05	148.3	0.3
9500	Calanques	43.2033	5.5235	0	38.3		3.0457	5.2E-05	149.5	0.3
9501	Calanques	43.2118	5.5333	0	28.3		3.0538	5.5E-05	149.8	0.3
9502	Calanques	43.2071	5.5333	0	38.0		3.2389	4.7E-05	149.2	0.3
9503	Calanques	43.2024	5.5333	0	37.9		3.2906	5.6E-05	149.1	0.3
9467	Calanques	43.2097	5.3867	0	38.3		3.3167	9.1E-05	148.0	0.4
9468	Calanques	43.2076	5.3867	0	38.2		3.4600	1.1E-04	148.0	0.5
9469	Calanques	43.2049	5.3867	0	38.2		2.6830	7.1E-05	147.7	0.5
9470	Calanques	43.2106	5.4030	0	36.5		3.2566	1.5E-04	151.1	0.8
9471	Calanques	43.2074	5.4030	0	38.2		3.3050	4.8E-05	147.3	0.3
9472	Calanques	43.2039	5.4030	0	38.2		3.1171	4.6E-05	147.2	0.3
9505	Calanques	43.2084	5.4319	0	38.0		3.2389	4.9E-05	147.2	0.3
9506	Calanques	43.2119	5.4547	0	26.3	16.3	2.2899	3.0E-05	267.3	0.3
9507	Calanques	43.2119	5.4546	0	34.7	12.7	2.8451	3.9E-05	192.2	0.3
9509	Calanques	43.2117	5.4553	0	37.5	14.0	2.7216	5.4E-05	148.8	0.3
9510	Calanques	43.2113	5.4551	0	38.1	13.4	3.3844	4.8E-05	147.7	0.3
9511	Calanques	43.2103	5.4555	0	37.7	13.4	3.3480	4.8E-05	149.7	0.3
9512	Calanques	43.2040	5.5131	0	34.5	14.2	3.1437	4.5E-05	157.3	0.3
9513	Calanques	43.2053	5.5134	0	30.0		2.4389	3.4E-05	178.7	0.3
9515	Calanques	43.2111	5.5212	0	14.0	16.4	1.2573	2.1E-05	331.8	0.4
9516	Calanques	43.2101	5.5206	0	18.6	15.6	1.7245	2.4E-05	256.1	0.4
9517	Calanques	43.2095	5.5197	0	19.7	15.7	1.4141	2.0E-05	243.1	0.3
9518	Calanques	43.2083	5.5184	0	24.8	15.0	1.6956	2.6E-05	205.2	0.3
9519	Calanques	43.2136	5.5329	0	7.5	16.1	1.0743	1.9E-05	210.0	0.5
9521	Calanques	43.2136	5.5330	0	22.1	14.8	1.8257	3.3E-05	165.9	0.4
9522	Calanques	43.2048	5.5144	0	30.8	15.6	2.3381	3.3E-05	192.1	0.3
9523	Canet	42.6689	3.0347	0	36.7	16.4	3.2506	5.4E-05	147.5	0.3
9526	Leucate	42.8925	3.0530	0	36.7	21.6	2.8384	3.4E-05	160.9	0.3

A.3 Gulf of Lions: spring samples and groundwater end-members

Lab Number	**Source**	**Latitude**	**Longitude**	**Depth** m	**Salinity** PSU	**Temperature** °C	^{238}**U** μg l^{-1}	2σ	δ^{234}**U** ‰	2σ
9504	SGD-1	43.2130	5.4032	0	21.7		2.0373	3.0E-05	165.5	0.3
9508	SGD-2	43.2118	5.4553	0	17.8	16.2	1.6678	2.9E-05	337.2	0.4
9514	SGD-3	43.2111	5.5211	0	9.3	16.8	0.9957	1.8E-05	418.5	0.6
9520	SGD-4	43.2140	5.5338	0	6.9	16.9	0.9703	1.8E-05	220.0	0.5
9528	La Palme	42.9787	3.0114	0	8.3		0.8405	1.3E-05	1173.2	0.7
9529	La Palme	42.9787	3.0114	0	8.3		0.8171	1.3E-05	1169.6	0.6
9530	Estramar	42.8593	2.9584	0	3.7		0.6215	1.0E-05	959.5	0.5

A.4 Atlantic Ocean

Lab Number	Station	Latitude	Longitude	Depth	Salinity	Temperature	^{238}U	2σ	δ^{234}U	2σ
				m	PSU	°C	μg l^{-1}		‰	
8956	UFO-1	37.0733	-19.7858	1287	35.61	7.90	3.2307	6.9E-05	147.0	0.3
8958	UFO-1	37.0733	-19.7858	1089	35.81	9.46	3.2705	6.5E-05	146.7	0.3
8962	UFO-1	37.0733	-19.7858	744	35.65	10.58	3.2621	6.8E-05	145.1	0.3
8995	UFO-2	36.7332	-16.0205	3031	34.94	2.86	3.2119	5.9E-05	146.8	0.4
8996	UFO-2	36.7332	-16.0205	2500	34.99	3.30	3.2403	5.7E-05	147.0	0.3
8997	UFO-2	36.7332	-16.0205	2500	34.99	3.30	3.3669	5.5E-05	146.9	0.3
8998	UFO-2	36.7332	-16.0205	2298	35.04	3.74	3.2935	5.7E-05	146.7	0.3
8999	UFO-2	36.7332	-16.0205	1898	35.14	4.62	3.2120	5.4E-05	146.9	0.3
9000	UFO-2	36.7332	-16.0205	1584	35.35	6.03	3.3392	6.0E-05	146.8	0.3
9001	UFO-2	36.7332	-16.0205	1471	35.56	7.19	3.3069	5.5E-05	147.2	0.3
9002	UFO-2	36.7332	-16.0205	1303	35.85	8.94	3.2653	6.4E-05	147.2	0.4
9003	UFO-2	36.7332	-16.0205	1158	36.09	10.41	3.2672	7.1E-05	146.7	0.4
9004	UFO-2	36.7332	-16.0205	1089	36.08	10.51	3.4823	6.7E-05	147.1	0.3
9005	UFO-2	36.7332	-16.0205	918	35.88	10.38	3.4448	6.4E-05	146.7	0.4
9006	UFO-2	36.7332	-16.0205	918	35.88	10.38	3.2805	6.7E-05	147.1	0.4
9009	UFO-2	36.7332	-16.0205	715	35.73	10.91	3.2709	6.0E-05	147.1	0.4
9011	UFO-2	36.7332	-16.0205	679	35.87	11.63	3.3109	5.4E-05	146.9	0.4
9012	UFO-2	36.7332	-16.0205	498	35.67	11.85	3.2464	6.4E-05	146.4	0.3
9013	UFO-2	36.7332	-16.0205	103	36.11	16.31	3.3943	7.1E-05	145.9	0.3
9014	UFO-2	36.7332	-16.0205	36	36.51	22.13	3.3649	6.4E-05	146.6	0.3
10427	MR1	53.9667	-14.2163	6	35.40	13.41	3.3069	7.2E-05	147.1	0.4
10428	MR1	53.9667	-14.2163	52	35.42	11.41	3.4090	6.9E-05	145.5	0.4
10429	MR1	53.9667	-14.2163	102	35.38	11.00	3.4267	7.2E-05	145.5	0.4
10430	MR1	53.9667	-14.2163	330	35.38	10.42	3.4221	7.0E-05	145.1	0.4
10431	MR1	53.9667	-14.2163	563	35.34	9.94	3.3957	7.6E-05	144.8	0.4
10432	MR1	53.9667	-14.2163	1000	35.26	8.00	3.4156	7.6E-05	144.3	0.4
10433	MR2	55.4168	-15.2992	14	35.29	12.27	3.3969	8.3E-05	145.4	0.4
10434	MR2	55.4168	-15.2992	200	35.29	9.76	3.4105	6.6E-05	145.8	0.4
10435	MR2	55.4168	-15.2992	400	35.30	9.50	3.4083	1.2E-04	145.1	0.4
10436	MR2	55.4168	-15.2992	635	35.27	8.64	3.1980	6.5E-05	144.7	0.5
10437	MR2	55.4168	-15.2992	998	35.21	6.70	3.3722	6.5E-05	145.8	0.3
10439	MR2	55.4168	-15.2992	103	35.27	10.01	3.4133	6.7E-05	145.6	0.4
10440	MR3	55.9162	-11.9982	15	35.30	13.04	3.3985	7.8E-05	146.0	0.4
10441	MR3	55.9162	-11.9982	77	35.33	10.07	3.4102	6.9E-05	145.7	0.4
10442	MR3	55.9162	-11.9982	201	35.33	9.82	3.4071	5.7E-05	146.0	0.4
10443	MR3	55.9162	-11.9982	400	35.32	9.64	3.3991	7.8E-05	145.7	0.4
10444	MR3	55.9162	-11.9982	700	35.32	9.22	3.4067	6.6E-05	146.2	0.5
10445	MR6	59.7167	-6.4837	10	35.23	12.04	3.4058	7.1E-05	145.7	0.5
10446	MR6	59.7167	-6.4837	102	35.32	9.72	3.4065	8.4E-05	145.4	0.4
10447	MR6	59.7167	-6.4837	196	35.32	9.64	3.4442	7.7E-05	145.9	0.5
10448	MR6	59.7167	-6.4837	276	35.32	9.55	3.4120	6.3E-05	145.8	0.3
10449	MR7	59.6998	-6.9157	39	35.27	11.77	3.4491	6.2E-05	145.6	0.5
10450	MR7	59.6998	-6.9157	202	35.32	9.54	3.4093	7.8E-05	146.2	0.4
10451	MR7	59.6998	-6.9157	400	35.31	9.20	3.4318	6.7E-05	146.2	0.4
10452	MR7	59.6998	-6.9157	600	35.29	8.92	3.4484	7.2E-05	145.7	0.4
10453	MR7	59.6998	-6.9157	950	35.24	7.96	3.3734	6.0E-05	146.0	0.3

A.5 Gulf of Cadiz

Lab Number	Station	Latitude	Longitude	Depth m	Salinity PSU	Temperature °C	^{238}U $\mu g\ l^{-1}$	2σ	$\delta^{234}U$ ‰	2σ
8412	Geob18132-1	35.33236	-7.04238	978	35.82	10.03	3.2698	5.0E-05	147.3	0.3
8413	Geob18132-1	35.33240	-7.04238	949	35.81	10.02	3.2561	5.2E-05	147.3	0.2
8414	Geob18132-1	35.33242	-7.04238	899	35.77	9.98	3.2407	7.3E-05	147.1	0.4
8415	Geob18132-1	35.33240	-7.04240	799	35.73	10.32	3.2439	7.0E-05	147.6	0.4
8417	Geob18132-1	35.33242	-7.04238	680	35.72	10.93	3.2458	5.3E-05	147.2	0.3
8418	Geob18132-1	35.33242	-7.04242	550	35.63	11.38	3.2377	5.9E-05	147.2	0.3
8419	Geob18132-1	35.33240	-7.04238	400	35.71	12.36	3.2702	7.6E-05	146.9	0.4
8420	Geob18132-1	35.33242	-7.04240	251	35.91	13.72	3.3120	7.1E-05	147.2	0.4
8421	Geob18132-1	35.33238	-7.04232	161	36.32	15.75	3.3011	5.7E-05	147.0	0.3
8422	Geob18132-1	35.33238	-7.04240	92	36.25	15.70	3.3254	5.3E-05	147.2	0.3
8423	Geob18132-1	35.33240	-7.04240	22	36.41	16.49	3.2706	7.5E-05	147.0	0.4
8431	Geob18132-1	35.33236	-7.04238	978	35.82	10.03	3.2856	1.1E-04	147.1	0.6
8432	Geob18132-1	35.33242	-7.04238	899	35.77	9.98	3.2979	8.3E-05	146.8	0.4
8433	Geob18132-1	35.33242	-7.04238	680	35.72	10.93	3.2738	1.1E-04	146.9	0.7
8434	Geob18132-1	35.33242	-7.04240	251	35.91	13.72	3.3316	7.6E-05	146.9	0.4
8578	Geob18136-1	35.10352	-7.13208	800	35.77	10.40	3.2325	4.4E-05	147.0	0.3
8579	Geob18136-1	35.10352	-7.13210	700	35.77	10.97	3.2119	4.0E-05	147.2	0.3
8580	Geob18136-1	35.10353	-7.13208	501	35.64	11.76	3.2245	4.4E-05	147.1	0.3
8581	Geob18136-1	35.10352	-7.13208	202	36.15	15.13	3.2513	4.2E-05	147.1	0.4
8582	Geob18136-1	35.10352	-7.13208	23	36.41	16.44	3.2838	4.3E-05	147.0	0.3
8583	Geob18136-1	35.10352	-7.13207	401	35.74	12.62	3.2194	3.8E-05	147.0	0.3
8586	Geob18152-1	35.41664	-7.00029	499	35.63	11.47	3.2102	4.8E-05	147.1	0.4
8587	Geob18152-1	35.41673	-7.00040	50	36.26	15.56	3.2729	4.6E-05	147.4	0.3
8588	Geob18154-1	35.24978	-7.08370	888	35.71	9.97	3.2333	4.8E-05	147.2	0.3
8589	Geob18154-1	35.24974	-7.08380	698	35.65	10.37	3.2234	5.1E-05	147.0	0.3
8590	Geob18154-1	35.24978	-7.08371	499	35.64	11.23	3.2249	5.0E-05	147.1	0.3
8591	Geob18154-1	35.24980	-7.08375	50	36.34	15.98	3.2869	4.7E-05	146.8	0.3

A.6 Amazon

Lab Number	Cruise	Latitude	Longitude	Depth	Salinity	Temperature	^{238}U	2σ	$\delta^{234}U$	2σ
				m	PSU	°C	$\mu g\ l^{-1}$		‰	
9828	M147	3.8995	-50.5018	40	36.19	25.89	3.2531	6.3E-05	146.4	0.3
9829	M147	1.0253	-47.0673	12	35.83	28.18	3.2601	5.9E-05	146.3	0.3
9830	M147	-0.5969	-46.9044	3	28.07	28.73	2.5469	5.0E-05	146.1	0.3
9831	M147	1.3609	-47.3844	30	35.90	27.63	3.1275	6.0E-05	146.4	0.3
9832	M147	1.0253	-47.0674	3	35.83	28.17	3.0954	6.4E-05	146.5	0.3
9833	M147	1.5942	-49.0030	6	13.50	27.98	0.7384	2.0E-05	155.4	0.7
9834	M147	3.7686	-50.8001	3	12.98	27.01	1.0947	2.4E-05	150.2	0.6
9835	M147	0.9517	-49.6476	3	0.19	28.37	0.0428	8.5E-06	246.3	10.5
9836	M147	3.9568	-47.6041	805	34.56	5.34	3.0219	6.1E-05	146.2	0.3
9837	M147	0.0286	-48.1934	2	2.74	26.66	0.1190	1.0E-05	170.0	3.7
9838	M147	6.5824	-49.7809	750	34.57	5.52	3.0355	6.8E-05	146.0	0.4
9839	M147	3.0997	-50.5020	3	10.59	27.32	0.7078	2.0E-05	152.2	0.7
9840	M147	3.9320	-47.6090	4	35.98	27.92	3.2366	7.2E-05	146.0	0.3
9842	M147	1.0252	-47.0673	35	35.84	28.18	3.2082	6.8E-05	146.2	0.3
9843	M147	-0.5442	-46.7695	3	30.79	28.75	2.7527	5.3E-05	146.3	0.3
9844	M147	1.1656	-48.3352	12	35.59	28.25	3.2133	6.4E-05	146.4	0.3
9846	M147	3.5501	-50.1192	3	21.05	27.79	1.9509	3.5E-05	148.2	0.4
9847	M147	-0.1743	-47.9234	20	24.10	28.68	2.0766	4.3E-05	147.6	0.4
9848	M147	-0.4826	-46.9007	3	30.84	29.22	2.7246	4.8E-05	146.1	0.3
9849	M147	1.4511	-49.3174	3	1.86	27.88	0.0410	1.3E-04		
9850	M147	0.0546	-48.7075	2	0.03	28.29	0.0723	9.0E-06	222.1	8.6
9851	M147	1.9440	-47.7888	3	26.78	28.36	2.3978	5.4E-05	148.2	0.4
9852	M147	0.4003	-47.4725	10	27.05	28.10	2.4320	6.1E-05	147.3	0.4
9853	M147	2.0855	-47.6625	72	36.12	25.77	3.2031	6.7E-05	146.1	0.3
9854	M147	1.7369	-47.9731	4	21.49	28.15	1.8634	4.2E-05	147.8	0.5
9855	M147	2.6522	-50.1086	2	13.36	27.09	0.8689	2.4E-05	151.3	0.8
9856	M147	1.9146	-46.4455	800	34.51	5.22	3.0666	7.2E-05	146.3	0.4
9857	M147	1.5942	-49.0030	6	13.50	27.98	0.7447	2.2E-05	156.0	0.9
9858	M147	3.5499	-50.1183	58	36.23	25.33	3.2240	6.5E-05	146.5	0.3
9974	M147	1.4379	-49.2975	3	7.17	27.93	0.1408	1.1E-05	169.8	4.3
9975	M147	1.6353	-48.5970	7	26.25	28.22	2.5183	4.9E-05	147.9	0.4
9978	M147	1.6353	-48.5971	8	27.35	28.21	2.6457	5.9E-05	148.2	0.4
9979	M147	3.2692	-48.8745	4	35.69	28.25	3.0813	6.1E-05	146.4	0.4
9980	M147	4.0036	-48.3082	3	35.96	28.18	3.1155	6.2E-05	146.2	0.3
9983	M147	0.4005	-47.4726	25	31.86	28.63	2.5627	4.9E-05	146.5	0.4
9984	M147	-0.1743	-47.9234	0			3.0987	6.9E-05	146.2	0.3
9985	M147	1.2667	-48.2784	3	7.31	28.08	0.5231	1.9E-05	155.2	1.4
9986	M147	2.3241	-47.4714	806	34.57	5.18	3.0206	6.3E-05	146.3	0.3
9988	M147	2.0861	-47.6637	3	33.10	28.08	2.8898	5.3E-05	146.3	0.3
9991	M147	0.9808	-47.7185	3	25.30	29.26	2.1673	4.7E-05	146.7	0.4
9993	M147	2.0518	-48.8320	3	3.54	27.83	0.4536	1.7E-05	156.7	1.4
9994	M147	1.4795	-48.1485	3	9.41	28.05	0.8817	2.1E-05	151.9	0.8
9995	M147	1.4394	-49.2867	3	5.10	27.86	0.0750	9.3E-06	186.2	8.1
9996	M147	1.4377	-49.2808	3	3.32	27.57	0.0456	1.3E-05	199.4	12.1
10044	M147	0.5678	-47.9981	3	6.86	28.20	1.2061	3.3E-05	148.7	0.7
10045	M147	1.4453	-49.3331	3	0.80	28.02	0.0529	1.3E-05	205.5	12.1
10046	M147	1.4624	-49.2561	3	12.93	27.99	0.9163	1.9E-05	154.9	0.7
10047	M147	2.3017	-48.5858	4	16.52	27.68	1.4465	3.4E-05	150.1	0.5
10048	M147	2.4258	-48.5049	3	22.34	27.31	1.9820	4.0E-05	148.4	0.4
10049	M147	2.5490	-48.4406	3	28.79	27.67	2.5105	4.9E-05		
10050	M147	2.8600	-48.2633	5	35.85	28.17	3.1286	6.9E-05	146.0	0.3
10051	M147	2.3290	-47.4825	4	36.05	27.87	3.0897	5.8E-05	146.6	0.3
10052	M147	0.0179	-48.4185	2	1.10	27.88	0.0712	1.8E-05	179.4	8.7
10053	M147	1.6514	-48.0400	41	35.84	27.74	3.1730	6.4E-05	145.7	0.3
10054	M147	1.5677	-48.0941	3	12.39	27.98	1.1579	3.2E-05	150.5	0.7
10055	M147	1.3613	-47.3847	3	35.61	28.25	3.1331	6.0E-05	146.0	0.3
10056	M147	-0.0658	-48.6901	3	0.03	28.27	0.0544	8.4E-06	247.6	11.4
10057	M147	0.0201	-48.4170	3	0.60	27.77	0.0453	9.9E-06	199.5	13.2
10058	M147	1.1655	-48.3355	3	5.90	27.66	0.5677	1.7E-05	151.7	1.0

B Additional figures

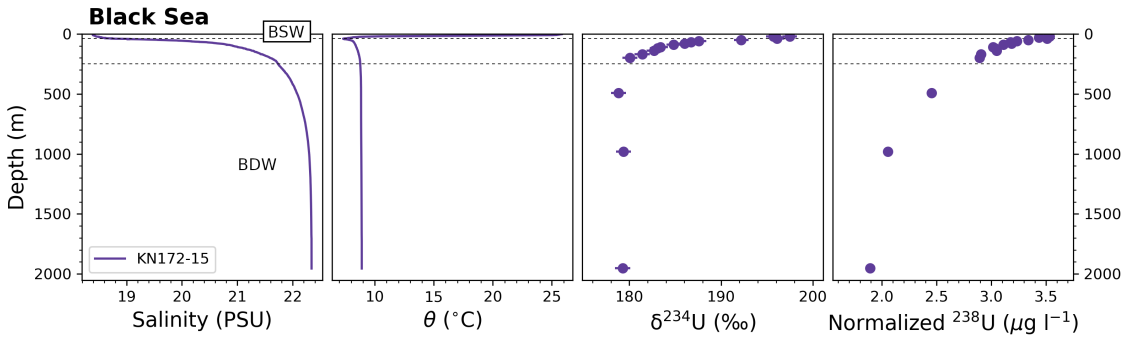

Figure B.1: δ^{234}U profile from the Black Sea. Concentrations are normalized to 35 PSU to show depletion of U with depth over the salinity gradient. Water masses shown are Black Sea surface water (BSW) and Black Sea deep water (BDW). All δ^{234}U errors are 2σ

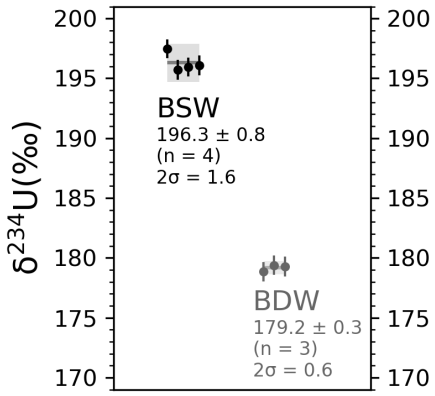

Figure B.2: δ^{234}U fingerprints of Black Sea water masses. Shaded regions for each water mass represent the 2σ external reproducibility, while the errors listed with each fingerprint value is the $2\sigma_m$ measurement error based on n measurements.

C Lists

C.1 List of Abbreviations

AgDW Aegean deep water

AMOC Atlantic meridional overturning circulation

AUR IUP Heidelberg Atlantic uranium record

AW Atlantic water

BDW Black Sea deep water

BSW Black Sea surface water

CTD Device for measuring the properties of seawater as well as collecting samples. Name stems from 'conductivity, temperature, and depth'

CWC Cold water coral

DWBC Deep western boundary current

EMDW Eastern Mediterranean deep water

ENACW Eastern North Atlantic central water

ESA Electrostatic analyzer

GoL Gulf of Lions

ICP Inductively-coupled plasma

LGM Last glacial maximum

LIW Levantine intermediate water

MAW Modified Atlantic water

MC-ICP-MS Multicollector inductively-coupled plasma mass spectrometer (or spectrometry)

MDW Mediterranean deep water

MOW Mediterranean overflow water

MS Magnetic sector

NADW North Atlantic deep water

NBC North Brazil current

NECC North equatorial counter current

NW Northwest

PSU Practical salinity unit

SE Southeast

SGD Submarine groundwater discharge

SGD+R Submarine groundwater discharge plus river discharge

SoG Strait of Gibraltar

THC Thermohaline circulation

TIMS Thermal ionization mass spectrometer (or spectrometry)

WMDW Western Mediterranean deep water

C.2 List of Figures

2.1 The overturning circulation of the oceans. Red arrows indicate surface currents. Blue arrows are deep-sea currents. The purple circles are areas of deep-water production. Figure from Hansen et al. (2004). . . 8

2.2 A schematic of the ocean U budget for the Holocene from Dunk et al. (2002). Inputs and removals are shown in terms of Mmol/yr, while the ocean inventory is in Mmol. 10

2.3 The ^{238}U decay chain, also known as the *uranium series*. The two uranium isotopes are highlighted in purple. The chain begins with primordial ^{238}U and ends with stable ^{206}Pb. 13

2.4 A conceptual view of the α-recoil effect, which is responsible for the elevated (i.e. above unity) ^{234}U content of groundwater, rivers and the ocean. 15

2.5 A model of the oceanic U system according to Chen et al. (1986). Inputs are primarily to the upper ocean, while removal occurs primarily in the deep-sea. 17

3.1 The CTD setup aboard the RV *Meteor*, as used to collect samples from the Amazon region. The 24 Niskin bottles are open, ready for deployment. The CTD unit and sensors can be seen at the bottom. In this particular instance the CTD unit is a Seabird "SBE 9 plus". . 20

3.2 The basic layout of the Thermo Fisher Neptune *plus* used for measuring δ^{234}U in this thesis. Samples were introduced to the ICP module using a Cetac Aridus II rather than the built-in nebulizer. Figure adapted from ThermoFisher (2009). 22

3.3 A cross section of the plasma torch. Figure adapted from ThermoFisher (2009). 23

3.4 Mass dispersion in the magnetic sector of the Neptune. Figure adapted from ThermoFisher (2009). 24

3.5 (left) The multicollector array, with eight mobile Faraday cups and one fixed 'center' cup. (right) A zoomed in view of a Faraday cup with the cover removed. Figures adapted from ThermoFisher (2009). 25

4.1 The major features of the Mediterranean Overturning Circulation. Atlantic Water (AW, also known as Modified Atlantic Water (MAW)) flows in through the SoG and across the basin where (due to evaporation) loses buoyancy and becomes Levantine Intermeditate Water (LIW). Western Mediterranean Deep Water (WMDW) and Eastern Mediterranean Deep Water (EMDW) are formed in the GoL and Adriatic Sea respectively. Figure adapted from Tsimplis et al. (2006). . . . 29

4.2 Sampling locations in the Mediterranean and nearby Atlantic. The top map inserts show a closer view of coastal sampling along the Western French Mediterranean Coast (left) and along the Calanques de Marseille (right). The bottom enlargement shows the closely spaced stations in the Gulf of Cadiz and Alboran Sea. 'Spring' here refers only to terrestrial springs, rather than SGD. Calanques samples were largely taken according to known SGD locations (Figure 4.3). 31

4.3 The five locations of strong SGD influence found by Bejannin et al. (2017). Aerial thermal imaging was used to find influence from cold SGD (a. Calanque of Cortiou, b. Calanque of Sormiou, c. Calanque of Sugiton, d. Calanque of Port Miou and e. Cassis). White arrows indicate known submarine springs according to Gilli (2001). Note that, in addition to SGD, Calanque of Cortiou (a) is influenced by ouflow from the main sewage plant in Marseille (warm signal). Figure taken from Bejannin et al. (2017). 32

4.4 (Top) δ^{234}U results from all coastal samples (springs, hand pump stations). The hand pump stations from the Western GoL (Leucate and Canet) are colored blue to differentiate them from the Calanques de Marseille stations (yellow). The inset figure shows a zoomed in view of the upper right region of the main plot. The shaded vertical section represents the oceanic δ^{234}U from Andersen et al. (2010) of 146.8 ± 0.1‰. All errors are 2σ, although most are smaller than the plot symbols. (Bottom) Salinity vs. U concentration (^{238}U) for coastal samples. 33

4.5 δ^{234}U results from CTD stations in the Mediterranean Sea and nearby Atlantic, arranged by region. The left two sections show salinity (in practical salinity units (PSU)) and potential temperature (θ) from CTD casts during sample collection. Major water masses are labeled as follows: Eastern North Atlantic central water (ENACW), Mediterranean overflow water (MOW), North Atlantic deep water (NADW), modified Atlantic water (MAW), Western Mediterranean deep water (WMDW), Levantine intermediate water (LIW), Eastern Mediterranean deep water (EMDW), Aegean Deep Water (AgDW), and Black Sea surface water (BSW). All δ^{234}U errors are 2σ. 34

4.6 Sectional view of CTD-station δ^{234}U results across the Atlantic and Mediterranean, with major water masses labeled. The lower map shows the sectional track. Created using Ocean Data View (Schlitzer (2018)). 37

4.7 δ^{234}U fingerprints for various water masses across the Atlantic and Mediterranean. ENACW and MOW are both split geographically, into one open-ocean fingerprint and one fingerprint from the Gulf of Cadiz (GoC). Similarly, upwelled WMDW in the Alboran Sea has been fingerprinted separately. Shaded regions for each water mass represent the 2σ external reproducibility, while the errors listed with each fingerprint value is the $2\sigma_m$ measurement error based on n measurements. 38

4.8 Calanques de Marseille results arranged geographically. Zooms of the two areas enclosed by black rectangles are seen in the two upper figures. Red numbers refer to the four SGD sources of δ^{234}U found in the study. 41

4.9 The results from Figure 4.8 re-scaled to more easily see differences in seawater samples. The signal from SGD sources 3 and 4 can be seen to propagate into nearby seawater samples, with nearly all eastern samples having δ^{234}U values of over 149‰. The fifth SGD source identified in Bejannin et al. (2017) (X) also shows no consistent SGD signal at this scale. 43

4.10 Keeling plot (δ^{234}U against $1/^{238}$U) of samples from Calanques de Marseille (inverted triangles), with spring samples from western GoL (diamonds) for reference. Calanques samples are colored according to which of the four SGD sources identified in Figure 4.8 they are located closest to. Lines with matching colors denote the linear regression of all samples from within each grouping. r^2 values for each line are found in the legend. 45

4.11 Schematic view of the box model for estimating the U concentration and δ^{234}U of the combined river and SGD input to the Mediterranean Basin. Inputs are represented in terms of their volumetric flow of water, uranium concentration (^{238}U) and δ^{234}U. ^{238}U decay to ^{234}U excludes the short lived intermediate isotopes of ^{234}Th and ^{234}Pa. SGD inflow is from Rodellas et al. (2015), with all other water fluxes from Jordà et al. (2017). Atlantic ^{238}U and δ^{234}U are from Chen et al. (1986) and Andersen et al. (2010) respectively. Black Sea ^{238}U and δ^{234}U are from Border et al. (2020). Mediterranean ^{238}U and δ^{234}U are the values for MDW from Section 4.4.1. 47

4.12 Modeled input (black curve) from SGD and rivers into the Mediterranean Sea according to Equation 4.5 in terms of U concentration (^{238}U) and δ^{234}U. The top axis is the modeled Mediterranean U concentration, which is related to the input U concentration through Equation 4.1. The shaded region is the U concentration measured in EMDW and WMDW in this thesis. The oceanic δ^{234}U value of 146.8 ± 0.1‰ as determined by Andersen et al. (2010) is represented by the dashed line. Rhône River U concentration and δ^{234}U are from Ollivier et al. (2011) and Zebracki et al. (2017) respectively. The world rivers data point is the average value of U concentration and δ^{234}U from world rivers as compiled by Chabaux et al. (2003). 50

5.1 A view of the entire Amazon catchment basin. Adapted from Calhman and da Hora (2017). 54

5.2 The Amazon Estuary region with an approximation of the Amazon Plume in red. The incoming North Brazil Current (NBC) is in dark blue. Lighter blue denotes surface currents heavily influenced by the plume: the northwest continuation of the NBC and the North Equatorial Counter Current (NECC). (Geyer et al., 1996; Johns et al., 1998; Bourles et al., 1999). 55

5.3 Locations of samples taken from the Amazon Estuary, colored according to salinity. The left-hand subplots show samples taken from shallower than 5 m depth (top) and those from over 5 m depth (bot). 57

5.4 (Top) δ^{234}U results from all Amazon Estuary samples. The inset figure shows a zoomed in view of high salinity samples. The shaded horizontal section represents the oceanic δ^{234}U from Andersen et al. (2010) of 146.8 ± 0.1‰. All errors are 2σ, although most are smaller than the plot symbols. (Bottom) Salinity vs. U concentration (^{238}U) for Amazon Estuary samples. 59

5.5 Amazon results shown geographically. (left) U concentration, (right) δ^{234}U. The white lines show the boundary between samples from the northwest (NW) or southeast (SE) of the Amazon Estuary, a designation which will be used to look into regional differences in U behavior. 61

5.6 (Top) ^{238}U results from Amazon Estuary samples colored according to whether they came from the NW or SE sections. The black line represents hypothetical conservative mixing across the salinity gradient between Amazon and Atlantic end-members from Section 5.4.1. (Bottom) The U content of each sample relative to conservative mixing (ΔU), i.e. -100% represents all U being removed, while +100% represents double the expected U. 62

5.7 Geographical view of ΔU results. The main map (right) shows all samples, while left-hand maps only show samples from surface (<5m, top) or bottom (>5m bottom). Samples are split between NW and SE as in Figure 5.5. Circled areas designate the regions with strong U-sink behavior. Stars are samples with $\Delta U > +10\%$, indicating local U-sources. 64

5.8 (Top) δ^{234}U results from Amazon Estuary samples colored according to whether they came from the NW or SE sections. The black curve represents hypothetical conservative mixing across the salinity gradient between Amazon and Atlantic end-members established in Section 5.4.1. (Bottom) The offset in δ^{234}U between each sample and the conservative mixing curve. 66

5.9 Comparison between ΔU and δ^{234}U offset (as seen in Figures 5.6 and 5.8 respectively). Samples with negative ΔU tend to show elevated δ^{234}U, while positive ΔU corresponds with lowered δ^{234}U. 68

5.10 Geographical view of $\Delta\delta^{234}$U (as defined by Equation 5.4) relative to conservative mixing between Amazon and Atlantic. Main map shows all samples, while left-hand maps only show samples from surface (<5m, top) or bottom (>5m bottom). Samples are split between NW and SE as in Figure 5.5. Circled areas designate the regions with strong U-sink behavior, as defined in Figure 5.7. Stars are samples with $\Delta U > 10\%$, indicating local U-sources. 69

5.11 The ΔU (top) and $\Delta\delta^{234}$U (bottom) results from the high-salinity (>20 PSU) samples. Samples are split between NW and SE as in Figure 5.5. NBC stands for North Brazil Current. 72

5.12 A map of the high-salinity (>20 PSU) ΔU results. The location of the Pará Mangroves are labeled. The three samples located just off the coast near the mangroves are labeled as "Mangroves" in Figure 5.11. 73

5.13 A map of the high-salinity (>20 PSU) $\Delta\delta^{234}$U results. 74

5.14 Comparison of δ^{234}U from oceanic samples within the mixed-layer (black) and below the mixed-layer (gray). Samples are split as shown in Figure 5.11. 76

6.1 A schematic view of the Atlantic Meridional Overturning Circulation (AMOC). Warm water is transported northwards where it sinks and returns southwards as North Atlantic Deep Water (NADW). This deep water formation takes place in both the Arctic Ocean and Labrador Sea. Figure adapted from Ruddiman (2001). 78

6.2 Location of samples from the Atlantic. Eastern North Atlantic samples were previously discussed in Chapter 4 (Stations UFO-1 and UFO-2). Western Equatorial Atlantic samples are the 'oceanic' samples (salinity >34 PSU) discussed in Chapter 5. Circles are from this work. Upward pointing green triangles are water samples from Andersen et al. (2010). Downward pointing red triangles represent modern carbonate (coral and *Halimeda*) samples measured by Robinson et al. (2004a). 80
6.3 δ^{234}U results of all samples from the open Atlantic Ocean. Locations are shown in Figure 6.2. Circles are from this work. Upward pointing green triangles are water samples from Andersen et al. (2010). Downward pointing red triangles are from modern carbonate (coral and *Halimeda*) samples measured by Robinson et al. (2004a). 81
6.4 Difference in δ^{234}U in the deep and upper(thermocline) Atlantic. Samples from the Eastern North Atlantic from within the MOW (as discussed in Section 4.4.1) are excluded. 83
6.5 Atlantic δ^{234}U over the last 60 kyr. Data is from the IUP Heidelberg Atlantic Uranium Record (AUR), a collection of previously published δ^{234}U values based on the U-series dating of cold-water corals (sources are in text). 87

B.1 δ^{234}U profile from the Black Sea. Concentrations are normalized to 35 PSU to show depletion of U with depth over the salinity gradient. Water masses shown are Black Sea surface water (BSW) and Black Sea deep water (BDW). All δ^{234}U errors are 2σ 102
B.2 δ^{234}U fingerprints of Black Sea water masses. Shaded regions for each water mass represent the 2σ external reproducibility, while the errors listed with each fingerprint value is the $2\sigma_m$ measurement error based on n measurements. 102

C.3 List of Tables

3.1 The typical setup for δ^{234}U measurement with the Thermo Fisher Neptune *Plus*. Typical intensities are in terms of what the current would be when measuring with the standard $10^{11}\Omega$ resistor. 26

D Bibliography

Andersen, M.B., Stirling, C.H., Porcelli, D., Halliday, A.N., Andersson, P.S., and Baskaran, M. The tracing of riverine U in Arctic seawater with very precise 234U/238U measurements. *Earth Planet. Sci. Lett.*, 259(1-2):171–185, 2007. doi: 10.1016/j.epsl.2007.04.051

Andersen, M.B., Stirling, C.H., and Weyer, S. Uranium Isotope Fractionation. *Rev. Mineral. Geochemistry*, 82(1):799–850, 2017. doi:10.2138/rmg.2017.82.19

Andersen, M.B., Stirling, C.H., Zimmermann, B., and Halliday, A.N. Precise determination of the open ocean 234 U/238 U composition. *Geochemistry, Geophys. Geosystems*, 11(12), 2010. doi:10.1029/2010GC003318

Andrews, J.N. and Kay, R.L.F. 234U/238U activity ratios of dissolved uranium in groundwaters from a jurassic limestone aquifer in England. *Earth Planet. Sci. Lett.*, 57(1):139–151, 1982. doi:10.1016/0012-821X(82)90180-7

Arps, J. Towards ϵ-Precision of U-series Age Determinations of Secondary Carbonates. Phd thesis, Universität Heidelberg, 2017

Barnes, C.E. and Cochran, J.K. Uranium geochemistry in estuarine sediments: Controls on removal and release processes. *Geochim. Cosmochim. Acta*, 57(3):555–569, 1993. doi:10.1016/0016-7037(93)90367-6

Bejannin, S., van Beek, P., Stieglitz, T., Souhaut, M., and Tamborski, J. Combining airborne thermal infrared images and radium isotopes to study submarine groundwater discharge along the French Mediterranean coastline. *J. Hydrol. Reg. Stud.*, 13(February):72–90, 2017. doi:10.1016/j.ejrh.2017.08.001

Bender, M.L. Helium-uranium dating of corals. *Geochim. Cosmochim. Acta*, 37(5):1229–1247, 1973. doi:10.1016/0016-7037(73)90058-6

Biastoch, A., Böning, C.W., Schwarzkopf, F.U., and Lutjeharms, J.R. Increase in Agulhas leakage due to poleward shift of Southern Hemisphere westerlies. *Nature*, 462(7272):495–498, 2009. doi:10.1038/nature08519

Bigeleisen, J. Nuclear size and shape effects in chemical reactions. Isotope chemistry of the heavy elements. *J. Am. Chem. Soc.*, 118(15):3676–3680, 1996. doi:10.1021/ja954076k

Border, E., Frank, N., van Beek, P., Henderson, G., Krengel, T., and Tamborski, J. Submarine Groundwater Discharge as the Cause of δ234U Enrichment in the Mediterranean Sea. *In prep.*, 2020

Bourles, B., Molinari, R.L., Johns, E., Wilson, W.D., and Leaman, K.D. Upper layer currents in the western tropical North Atlantic (1989-1991). *J. Geophys. Res. Ocean.*, 104(C1):1361–1375, 1999. doi:10.1029/1998jc900025

Brennecka, G.A., Wasylenki, L.E., Bargar, J.R., Weyer, S., and Anbar, A.D. Uranium isotope fractionation during adsorption to Mn-oxyhydroxides. *Environ. Sci. Technol.*, 45(4):1370–1375, 2011. doi:10.1021/es103061v

Broecker, W.S. A kinetic model for the chemical composition of sea water. *Quat. Res.*, 1(2):188–207, 1971. doi:10.1016/0033-5894(71)90041-X

Broecker, W.S. and Peng, T.H. *Tracers in the Sea.* Lamont-Doherty Geological Observatory, Columbia University, Palisades, New York, 10964, 1982

Burnett, W.C., Bokuniewicz, H., Huettel, M., Moore, W.S., and Taniguchi, M. Groundwater and pore water inputs to the coastal zone. 2003. doi:10.1023/B:BIOG.0000006066.21240.53

Cai, W., Santoso, A., Wang, G., Yeh, S.W., An, S.I., Cobb, K.M., Collins, M., Guilyardi, E., Jin, F.F., Kug, J.S., Lengaigne, M., Mcphaden, M.J., Takahashi, K., Timmermann, A., Vecchi, G., Watanabe, M., and Wu, L. ENSO and greenhouse warming. 2015. doi:10.1038/nclimate2743

Calhman, O.K.B. and da Hora, M.d.A.G.M. The Amazon Basin in the Context of Shared Management of Transboundary Water Resources. *J. Water Resour. Prot.*, 09(06):629–636, 2017. doi:10.4236/jwarp.2017.96042

Carlier, A., Riera, P., Amouroux, J.M., Bodiou, J.Y., Desmalades, M., and Grémare, A. Food web structure of two Mediterranean lagoons under varying degree of eutrophication. *J. Sea Res.*, 60(4):264–275, 2008. doi:10.1016/j.seares.2008.10.006

Carroll, J.L. and Moore, W.S. Uranium removal during low discharge in the Ganges-Brahmaputra mixing zone. *Geochim. Cosmochim. Acta*, 57(21-22):4987–4995, 1993. doi:10.1016/S0016-7037(05)80004-3

Cessi, P. The Global Overturning Circulation. *Ann. Rev. Mar. Sci.*, 11(1):249–270, 2019. doi:10.1146/annurev-marine-010318-095241

Chabaux, F., Riotte, J., Clauer, N., and France-Lanord, C. Isotopic tracing of the dissolved U fluxes of Himalayan rivers: Implications for present and past U budgets of the Ganges-Brahmaputra system. *Geochim. Cosmochim. Acta*, 65(19):3201–3217, 2001. doi:10.1016/S0016-7037(01)00669-X

Chabaux, F., Riotte, J., and Dequincey, O. U-Th-Ra Fractionation During Weathering and River Transport. *Rev. Mineral. Geochemistry*, 52(1):533–576, 2003. doi:10.2113/0520533

Chen, J.H., Lawrence Edwards, R., and Wasserburg, G.J. 238U, 234U and 232Th in seawater. *Earth Planet. Sci. Lett.*, 80(3-4):241–251, 1986. doi: 10.1016/0012-821X(86)90108-1

Chen, T., Robinson, L.F., Beasley, M.P., Claxton, L.M., Andersen, M.B., Lauren, J., Wadham, J., Fornari, D.J., and Harpp, K.S. Ocean mixing and ice-sheet control of seawater 234 U / 238 U during the last deglaciation. *Science (80-.).*, 1015, 2016. doi:10.1126/science.aag1015

Cheng, H., Adkins, J., Edwards, R.L., and Boyle, E.A. U-Th dating of deep-sea corals. *Geochim. Cosmochim. Acta*, 64(14):2401–2416, 2000. doi:10.1016/S0016-7037(99)00422-6

Cherdyntsev, V. Transaction of the third session of the commission for the determining the absolute age of geological formations. *Izv Akad Nauk SSSR*, 1955

Choppin, G., Liljenzin, J.O., Rydberg, J., and Ekberg, C. The Actinide and Transactinide Elements. In *Radiochem. Nucl. Chem.*, pp. 405–444. Elsevier, 2013. doi: 10.1016/b978-0-12-405897-2.00014-8

Chutcharavan, P.M., Dutton, A., and Ellwood, M.J. Seawater 234U/238U recorded by modern and fossil corals. *Geochim. Cosmochim. Acta*, 224:1–17, 2018. doi: 10.1016/j.gca.2017.12.017

Dai, A. and Trenberth, K.E. Estimates of Freshwater Discharge from Continents : Latitudinal and Seasonal Variations. *J. Hydrometeorol.*, 3:660–687, 2002

de Ruijter, W.P.M., Biastoch, A., Drijfhout, S.S., Lutjeharms, J.R.E., Matano, R.P., Pichevin, T., van Leeuwen, P.J., and Weijer, W. Indian-Atlantic interocean exchange: Dynamics, estimation and impact. *J. Geophys. Res. Ocean.*, 104(C9):20885–20910, 1999. doi:10.1029/1998jc900099

Delanghe, D., Bard, E., and Hamelin, B. New TIMS constraints on the uranium-238 and uranium-234 in seawaters from the main ocean basins and the Mediterranean Sea. *Mar. Chem.*, 80(1):79–93, 2002. doi:10.1016/S0304-4203(02)00100-7

DePaolo, D.J., Maher, K., Christensen, J.N., and McManus, J. Sediment transport time measured with U-series isotopes: Results from ODP North Atlantic drift site 984. *Earth Planet. Sci. Lett.*, 248(1-2):394–410, 2006. doi:10.1016/j.epsl.2006.06.004

Dooley, J.R., Granger, H.C., and Rosholt, J.N. Uranium-234 fractionation in the sandstone-type uranium deposits of the ambrosia lake district, New Mexico. *Econ. Geol.*, 61(8):1362–1382, 1966. doi:10.2113/gsecongeo.61.8.1362

Dornick, C. Charakterisierung verschiedener Detektortypen in der Massenspektrometrie mit induktiv gekoppelter Plasma-Quelle (ICP-MS). Ph.D. thesis, Uni Heidelberg, 2016

Douville, E., Sallé, E., Frank, N., Eisele, M., Pons-Branchu, E., and Ayrault, S. Rapid and accurate U-Th dating of ancient carbonates using inductively coupled plasma-quadrupole mass spectrometry. *Chem. Geol.*, 272(1-4):1–11, 2010. doi: 10.1016/j.chemgeo.2010.01.007

Dunk, R.M., Mills, R.A., and Jenkins, W.J. A reevaluation of the oceanic uranium budget for the Holocene. *Chem. Geol.*, 190(1-4):45–67, 2002. doi: 10.1016/S0009-2541(02)00110-9

Elliot, M. MINGULAY ROCKALL cruise, RV L'Atalante. Technical report, 2016. doi:doi.org/10.17600/16000800

England, M.H. The age of water and ventilation timescales in a global ocean model. *J. Phys. Oceanogr.*, 25(11 Part I):2756–2777, 1995. doi:10.1175/1520-0485(1995)025<2756:TAOWAV>2.0.CO;2

Esat, T.M. and Yokoyama, Y. Variability in the uranium isotopic composition of the oceans over glacial-interglacial timescales. *Geochim. Cosmochim. Acta*, 70(16):4140–4150, 2006. doi:10.1016/j.gca.2006.06.013

Fabres, J., Calafat, A., Sanchez-Vidal, A., Canals, M., and Heussner, S. Composition and spatio-temporal variability of particle fluxes in the Western Alboran Gyre, Mediterranean Sea. *J. Mar. Syst.*, 33-34:431–456, 2002. doi: 10.1016/S0924-7963(02)00070-2

Ferreira, M.L.d.C. and Kerr, R. Source water distribution and quantification of North Atlantic Deep Water and Antarctic Bottom Water in the Atlantic Ocean. *Prog. Oceanogr.*, 153:66–83, 2017. doi:10.1016/j.pocean.2017.04.003

Frank, N. M141-2 (UFO), RV Meteor. Technical report, 2017

García-Lafuente, J., Delgado, J., Criado-Aldeanueva, F., Bruno, M., del Río, J., and Miguel Vargas, J. Water mass circulation on the continental shelf of the Gulf of Cádiz. *Deep. Res. Part II Top. Stud. Oceanogr.*, 53(11-13):1182–1197, 2006. doi:10.1016/j.dsr2.2006.04.011

Geyer, W.R., Beardsley, R.C., Lentz, S.J., Candela, J., Limeburner, R., Johns, W.E., Castro, B.M., and Soares, I.D. Physical oceanography of the Amazon shelf. *Cont. Shelf Res.*, 16(5-6):575–616, 1996. doi:10.1016/0278-4343(95)00051-8

Gilli, E. Compilation d'anciennes mesures de débit à Port Miou. Apport à l'hydrogéologie de la Basse Provence Compilation d'anciennes mesures de débit à Port Miou . Apport à l'hydrogéologie de la Basse Provence. In *7e Colloq. hydrogéologie en payx calcaire milieu Fiss. Besançon.* 2001

Hansen, B., Østerhus, S., Quadfasel, D., Turrell, W., Osterhus, S., Quadfasel, D., and Turrell, W. Already the day after tomorrow? *Science (80-.).*, 305(5686):953–954, 2004. doi:DOI10.1126/science.1100085

Hebbeln, D., Wienberg, C., Bartels, M., Bergenthal, M., Frank, N., Gaide, S., Henriet, J.P., Kaszemeik, K., Klar, S., Klein, T., Krengel, T., Kuhnert, M., Meyer-Schack, B., Noorlander, C., Reuter, M., Rosiak, U., Schmidt, W., Seeba, H., Seiter, C., Stange, N., Terhzaz, L., and Van Rooij, D. MoccoMeBo Climate-driven development of Moroccan cold-water coral mounds revealed by MeBo-drilling: Atlantic vs. Mediterranean settings - Cruise MSM36 - February 18 - March 17, 2014 - Malaga (Spain) - Las Palmas (Spain). Technical report, 2015. doi:10.2312/CR_MSM36

Henderson, G.M. Seawater (234U/238U) during the last 800 thousand years. *Earth Planet. Sci. Lett.*, 199(1-2):97–110, 2002. doi:10.1016/S0012-821X(02)00556-3

Henry, L.G., McManus, J.F., Curry, W.B., Roberts, N.L., Piotrowski, A.M., and Keigwin, L.D. North Atlantic ocean circulation and abrupt climate change during the last glaciation. *Science (80-.).*, 353(6298):470–474, 2016. doi:10.1126/science.aaf5529

Hoffmann, E.D. and Stroobant, V. *Mass Spectrometry - Priniples and Applications.*, volume 29. 2007. ISBN 9780470033104. doi:10.1002/mas.20296

Horwitz, E.P., Dietz, M.L., Chiarizia, R., Diamond, H., Essling, A.M., and Graczyk, D. Separation and preconcentration of uranium from acidic media by extraction chromatography. *Anal. Chim. Acta*, 266(1):25–37, 1992. doi:10.1016/0003-2670(92)85276-C

Jaffey, A.H., Flynn, K.F., Glendenin, L.E., Bentley, W.C., and Essling, A.M. Precision measurement of half-lives and specific activities of U235 and U238. *Phys. Rev. C*, 4(5):1889–1906, 1971. doi:10.1103/PhysRevC.4.1889

Johns, W.E., Lee, T.N., Beardsley, R.C., Candela, J., Limeburner, R., and Castro, B. Annual cycle and variability of the North Brazil current. *J. Phys. Oceanogr.*, 28(1):103–128, 1998. doi:10.1175/1520-0485(1998)028<0103:ACAVOT>2.0.CO;2

Jordà, G., Von Schuckmann, K., Josey, S.A., Caniaux, G., García-Lafuente, J., Sammartino, S., Özsoy, E., Polcher, J., Notarstefano, G., Poulain, P.M., Adloff, F., Salat, J., Naranjo, C., Schroeder, K., Chiggiato, J., Sannino, G., and Macías, D. The Mediterranean Sea heat and mass budgets: Estimates, uncertainties and perspectives. 2017. doi:10.1016/j.pocean.2017.07.001

Keeling, C.D. The concentration and isotopic abundances of atmospheric carbon dioxide in rural areas. *Geochim. Cosmochim. Acta*, 13(4):322–334, 1958. doi:10.1016/0016-7037(58)90033-4

Khatiwala, S., Primeau, F., and Holzer, M. Ventilation of the deep ocean constrained with tracer observations and implications for radiocarbon estimates of ideal mean age. *Earth Planet. Sci. Lett.*, 325-326:116–125, 2012. doi:10.1016/j.epsl.2012.01.038

Kinder, T. and Parilla, G. Yes, some of the Mediterranean outflow does come from great depth. *J. Geophys. Res. Ocean.*, 92(C3):2901–2906, 1987. doi:10.1029/JC092iC03p02901

Kinder, T.H. and Bryden, H.L. Aspiration of Deep Waters through Straits. In *Phys. Oceanogr. Sea Straits*, pp. 295–319. Springer Netherlands, 1990. doi:10.1007/978-94-009-0677-8_14

Koide, M. and Goldberg, E.D. Uranium-234/uranium-238 ratios in sea water. *Prog. Oceanogr.*, 3(C):173–177, 1965. doi:10.1016/0079-6611(65)90016-9

Koschinsky, A., Frank, M., Dittmar, T., Gledhill, M., de Rezende, C., Lodeiro, P., Seidel, M., Knoke, M., Paul, S.A.L., Zitoun, R., Heinrich, L., Fronzek, J., Münch, J., Scholten, J., Border, E.C., Schneider, A., de Carvalho, L.M., Leist, L., Mutzberg, A., Marques da Silva Jr., J., Cherene Bras de Oliveira, B., Walter, J.M., Soares Nóbrega, M., Bretschneider, L., Hathorne, E.C., Vosteen, P., Spiegel, T., Maguire, C., and Rohleder, C. Interactions of trace metals, DOM, and particles in the Amazon estuary and associated plume as key processes for trace metal and DOM fluxes into the Atlantic, Cruise No. M147, April 19 - May 21, 2018, Las Palmas (Gran Canaria) - Belém (Brazil). Technical report, Bonn, 2018. doi:10.2312/cr_m147

Krengel, T. 550,000 years of marine climate variability in the western Mediterranean Sea revealed by cold-water corals. Doctoral thesis, Heidelberg University, 2020. doi:https://doi.org/10.11588/heidok.00027990

Krishnaswami, S. and Kirk Cochran, J. *U-Th Series Nuclides in Aquatic Systems*, volume 13. Elsevier Science, 2008. ISBN 9780080450124. doi:10.1016/S1569-4860(07)00001-0

Ku, T.L., Knauss, K.G., and Mathieu, G.G. Uranium in open ocean: concentration and isotopic composition. *Deep. Res.*, 24(11):1005–1017, 1977. doi:10.1016/0146-6291(77)90571-9

Kuehl, S.A., Nittrouer, C.A., Allison, M.A., Faria, L.E.C., Dukat, D.A., Jaeger, J.M., Pacioni, T.D., Figueiredo, A.G., and Underkoffler, E.C. Sediment deposition, accumulation, and seabed dynamics in an energetic fine-grained coastal environment. *Cont. Shelf Res.*, 16(5-6):787–815, 1996. doi:10.1016/0278-4343(95)00047-X

Kuehl, S.A., Nittrouer, C.A., and DeMaster, D.J. Distribution of sedimentary structures in the Amazon subaqueous delta. *Cont. Shelf Res.*, 6(1-2):311–336, 1986. doi:10.1016/0278-4343(86)90066-X

Kwon, E.Y., Kim, G., Primeau, F., Moore, W.S., Cho, H.M., DeVries, T., Sarmiento, J.L., Charette, M.A., and Cho, Y.K. Global estimate of submarine groundwater

discharge based on an observationally constrained radium isotope model. *Geophys. Res. Lett.*, 41(23):8438–8444, 2014. doi:10.1002/2014GL061574

LeBel, D.A., Smethie, W.M., Rhein, M., Kieke, D., Fine, R.A., Bullister, J.L., Min, D.H., Roether, W., Weiss, R.F., Andrié, C., Smythe-Wright, D., and Peter Jones, E. The formation rate of North Atlantic Deep Water and Eighteen Degree Water calculated from CFC-11 inventories observed during WOCE. *Deep. Res. Part I Oceanogr. Res. Pap.*, 55(8):891–910, 2008. doi:10.1016/j.dsr.2008.03.009

Lentz, S.J. The Amazon River plume during AMASSEDS: subtidal current variability and the importance of wind forcing. *J. Geophys. Res.*, 100(C2):2377–2390, 1995. doi:10.1029/94JC00343

Lübbecke, J.F., Durgadoo, J.V., and Biastoch, A. Contribution of increased agulhas leakage to tropical Atlantic warming. *J. Clim.*, 28(24):9697–9706, 2015. doi:10.1175/JCLI-D-15-0258.1

Lumpkin, R. and Speer, K. Global ocean meridional overturning. *J. Phys. Oceanogr.*, 37(10):2550–2562, 2007. doi:10.1175/JPO3130.1

Mangini, A. and Dominik, J. Late Quaternary sapropel on the Mediterranean Ridge: U-budget and evidence for low sedimentation rates. *Sediment. Geol.*, 23(1-4):113–125, 1979. doi:10.1016/0037-0738(79)90009-5

Markich, S.J. and Brown, P.L. Actinide Speciation and Bioavailability in Fresh and Marine Waters. In *Encycl. Inorg. Bioinorg. Chem.*, pp. 1–33. 2018. ISBN 9781119951438. doi:10.1002/9781119951438.eibc2559

Marshall, J. and Plumb, R.A. *Amosphere, Ocean, and Climate Dynamics: An Introductory Text*. Academic Press, 21 edition, 2007. ISBN 9780125586917

Marshall, J. and Speer, K. Closure of the meridional overturning circulation through Southern Ocean upwelling. 2012. doi:10.1038/ngeo1391

Martin, J.M., Meybeck, M., and Pusset, M. Uranium behaviour in the Zaire estuary. 1978. doi:10.1016/0077-7579(78)90036-4

Mascarenhas, A.C., Gomes, G.S., Lima, A.P., da Silva, H.K., Santana, L.S., Rosário, R.P., and Rollnic, M. Seasonal Variations of the Amazon River Plume with Focus on the Eastern Sector. *J. Coast. Res.*, 75(sp1):532–536, 2016. doi:10.2112/si75-107.1

Matsumoto, K. Radiocarbon-based circulation age of the world oceans. *J. Geophys. Res. Ocean.*, 112(9), 2007. doi:10.1029/2007JC004095

McCarthy, G.D., Smeed, D.A., Johns, W.E., Frajka-Williams, E., Moat, B.I., Rayner, D., Baringer, M.O., Meinen, C.S., Collins, J., and Bryden, H.L. Measuring the Atlantic Meridional Overturning Circulation at 26N. *Prog. Oceanogr.*, 130:91–111, 2015. doi:10.1016/j.pocean.2014.10.006

McClain, M.E. and Naiman, R.J. Andean Influences on the Biogeochemistry and Ecology of the Amazon River. *Bioscience*, 58(4):325–338, 2008. doi:10.1641/b580408

McKee, B.A., DeMaster, D.J., and Nittrouer, C.A. Uranium geochemistry on the Amazon shelf: Evidence for uranium release from bottom sediments. *Geochim. Cosmochim. Acta*, 51(10):2779–2786, 1987. doi:10.1016/0016-7037(87)90157-8

McPhaden, M.J., Zebiak, S.E., and Glantz, M.H. ENSO as an integrating concept in earth science. 2006. doi:10.1126/science.1132588

Meade, R.H., Dunne, T., Richey, J.E., Santos, U.D.M., and Salati, E. Storage and remobilization of suspended sediment in the lower amazon river of Brazil. *Science (80-.).*, 228(4698):488–490, 1985. doi:10.1126/science.228.4698.488

Meija, J., Coplen, T.B., Berglund, M., Brand, W.A., De Bièvre, P., Gröning, M., Holden, N.E., Irrgeher, J., Loss, R.D., Walczyk, T., and Prohaska, T. Atomic weights of the elements 2013 (IUPAC Technical Report). 2016. doi:10.1515/pac-2015-0305

Meinen, C.S., Speich, S., Piola, A.R., Ansorge, I., Campos, E., Kersalé, M., Terre, T., Chidichimo, M.P., Lamont, T., Sato, O.T., Perez, R.C., Valla, D., van den Berg, M., Le Hénaff, M., Dong, S., and Garzoli, S.L. Meridional Overturning Circulation Transport Variability at 34.5S During 2009–2017: Baroclinic and Barotropic Flows and the Dueling Influence of the Boundaries. *Geophys. Res. Lett.*, 45(9):4180–4188, 2018. doi:10.1029/2018GL077408

Milliman, J. River Inputs. In *Encycl. Ocean Sci.*, pp. 2419–2427. Elsevier, 2001. doi:10.1006/rwos.2001.0074

Millot, C. and Taupier-Letage, I. Circulation in the Mediterranean Sea. 5(June):29–66, 2006. doi:10.1007/b107143

Moore, W.S. Amazon and Mississippi river concentrations of uranium, thorium, and radium isotopes. *Earth Planet. Sci. Lett.*, 2(3):231–234, 1967. doi:10.1016/0012-821X(67)90134-3

Moore, W.S. The effect of submarine groundwater discharge on the ocean. *Ann. Rev. Mar. Sci.*, 2:59–88, 2010. doi:10.1146/annurev-marine-120308-081019

Moore, W.S., Sarmiento, J.L., and Key, R.M. Submarine groundwater discharge revealed by 228Ra distribution in the upper Atlantic Ocean. *Nat. Geosci.*, 1(5):309–311, 2008. doi:10.1038/ngeo183

Moore, W.S. and Shaw, T.J. Fluxes and behavior of radium isotopes, barium, and uranium in seven Southeastern US rivers and estuaries. *Mar. Chem.*, 108(3-4):236–254, 2008. doi:10.1016/j.marchem.2007.03.004

Nittrouer, C.A. and DeMaster, D.J. The Amazon shelf setting: Tropical, energetic, and influenced by a large river. *Cont. Shelf Res.*, 16(5-6):553–573, 1996. doi: 10.1016/0278-4343(95)00069-0

Nomura, M., Higuchi, N., and Fujii, Y. Mass dependence of uranium isotope effects in the U(IV)-U(VI) exchange reaction. *J. Am. Chem. Soc.*, 118(38):9127–9130, 1996. doi:10.1021/ja954075s

Ollivier, P., Radakovitch, O., and Hamelin, B. Major and trace element partition and fluxes in the Rhône River. *Chem. Geol.*, 285(1-4):15–31, 2011. doi:10.1016/J.CHEMGEO.2011.02.011

Osmond, J.K. and Cowart, J.B. U-Series Nuclides as Tracers in Groundwater Hydrology. In *Environ. Tracers Subsurf. Hydrol.*, pp. 145–173. Springer US, 2000. doi:10.1007/978-1-4615-4557-6_5

Osmond, J.K. and Ivanovich, M. Uranium series mobilization and surface hydrology. *Uranium-Series Disequilibrium Appl. to Earth Mar. Environ. Sci.*, 1992

Palmer, M.R. and Edmond, J.M. Uranium in river water. *Geochim. Cosmochim. Acta*, 57(20):4947–4955, 1993. doi:10.1016/0016-7037(93)90131-F

Palter, J.B. The Role of the Gulf Stream in European Climate. *Ann. Rev. Mar. Sci.*, 7(1):113–137, 2015. doi:10.1146/annurev-marine-010814-015656

Pataki, D.E., Ehleringer, J.R., Flanagan, L.B., Yakir, D., Bowling, D.R., Still, C.J., Buchmann, N., Kaplan, J.O., and Berry, J.A. The application and interpretation of Keeling plots in terrestrial carbon cycle research. *Global Biogeochem. Cycles*, 17(1), 2003. doi:10.1029/2001GB001850

Porcelli, D. and Swarzenski, P.W. The behavior of U- and Th-series nuclides in groundwater. In *Uranium-series Geochemistry*, volume 52, pp. 317–361. De Gruyter Mouton, 2003. ISBN 9781501509308. doi:10.2113/0520317

Pritchard, D.W. What is an Estuary: Physical Viewpoint. 1967

Rahmstorf, S. Thermohaline Ocean Circulation. In *Encycl. Quat. Sci.*, pp. 1–10. 2006. ISBN 9780122274305. doi:10.1016/B0-44-452747-8/00014-4

Richardson, P.L. Agulhas leakage into the Atlantic estimated with subsurface floats and surface drifters. *Deep. Res. Part I Oceanogr. Res. Pap.*, 54(8):1361–1389, 2007. doi:10.1016/j.dsr.2007.04.010

Robinson, A., Leslie, W., Theocharis, A., and Lascaratos, A. Mediterranean Sea Circulation. In *Encycl. Ocean Sci.*, pp. 1689–1705. 2001a. doi:10.1006/rwos.2001.0376

Robinson, A.R., Leslie, W.G., Theocharis, A., and Lascaratos, A. Mediterranean Sea Circulation. In *Encycl. Ocean Sci. Second Ed.*, pp. 710–725. Elsevier Ltd., 2001b. ISBN 9780123744739. doi:10.1016/B978-012374473-9.00376-3

Robinson, L.F., Belshaw, N.S., and Henderson, G.M. U and Th concentrations and isotope ratios in modern carbonates and waters from the Bahamas. *Geochim. Cosmochim. Acta*, 68(8):1777–1789, 2004a. doi:10.1016/j.gca.2003.10.005

Robinson, L.F., Henderson, G.M., Hall, L., and Matthews, I. Climatic control of riverine and seawater uranium-isotope ratios. *Science (80-.).*, 305(5685):851–854, 2004b. doi:10.1126/science.1099673

Rodellas, V., Garcia-Orellana, J., Masqué, P., Feldman, M., and Weinstein, Y. Submarine groundwater discharge as a major source of nutrients to the Mediterranean Sea. *Proc. Natl. Acad. Sci.*, 112(13):3926–3930, 2015. doi:10.1073/pnas.1419049112

Rosholt, J.N., Harshman, E.N., Shields, W.R., and Garner, E.L. Isotopic fractionation of uranium related to roll features in sandstone, Shirley Basin, Wyoming. *Econ. Geol.*, 59(4):570–585, 1964. doi:10.2113/gsecongeo.59.4.570

Ruddiman, W. *Earth's Climate: Past and Future*. Macmillan, 2001. ISBN 9781429255257

Rühs, S., Durgadoo, J.V., Behrens, E., and Biastoch, A. Advective timescales and pathways of Agulhas leakage. *Geophys. Res. Lett.*, 40(15):3997–4000, 2013. doi:10.1002/grl.50782

Sarin, M.M. and Church, T.M. Behaviour of uranium during mixing in the delaware and chesapeake estuaries. *Estuar. Coast. Shelf Sci.*, 39(6):619–631, 1994. doi:10.1016/S0272-7714(06)80013-2

Sarin, M.M., Krishnaswami, S., Somayajulu, B.L., and Moore, W.S. Chemistry of uranium, thorium, and radium isotopes in the Ganga-Brahmaputra river system: Weathering processes and fluxes to the Bay of Bengal. *Geochim. Cosmochim. Acta*, 54(5):1387–1396, 1990. doi:10.1016/0016-7037(90)90163-F

Schlitzer, R. Ocean Data View. 2018

Scott, M. The chemistry of U- and Th-series nuclide in the rivers. In *Uranium Ser. Disequilibrium Appl. to Environ. Probl.*, pp. 181–201. 1982. ISBN 0-19-854423-5

Shaltout, M. and Omstedt, A. Modelling the water and heat balances of the Mediterranean Sea using a two-basin model and available meteorological, hydrological, and Ocean data. *Oceanologia*, 57(2):116–131, 2015. doi:10.1016/j.oceano.2014.11.001

Shiel, A.E., Laubach, P.G., Johnson, T.M., Lundstrom, C.C., Long, P.E., and Williams, K.H. No measurable changes in 238U/235U due to desorption-adsorption of U(VI) from groundwater at the Rifle, Colorado, integrated field research challenge site. *Environ. Sci. Technol.*, 47(6):2535–2541, 2013. doi: 10.1021/es303913y

Sholkovitz, E.R. The geochemistry of rare earth elements in the Amazon River estuary. *Geochim. Cosmochim. Acta*, 57(10):2181–2190, 1993. doi:10.1016/0016-7037(93)90559-F

Smoak, J.M., Krest, J.M., and Swarzenski, P.W. Geochemistry of the Amazon estuary. *Handb. Environ. Chem. Vol. 5 Water Pollut.*, 5(PART H):71–90, 2006. doi:10.1007/698-5-029

Sparnocchia, S., Manzella, G.M.R., and Violette, P.E.L. The Interannual and Seasonal Variability of the MAW and LIW Core Properties in the Western Mediterranean Sea. In *Seas. Interannual Var. West. Mediterr. Sea, Vol. 46*, pp. 177–194. American Geophysical Union (AGU), 1994. doi:10.1029/CE046P0117

Stieglitz, T.C., van Beek, P., Souhaut, M., and Cook, P.G. Karstic groundwater discharge and seawater recirculation through sediments in shallow coastal Mediterranean lagoons, determined from water, salt and radon budgets. *Mar. Chem.*, 156:73–84, 2013. doi:10.1016/j.marchem.2013.05.005

Suksi, J., Rasilainen, K., and Pitkänen, P. Variations in 234U/238U activity ratios in groundwater-A key to flow system characterisation? *Phys. Chem. Earth*, 31(10-14):556–571, 2006. doi:10.1016/j.pce.2006.04.007

Swart, P.K. and Hubbard, J.A. Uranium in scleractinian coral skeletons. *Coral Reefs*, 1(1):13–19, 1982. doi:10.1007/BF00286535

Swarzenski, P., Campbell, P., Porcelli, D., and McKee, B. The estuarine chemistry and isotope systematics of234,238U in the Amazon and Fly Rivers. *Cont. Shelf Res.*, 24(19):2357–2372, 2004. doi:10.1016/j.csr.2004.07.025

Swarzenski, P.W. and McKee, B.A. Seasonal uranium distributions in the coastal waters off the Amazon and Mississippi Rivers. *Estuaries*, 21(3):379–390, 1998. doi:10.2307/1352837

Swarzenski, P.W., McKee, B.A., and Booth, J.G. Uranium geochemistry on the Amazon shelf: Chemical phase partitioning and cycling across a salinity gradient. *Geochim. Cosmochim. Acta*, 59(1):7–18, 1995a. doi:10.1016/0016-7037(94)00371-R

Swarzenski, P.W., McKee, B.A., and Booth, J.G. Uranium geochemistry on the Amazon shelf: Chemical phase partitioning and cycling across a salinity gradient. *Geochim. Cosmochim. Acta*, 59(1):7–18, 1995b. doi:10.1016/0016-7037(94)00371-R

Talley, L.D. Closure of the global overturning circulation through the Indian, Pacific, and southern oceans. *Oceanography*, 26(1):80–97, 2013. doi:10.5670/oceanog.2013.07

Tanhua, T., Hainbucher, D., Schroeder, K., Cardin, V., Álvarez, M., and Civitarese, G. The Mediterranean Sea system: A review and an introduction to the special issue. 2013. doi:10.5194/os-9-789-2013

ThermoFisher. *Finnigan Neptune*. Thermo Fisher Scientific, Massachusetts, 2009

Thomas, R. Practical Guide to ICP-MS: A Tutorial for Beginners, Third Edition. *Robert Thomas*, p. 446, 2013. doi:10.1017/CBO9781107415324.004

Thurber, D.L. Anomalous U 234 U 238 in nature. *J. Geophys. Res.*, 67(11):4518–4520, 1962. doi:10.1029/jz067i011p04518

Tsimplis, M.N., Zervakis, V., Josey, S.A., Peneva, E.L., Struglia, M.V., Stanev, E.V., Theocharis, A., Lionello, P., Malanotte-Rizzoli, P., Artale, V., Tragou, E., and Oguz, T. Changes in the oceanography of the Mediterranean Sea and their link to climate variability. In *Dev. Earth Environ. Sci.*, volume 4, pp. 227–282. Elsevier, 2006. doi:10.1016/S1571-9197(06)80007-8

Weijer, W., De Ruijter, W.P., and Dukstra, H.A. Stability of the atlantic overturning circulation: Competition between bering strait freshwater flux and agulhas heat and salt sources. *J. Phys. Oceanogr.*, 31(8 PART 2):2385–2402, 2001. doi:10.1175/1520-0485(2001)031<2385:sotaoc>2.0.co;2

Wendt, K.A., Pythoud, M., Moseley, G.E., Dublyansky, Y.V., Edwards, R.L., and Spötl, C. Paleohydrology of southwest Nevada (USA) based on groundwater 234U/238U over the past 475 k.y. *GSA Bull.*, (July), 2019. doi:10.1130/b35168.1

Zänker, H. and Hennig, C. Colloid-borne forms of tetravalent actinides: A brief review. 2014. doi:10.1016/j.jconhyd.2013.11.004

Zebracki, M., Cagnat, X., Gairoard, S., Cariou, N., Eyrolle-Boyer, F., Boulet, B., and Antonelli, C. U isotopes distribution in the Lower Rhone River and its implication on radionuclides disequilibrium within the decay series. *J. Environ. Radioact.*, 178-179:279–289, 2017. doi:10.1016/j.jenvrad.2017.09.004

Zodiatis, G. Advection of Black Sea water in the north Aegean Sea. *Glob. Atmos. Ocean Syst.*, 2(1):41–60, 1994

Acknowledgments

Sir Issac Newton best described scientific achievement when he stated

"If I have seen further it is by standing on the shoulders of Giants"

Truly, any work is dependent upon the combined effort of many others, both in providing a basis from which to build as well as supporting in parallel. For this reason I would first like to extend a warm thank you to the entire Physics of Environmental Archives group, both present and past members, whose hard-work has allowed for my own humble contribution.

There are many who have gone out of their way to help me over the years and I apologize sincerely to whomever I have forgotten to list (though perhaps that is indicative of you being helpful to such a degree that I didn't even realize it). I'd like to thank my parents for supporting me when I came up with the crazy idea to move half the world away to study environmental physics, rather than trying to convince me to do something more *practical*. I'd like to thank my partner and best-friend Matea for putting up with my 'weird science lifestyle' as well as my occasional stress-induced craziness (particularly over the past year or so). I'd like to thank my good friends and fellow PhDs, Steffen, Marleen, Thomas, and Julius for their support over the years, particularly as a foreigner trying to learn the language (ganz ehrlich, wie habt ihr mich überhaupt verstanden?). I'd like to thank my fifth-floor team, particularly Markus and Inga. I'd like to thank René for trying his best to speak hoch-deutsch while explaining mass-spectrometry to someone struggling to understand. I'd like to thank Andrea for always pointing me in the right direction when I can't understand the bureaucracy. I'd like to thank my proof-reader Sophie for giving great in-depth feedback.

Lastly, I would like to thank the person who ultimately made all this possible: Norbert. Without you believing in me and giving me the opportunity I never could have done anything like this. I'll never forget hearing your Environmental Physics lecture and just thinking 'wow...this is something I really want to do!'. More than anything, I appreciate the freedom and trust you have shown me over the years, particularly through letting me try out new things (even when there wasn't always a clearly defined goal). I sincerely hope that I've repaid your belief in me. You've provided an environment in which I've been able to flourish and prepare myself for the next step in life. For that I am extremely grateful.

Vielen Dank an euch alle!
-Evan